

AD-A174 784

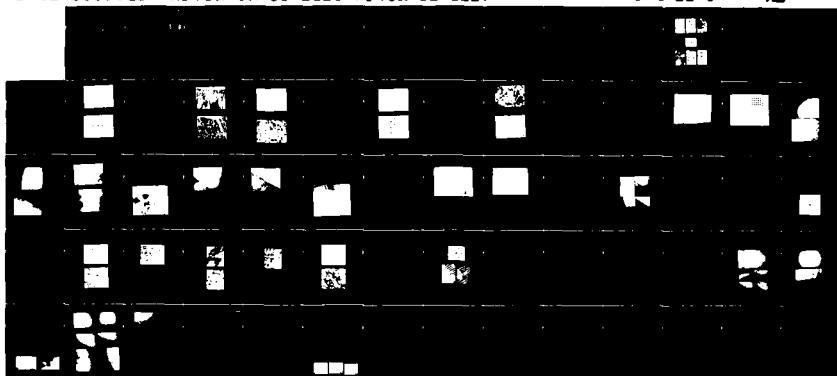
A FUNDAMENTAL STUDY OF THE BONDING OF THERMAL BARRIER  
COATINGS(U) CASE WESTERN RESERVE UNIV CLEVELAND OH DEPT  
OF METALLURGY AND... J E MITCHELL ET AL. JUN 86  
AFOSR-IR-86-2013 AFOSR-82-0227

1/1

UNCLASSIFIED

F/C 11/3

ML



END

DATE  
FILMED  
F



② ~~SECRET~~  
AFOSR-TR. 86-2013

FINAL SCIENTIFIC REPORT ON  
A FUNDAMENTAL STUDY OF THE BONDING OF THERMAL BARRIER COATINGS

AD-A174 784

Submitted to:

Air Force Office of Scientific Research

Contract No. 82-0227

For The Period June 15, 1982 to November 30, 1985

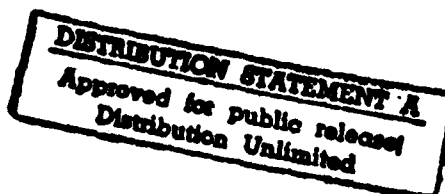
DTIC  
SELECTE  
NOV 26 1986  
S D

By:

T.E. Mitchell and A.H. Heuer

Department of Metallurgy & Materials Science  
CASE WESTERN RESERVE UNIVERSITY  
10900 Euclid Avenue  
Cleveland, OH 44106

JUNE 1986



86 11 25 368

6c. ADDRESS (City, State and ZIP Code) 10900 Euclid Avenue Cleveland, OH 44106		7d. ADDRESS (City, State and ZIP Code) Building 410 Bolling AFB DC 20332-6448	
8a. NAME OF FUNDING/SPONSORING ORGANIZATION AFOSR	8b. OFFICE SYMBOL (if applicable) NE	9. PROCUREMENT INSTRUMENT IDENTIFICATION NUMBER AFOSR-82-0227	
8c. ADDRESS (City, State and ZIP Code) Bld 410 BAFB DC 20332-6448		10. SOURCE OF FUNDING NOS.	
		PROGRAM ELEMENT NO. 2500/AZ -61102F	PROJECT NO. 2306
		TASK NO. A2	WORK UNIT NO.
11. TITLE (Include Security Classification) Fundamental Study of the Bonding of Thermal Barrier Coatings			
12. PERSONAL AUTHOR(S) T. E. Mitchell and A.H. Heuer			
13a. TYPE OF REPORT Final (includes Annual)	13b. TIME COVERED FROM 6/15/82 TO 11/30/85	14. DATE OF REPORT (Yr., Mo., Day) June 86	15. PAGE COUNT 5
16. SUPPLEMENTARY NOTATION			

## 1. INTRODUCTION

This report describes the progress and publications which have resulted from AFOSR support of our research on fundamental studies of the bonding of zirconia-yttria thermal barrier coatings to alumina-forming alloy bond coats on superalloys. This research has been directed by Professors T.E. Mitchell and A.H. Heuer with the active research being performed by Ms. S. Kraus (for her M.S. Thesis) and Dr. V. Lanteri (for his Ph.D. Thesis).

Two layer thermal barrier coatings are currently being developed for extending the performance of nickel base superalloy gas turbine engines. The best materials reported to date comprise a Ni-Cr-Al-Y bond coat and a  $Y_2O_3$  partially stabilized  $ZrO_2$  (Y-PSZ) thermal barrier coat. The Y level of both the bond coat and the thermal barrier coat have been studied empirically but the fundamental factors that govern optimization of the thermal barrier system are not well understood. Optimized systems perform remarkably well during high temperature exposure and thermal cycling but failure still tends to occur by radial cracking in the ceramic coat and circumferential cracking at the various metal/ceramic interfaces. ~~In the present study we have concentrated on~~ <sup>As discussed</sup> two fundamental aspects of the behavior: firstly, phase stability in the zirconia-yttria system itself, particularly the desirable tetragonal phase, and secondly, the nature of the important zirconia-alumina interface which forms during oxidation of the underlying bond coat. The results of this research are described briefly below and in the various Appendices. Section 6 lists our various publications deriving from AFOSR sponsorship.



Accession For	
NTIS CRA&I	<input checked="checked" type="checkbox"/>
DTIC TAB	<input type="checkbox"/>
Unannounced	<input type="checkbox"/>
Justification	
By	
Distribution /	
Availability Codes	
Dist	
A-1	

## 2. PHASE STABILITY IN YTTRIA PARTIALLY STABILIZED ZIRCONIA

The microstructure of the tetragonal phase in yttria partially stabilized zirconia (Y-PSZ) is very sensitive to cooling rates. With fast cooling rates a displacive, but non-martensitic, transformation occurs resulting in the formation of a tetragonal solid solution ( $t'$ -ZrO<sub>2</sub>) with the same yttria content as the parent cubic phase ( $c$ -ZrO<sub>2</sub>). The microstructure is characterized by the presence of antiphase domain boundaries (APB's) resulting from the loss of symmetry during the transformation, and by 90° twins formed mechanically to relieve the transformation strains.

With slow cooling rates, the equilibrium tetragonal solid solution ( $t$ -ZrO<sub>2</sub>) starts to precipitate; at room temperature the material has a tweed-like microstructure. After lengthy annealings at high temperatures in the two phase field ( $t + c$ ),  $t$ -ZrO<sub>2</sub> coarsens in a cubic matrix which can again undergo a displacive transformation upon cooling depending on its rate.  $t$ -ZrO<sub>2</sub> has a particular microstructure consisting of large colonies of twin related variants. Each colony is formed by stacking plates of two tetragonal variants sharing the same (101) habit plane, with their  $c$ -axes at about 90°. This microstructure effectively reduces the overall strain energy.

The tetragonal colonies can martensitically transform to monoclinic symmetry ( $m$ -ZrO<sub>2</sub>) under the action of a propagating crack. There is no evidence of a  $t'$ -ZrO<sub>2</sub> to  $m$ -ZrO<sub>2</sub> transformation.

The colonies can also transform to an orthorhombic phase ( $o$ -ZrO<sub>2</sub>) by a pure thin film effect. This transformation is also displacive and is characterized by the presence of APB's.

The difference in morphology and distribution of tetragonal

precipitates in the three major classes of PSZ (Mg-, Ca-, and Y-PSZ) is explained in terms of strain energy reduction using Khachaturyan's theory of structural transformations in solids.

### 3. STRUCTURE OF $\text{ZrO}_2/\text{Al}_2\text{O}_3$ INTERFACES

High resolution electron microscopy has been used to study the interfacial structures in  $\text{ZrO}_2$ -toughened  $\text{Al}_2\text{O}_3$ . The  $\text{ZrO}_2$  exists as both inter- and intragranular particles, and the most informative images are of intragranular  $\text{ZrO}_2/\text{Al}_2\text{O}_3$  interfaces. The majority of these particles are spherical, but some are faceted, implying that there are low energy interfaces between the two materials. For spherical particles, both ledge-like structure and misfit dislocation-like structures accommodate the lattice misfit, depending on the orientation of the interface. The intergranular particle/matrix interfaces yielded little information, as there is a ubiquitous glassy phase which can, at times, obscure the interface boundary. Computer simulation is being used to interpret the structures: successful matches between experimental and computed images of the perfect  $\text{Al}_2\text{O}_3$  matrix have been made and the technique is being extended to the interface. The results show that the interface is sharp, that there is no evidence for any interaction zone between the two oxides, but that the interfacial adhesion is still apparently strong.

### 4. RELEVANCE TO THERMAL BARRIER COATING BEHAVIOR

So far as phase stability is concerned, our results show quite clearly that compositions in the range of 6-8 wt.% yttria ought to consist of 100% tetragonal phase ( $t'$ ). This phase is metastable but has been called non-transformable because the monoclinic phase does not form during cooling

to room temperature. It ought to remain stable during exposure to temperatures as high as 1200°C even during thermal cycling. In fact, our own observations and those of others show that the amount of monoclinic and cubic phases gradually increase during high temperature exposure and the monoclinic phase is a potential source of failure. The most likely reason for this is the non-uniformity of the powder compositions used for plasma spraying since powder containing less than about 4 wt.% yttria will transform to the monoclinic phase on cooling. Transmission electron microscope studies have shown that the microstructures observed in the plasma sprayed material are much the same as in the bulk material except for the variability in the microstructure which is produced by the inhomogeneous composition and the variation in cooling rate. Near to the bond coat the splats have a high cooling rate and so the resulting structure consists of very fine columnar grains of  $t'$ . Near the outer surface the cooling rate is much slower and so the grains are larger and contain the  $t'$  colonies and APB's already described in the bulk material. The structure is still stable to high temperature exposure and it is the compositional inhomogeneity which gives rise to problems with stability. If a powder with a uniform composition of 6-8 wt.% yttria were used, the resulting 100% tetragonal ceramic coat should be stable to high temperature exposure. These results were presented at the workshop on Thermal Barrier Coatings organized by NASA Lewis Research Center, May 20-21, 1985 and at a similar symposium organized by the American Vacuum Society in San Diego, April 7-11, 1986.

So far as the zirconia-alumina interface is concerned, we have shown that the interface is incoherent but that the incoherency is accommodated with step-like and dislocation-like structures at the atomic level. Such



an interface will form during high temperature exposure of the thermal barrier coating system, since the bond coat becomes oxidized by diffusion of oxygen through the ceramic coat. Electron microscopy observations on these interfaces show that they are quite adherent in much the same way as the interfaces observed by high resolution electron microscopy. In fact, we have found that the ceramic coat spalls off at the alumina-metal interface just as much as at the alumina zirconia interface. The main problem here seems to be to maintain a sufficient level of yttrium in the Ni-Cr-Al bond-coat so as to maintain adhesion at the alloy/alumina interface.

#### 5. Prior AFOSR - Supported Research

As a matter of completeness, we include in Section 6 several publications completed during the current contract period which actually derives from previous AFOSR support to T.E. Mitchell and A.H. Heuer (Contract No. F49620-78C-0053). Both relate to oxidation issues relevant to advanced high temperature ceramics; one provides evidence that diffusion of oxygen through the passive silica film that forms on SiC cannot control the oxidation kinetics; the second reviews the use of "volatility" or "stability" diagrams, which are the most convenient way of representing available thermodynamic data relevant to oxidation of metals, alloys, and non-oxide ceramics and also evaporation of oxide ceramics.

## 16. PUBLICATIONS

1. V. Lanteri, A.H. Heuer and T.E. Mitchell, "Tetragonal Precipitation in the System  $Y_2O_3$ - $ZrO_2$ ", in Proc. 41st Annual Meeting, Electron Microscopy Society of America, G.W. Bailey, ed., San Francisco Press, p. 58 (1983). - Appendix 1
2. S. Farmer, V. Lanteri, J. Hangan, T.E. Mitchell, and A.H. Heuer, "Ordered Defect Fluorite Compounds in  $ZrO_2$  Alloys", in Electron Microscopy in Materials Science, W. Krakow, D.A. Smith and L.W. Hobbs, eds., North Holland, p. 357 (1984). - Appendix 2
3. V. Lanteri, A.H. Heuer and T.E. Mitchell, "Tetragonal Phase in the System  $Y_2O_3$ - $ZrO_2$ ", in Advances in Ceramics, Vol. 12, Science and Technology of Zirconia II, The American Ceramic Society, Columbus, Ohio, p. 118-130, 1984. - Appendix 3
4. A.H. Heuer, S.P. Kraus-Lanteri, P.A. Labun, V. Lanteri, and T.E. Mitchell, "HREM Studies of Coherent and Incoherent Interfaces in  $ZrO_2$ -Containing Ceramics: A Preliminary Account", Ultramicroscopy **18**, 335-348 (1985). - Appendix 4
5. S. Kraus, "HREM Studies of Interfaces in  $ZrO_2/Al_2O_3$  Ceramics", Proc. 43rd Annual Meeting, Electron Microscopy Society of America, G.W. Bailey, ed., San Francisco Press, p. 218-219 (1985). - Appendix 5
6. A.H. Heuer, S.P. Kraus-Lanteri, P.A. Labun, and T.E. Mitchell, "HREM of Incoherent  $ZrO_2/Al_2O_3$  Interfaces", Inst. Phys. Conf. Ser. No. 78, EMAG '85, Adam Hilger, p. 519-522 (1985). - Appendix 6
7. S.P. Kraus-Lanteri, T.E. Mitchell and A.H. Heuer, "Structure of Incoherent  $ZrO_2/Al_2O_3$  Interfaces", J. Amer. Ceram. Soc. **69**, p. 256-258 (1986). - Appendix 7
8. V. Lanteri, T.E. Mitchell and A.H. Heuer, "The Morphology of Tetragonal Precipitates in Partially-Stabilized Zirconia", J. Amer. Ceram. Soc., in press (1986). - Appendix 8 (Abstract only)
9. A.H. Heuer, R. Chaim and V. Lanteri, "The Displacive Cubic-Tetragonal Transformation in  $ZrO_2$  Alloys", submitted to Acta Met. (1986). - Appendix 9 (Abstract only)
10. D.M. Mieskowski, T.E. Mitchell and A.H. Heuer, "Bubble Formation in Oxide Scales on SiC", J. Am. Ceram. Soc., Vol. 67, No. 1, (1984). - Appendix 10
11. V.L.K. Lou, T.E. Mitchell and A.H. Heuer, "Review - Graphical Displays of the Thermodynamics of High-Temperature Gas-Solid Reactions and Their Application to Oxidation of Metals and Evaporation of Oxides", J. Am. Ceram. Soc., Vol. 68, No. 2, (1985). - Appendix 11

## TETRAGONAL PRECIPITATION IN THE SYSTEM $Y_2O_3$ - $ZrO_2$

V. Lanteri, A. H. Heuer and T. E. Mitchell

Department of Metallurgy and Materials Science  
Case Western Reserve University, Cleveland, Ohio 44106

**INTRODUCTION:** The major applications of partially stabilized zirconia (PSZ) concern materials in which the microstructures are in the two phase regions (cubic-tetragonal or cubic-monoclinic). The aim of this paper is to discuss the occurrence of tetragonal precipitation in yttria-PSZ. Despite the similarity with other doped zirconia alloys (Mg-PSZ, Ca-PSZ), the shape, the habit planes and mechanisms of precipitation are found to be different for Y-PSZ. Single crystals, obtained from skull melting, with composition 8wt%- $Y_2O_3$  were examined by transmission electron microscopy (TEM) and the tetragonal phase was imaged using standard dark field techniques.

**AS RECEIVED MATERIALS.** Because of the crystallography of the tetragonal phase ( $t$ - $ZrO_2$ ), which is obtained by slight displacements of the oxygen atoms from the fluorite type cubic phase ( $c$ - $ZrO_2$ ), there are three variants (the  $c$ -axis being along one of the  $\langle 100 \rangle$  directions). Fig. 1 shows a  $\{111\}$  diffraction pattern, where the two reciprocal lattices ( $c$ - $ZrO_2$  and  $t$ - $ZrO_2$ ) are indexed. The weakest spots, which are forbidden for the fluorite structure, are due only to the  $t$ - $ZrO_2$  resulting from the slightly distorted fluorite cell. In this particular orientation,  $\{112\}$  spots were used to image the three variants of the  $t$ - $ZrO_2$  phase, as shown in the dark field micrographs of Fig. 2. Fig. 2a and 2b clearly show the three variants of precipitates which have  $\{110\}$  habit planes and possess all the features of a diffusion-assisted transformation. Fig. 2c, which is obtained using the third  $\{112\}$  tetragonal reflection, surprisingly shows a different microstructure. This  $t$ - $ZrO_2$  phase must be the non-transformable  $t'$ - $ZrO_2$  reported by Scott (1) in his non-equilibrium phase diagram, and by Miller, et al. (2) in plasma sprayed materials. It is believed that this material is a mixture of  $t$ - $ZrO_2$  and  $t'$ - $ZrO_2$  with very little cubic phase (as confirmed by x-ray diffraction).

**AGED SPECIMENS.** Fig. 3 consists of dark field micrographs of the same material, aged at 24 hours at 1600°C, imaged as in the case above by using the three tetragonal reflections in the  $\{111\}$  orientation. It is seen that the  $t'$ - $ZrO_2$  occurs in large colonies of plates lying in  $\{110\}$  planes. Each colony is indeed formed by two variants (different  $c$ -axes) with the same habit planes. This is shown in Figs. 3a and 3b in which one variant is imaged using one particular reflection, whereas the other variant within the same colony is imaged with another reflection.

**CONCLUSIONS.** Evidence of two tetragonal phases has been found:  $t$ - $ZrO_2$  is the usual tetragonal phase formed by a diffusion process, also encountered in polycrystalline sintered materials (3); and  $t'$ - $ZrO_2$ , which is believed to form via a diffusionless process, is unstable at high temperatures, and decomposes into  $t$ - $ZrO_2$  and  $c$ - $ZrO_2$  during annealing.(4)

### References

1. H.G.Scott, J. Mat. Sci., **10** (1975), 1527-1535.
2. R.B.Miller, J.L.Smialek and R.G.Garlick, *Advances in Ceramics*, Vol. 3, *Science and Technology of Zirconia*, ed. A.H.Heuer and L.W.Hobbs, The American Ceramic Society, (1981) p. 241.
3. P.C.Valentine, M.S. Thesis, Case Western Reserve University (1982).
4. The authors thank the Naval Research Lab, Washington, D.C. for providing the single crystals. This research has been supported by AFOSR-82-0227.

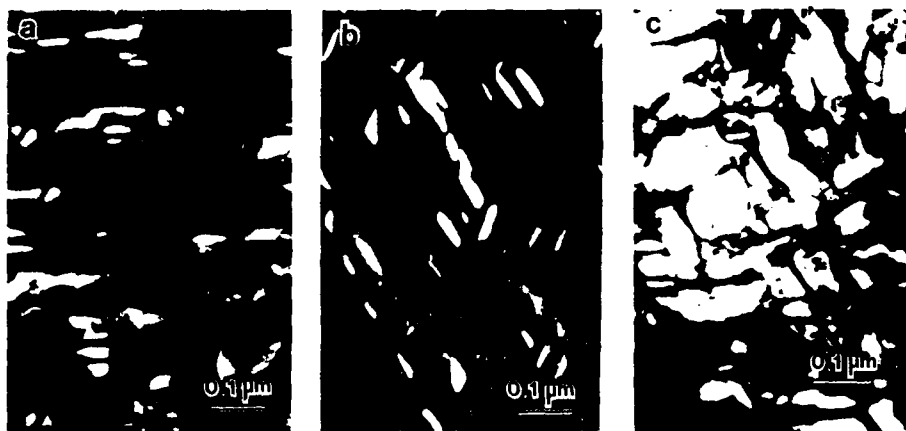


Fig. 2. Dark field micrographs of as received specimen  
 a)  $g = 112_t$       b)  $g = 121_t$       c)  $g = 211_t$

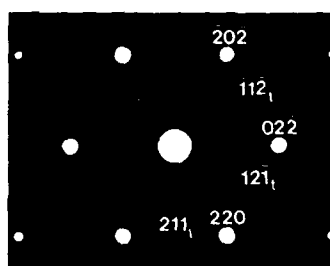


Fig. 1  $[111]$  Diffraction pattern

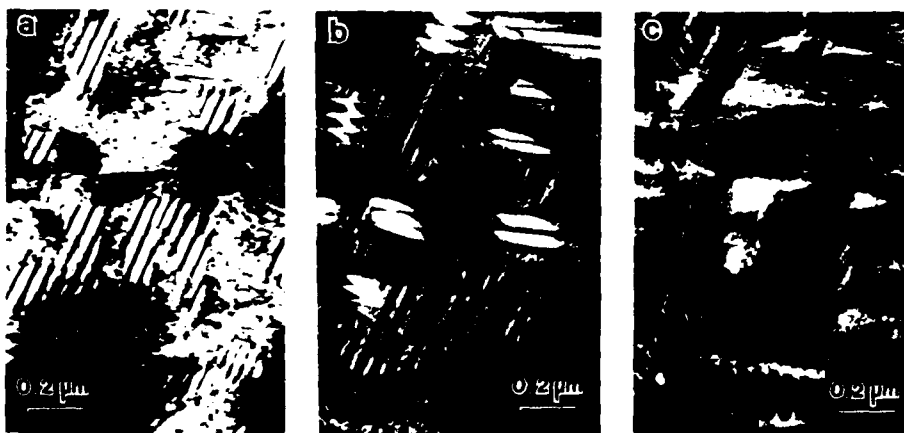


Fig. 3. Dark field micrographs of aged specimen at 1600°C for 24 hr.  
 a)  $g = 112_t$       b)  $g = 121_t$       c)  $g = 211_t$

S. Farmer, J. Hangan, V. Lanteri, T.E. Mitchell and A.E. Heuer, Case Western Reserve University, Department of Metallurgy and Materials Science, Cleveland Ohio 44106

# ABSTRACT

Intermediate ordered-defect fluorite compounds are an important component of  $ZrO_2$  alloys containing the aliovalent solutes  $MgO$ ,  $CaO$ , or  $Y_2O_3$ . These compounds also form in oxygen-deficient rare earth oxides and in other ternary oxides based on the fluorite structure, and can best be studied by TEM. Examples are given of such phases in the  $MgO-ZrO_2$ ,  $Y_2O_3-ZrO_2$ , and  $CaO-ZrO_2$  systems.

## I. INTRODUCTION AND LITERATURE REVIEW

The high temperature cubic (c) polymorph of  $ZrO_2$  with the fluorite structure (space group  $Fm\bar{3}m$ ) transforms on cooling below  $2370^\circ C$  to a tetragonally distorted fluorite-type structure (space group  $P4_2/nmc$ ) (1). The subsequent tetragonal (t)  $\rightarrow$  monoclinic (m) transformation (below  $1000^\circ C$ ) can have untoward consequences in  $ZrO_2$ -containing ceramics, and so considerable effort, extending over half a century (2), has been expended in "stabilizing" the cubic fluorite phase. For this purpose,  $MgO$ ,  $CaO$ ,  $Y_2O_3$ ,  $Sc_2O_3$ , or any of a host of rare earth oxides are suitable; all show extensive solid solubility in  $ZrO_2$  and act as "fluorite-stabilizers", in that they lower the temperature of the c  $\rightarrow$  t transformation (3).

One consequence of the dissolution of considerable quantities of such aliovalent cation solutes is the generation of massive quantities of charge-compensating oxygen vacancies, one for each divalent cation or two trivalent cations. Dissolution of  $ZrN$  in  $ZrO_2$  also stabilizes the c polymorph (4) and again produces one oxygen vacancy for every two nitrogen anions.

It has been recognized for some time (5) that the massive concentration of point defects thus engendered is not randomly distributed and non-interacting; rather, such systems exhibit significant short-range and long-range ordering (6), resulting in many cases in the formation of ordered defect-fluorite compounds.

The fluorite structure is also notable for its ability to accommodate non-stoichiometry, even in the absence of aliovalent solutes. For example,  $UO_{2-x}$  exists at high temperatures from  $x=0.1$  on the hypostoichiometric side to  $x=0.25$  on the hyperstoichiometric side of  $UO_2$  (7). In rare earth oxides such as  $CeO_2$ ,  $PrO_2$ , and  $TbO_2$ , oxygen-deficiency is prevalent and results in a series of ordered fluorite superstructures (8), which are members of a homologous series  $M_nO_{2n-2}$ , with  $n=7, 9, 10, 11$ , and  $12$ . While all the superstructures are structurally related, only the  $n=7$  example is isostructural in the Ce, Pr, and Tb systems. This  $M_7O_{12}$  structure is very common, and is the structural type for  $Mg_2Zr_5O_{12}$ ,  $Zr_3Sc_4O_{12}$ ,  $Zr_4Y_4O_{12}$ , and  $Zr_7O_8N_4$  (and some of their  $HfO_2$  analogues). (The crystal structure of this group of  $M_nO_{12}$  compounds was first determined for  $UY_6O_{12}$  (9), the isomorphous phase in which the cations are ordered.)

These  $M_7O_{12}$  structures are rhombohedral, all cations having either six or seven oxygen near neighbors. All the 6-coordinated cations lie along the 3-fold axis, forming so-called "Eeven clusters" (one 6-coordinated cation and six 7-coordinated cation (Fig. 1)) which constitute infinite strings in the structure (10). However, not all members of the rare earth homologous series

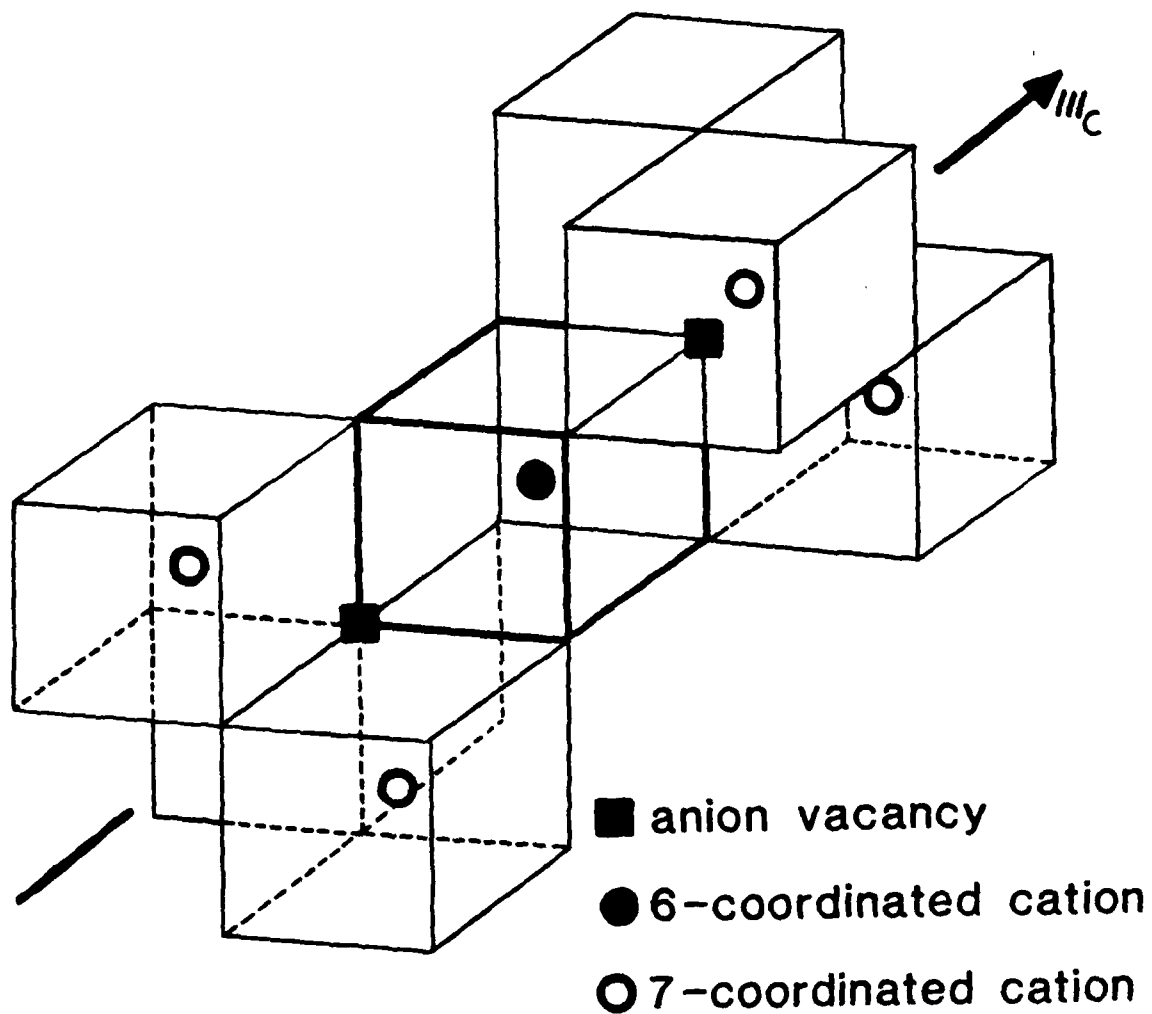


FIG. 1: Bevan cluster of one 6-coordinated cation, two oxygen vacancies, and six 7-coordinated cations. (Only four of the six 7-coordinated cations are indicated).

contain these strings of "Bevan clusters" along  $\langle 111 \rangle_F$  directions; rather the oxygen deficiency is accommodated by the clusters aligning on  $\{135\}$  planes along  $\langle 211 \rangle_F$  directions (11); the  $\{135\}$  planar spacing determines the stoichiometry, being every  $n$ th plane for  $M_2O_{2n-n}$ . It is of interest that infinite strings of 6-coordinated cations and two adjacent oxygen vacancies along all 3-fold axes are also found in the C-type rare earth sesquioxides ( $M_2O_3$ ).

Although numerous intermediate phases have been identified in the binary rare earth oxides, isostructural phases are absent in most mixed rare earth oxide systems. This has been attributed to the sluggish diffusion in the cation sublattice, and the relatively low temperature of the order-disorder transformation so that equilibrium is rarely attained.

In the  $Sc_2O_3$ - $ZrO_2$  and  $Sc_2O_3$ - $HfO_2$  systems, three rhombohedral intermediate phases with disordered cations sublattices form (10). The ordered intermediate phases in the  $ZrN$ -,  $Y_2O_3$ -, and  $MgO$ - $ZrO_2$  binaries are similar to those observed in the  $Sc_2O_3$ - $ZrO_2$  system. In the  $CaO$ - $ZrO_2$  and  $CaO$ - $HfO_2$  binaries, the larger Ca ion causes a different packing of the 6-fold cations and the associated oxygen vacancies; three ordered phases form and all show some degree of cation order.

TEM has been an important, and in some cases an essential, tool in the study of these defect-fluorite oxides and oxynitrides, in part because the x-ray diffraction patterns are so similar, in part because of the incomplete "ordering" which is so common in these systems; and in part because the occurrence of these ordered compounds as fine precipitates requires a technique with good spatial resolution. It is this last advantage of TEM that has motivated our studies, in which the formation of these intermediate compounds as precipitate phases in  $c$ - $ZrO_2$  solid solutions alloyed with  $MgO$ ,  $CaO$ , or  $Y_2O_3$ , has been investigated. Our studies also have relevance to the understanding of the good mechanical properties of partially stabilized  $ZrO_2$ 's (PSZ's) (1).

## II. The $MgO$ - $ZrO_2$ System

There are no stable intermediate compounds in the currently accepted phase diagram for the  $MgO$ - $ZrO_2$  binary system (12). However, the existence of the compound  $Mg_2Zr_5O_{12}$  (and its analogue in the  $MgO$ - $HfO_2$  system) was reported some years ago (13); as noted already, it is isostructural with  $Zr_7O_8N_4$  and  $Zr_3Sc_4O_{12}$ .

The early literature (13, 14) suggested that  $Mg_2Zr_5O_{12}$  could form from a  $c$ - $ZrO_2$  solid solution of the appropriate composition (28.57 m/o  $MgO$ ) but decomposed to  $c$ - $ZrO_2$  and  $MgO$  below  $1850^\circ C$ . More recently, this compound has been formed as a precipitate phase in  $Mg$ -PSZ's containing 8-14 m/o  $MgO$  (15-17).

Our studies have focussed on two compositions, 8.1 and 11.3 m/o  $MgO$ , initially formed as a  $c$ - $ZrO_2$  solid solution and progressively decomposed (diffusionally) by annealing between  $800$  and  $1100^\circ C$ . Decomposition was found to be a sensitive function of previous thermal history.

Heat treatment of either composition (as a single phase solid solution) at  $800^\circ C$  for one hour, followed by  $1100^\circ C$  for 5 hours, induced growth of coherent  $t$ - $ZrO_2$  precipitates and precipitates of the ordered phase  $Mg_2Zr_5O_{12}$  within the  $c$ - $ZrO_2$  matrix (Figs. 2a and b). The  $t$ - $ZrO_2$  phase actually nucleated and grew to  $\sim 5$  nm on cooling from a previous heat treatment at  $1800^\circ C$ , during which the solid solution was homogenized; it further coarsened to 50-20 nm during the  $800/1100^\circ C$  "aging". The equilibrium phases for these temperatures,  $m$ - $ZrO_2$  and  $MgO$ , are not much in evidence after such short

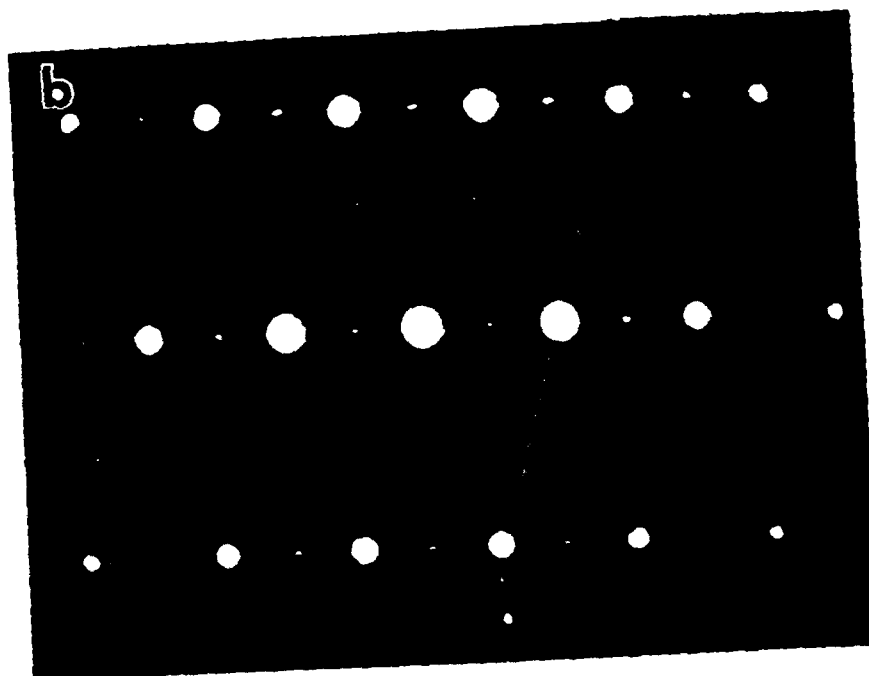
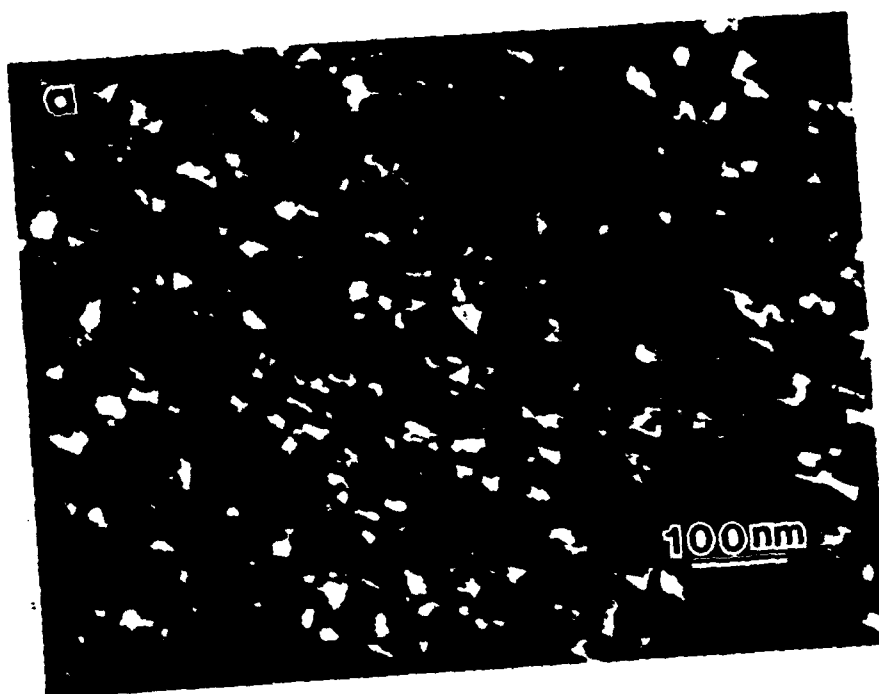


FIG. 2:  $\text{Mg}_2\text{Zr}_5\text{O}_{12}$  precipitate in Mg-PSZ. (a) is a dark field image of a single precipitate variant in a  $\underline{c}$ - $\text{ZrO}_2$  matrix and (b) is a  $\langle 310 \rangle_{\text{F}}$  zone axis diffraction pattern. The most intense ("fundamental") reflections are from the  $\underline{c}$ - $\text{ZrO}_2$  matrix, while the weakest reflections are from two variants of  $\text{Mg}_2\text{Zr}_5\text{O}_{12}$ . The arrowed reflections are due to  $\underline{t}$ - $\text{ZrO}_2$  precipitates, which are out of contrast in (a).



aging times.

If the aging time at 1100°C is increased to 10 hours, the  $\text{Mg}_2\text{Zr}_5\text{O}_{12}$  does not coarsen appreciably, but a good deal of  $\text{m-ZrO}_2$  is found at grain boundaries of the polycrystalline Mg-PSZ. This grain boundary "phase" is actually a eutectoid decomposition product consisting of  $\text{m-ZrO}_2$  plus MgO, which advances into the surrounding grains as a coupled growth product (Fig. 3), and consumes the  $\text{c-ZrO}_2$  and its  $\text{t-ZrO}_2$  and  $\text{Mg}_2\text{Zr}_5\text{O}_{12}$  precipitates. The ordered compound  $\text{Mg}_2\text{Zr}_5\text{O}_{12}$  is therefore clearly a metastable decomposition product, although it may have a region of stability at some other temperature on the equilibrium phase diagram.

The conditions under which the  $\text{Mg}_2\text{Zr}_5\text{O}_{12}$  formed were quite specific--solution annealing at  $T > 1600^\circ\text{C}$ , followed by the 300/1100°C heat treatment. The lower temperature heat treatment is necessary to nucleate this phase; 300°C was usually used although 900°C was also found to be suitable. It was of interest that nucleation and growth of  $\text{Mg}_2\text{Zr}_5\text{O}_{12}$  could be suppressed by an intermediate heat treatment. For example, prior heating at 1600°C for 1 hr, followed by furnace cooling, prevented the formation of  $\text{Mg}_2\text{Zr}_5\text{O}_{12}$  during the 300/1100°C aging. If such material is subsequently given a second solution annealing of 2 hrs at 2100°C in an oxy-acetylene furnace, followed by rapid cooling ( $\sim 5$  min) to room temperature, aging at 1100°C leads to the ready formation of  $\text{Mg}_2\text{Zr}_5\text{O}_{12}$  without the need for a lower temperature nucleation heat treatment. Similar behavior has previously been noted concerning the formation of ordered defect-fluorite phases in some rare earth oxide systems (12), in which a suitable quenched-in high temperature cation arrangement is necessary to permit nucleation of particular ordered phases.

### III. The $\text{ZrO}_2\text{-Y}_2\text{O}_3$ System

Two intermediate ordered compounds are known in the  $\text{ZrO}_2\text{-Y}_2\text{O}_3$  system, an  $\text{M}_7\text{O}_{12}$  compound at 40 m/o  $\text{Y}_2\text{O}_3$  and an  $\text{M}_{11}\text{O}_{18}$  phase at 75 m/o  $\text{Y}_2\text{O}_3$ . The most recent phase diagrams for this system (19-21) suggest that the former phase should be ubiquitous in high  $\text{ZrO}_2$  compositions. However, a number of TEM studies have been reported of technologically interesting compositions containing between 2 and 8 m/o  $\text{Y}_2\text{O}_3$  (22, 23); only  $\text{m}$ ,  $\text{t}$ , and  $\text{c-ZrO}_2$  polymorphs have been reported. This is probably due to the low temperature of the eutectoid in this system.

Recently, however, we have found evidence of an unusual ordering reaction in a 6.3 m/o Y-PSZ (the composition was determined by calibrated EDS analysis) (24). This material is a commercial furnace tube; we presume it was fired at a temperature above 1500°C and cooled slowly to room temperature.

Most grains have  $\text{t-symmetry}$  but contain anti-phase domain boundaries (Fig. 4), a result of a diffusionless  $\text{c} \rightarrow \text{t}$  transformation (1). Such microstructures are common in other  $\text{Y}_2\text{O}_3\text{-ZrO}_2$  ceramics (23). Some  $\text{t-ZrO}_2$  "colonies" are also present, each colony consisting of stacked plates sharing a  $\{101\}$  habit plane, alternate plates being twin-related (their  $\text{c-axes}$  are rotated by  $90^\circ$ ). Such colonies are also common in  $\text{Y}_2\text{O}_3\text{-ZrO}_2$  samples heat treated in the two-phase  $\text{t}$  plus  $\text{c}$  field (22, 25).

A few grains in this polycrystalline ceramic possessed a different structure, one not observed previously in any prior study of lower  $\text{Y}_2\text{O}_3$  material. The fundamental reflections in SAD patterns (Fig. 5) show tetragonal symmetry, and satellite reflections are seen about each of the strong fundamental reflections. Very weak superlattice reflections are also visible in  $\langle 111 \rangle_F$  orientations.

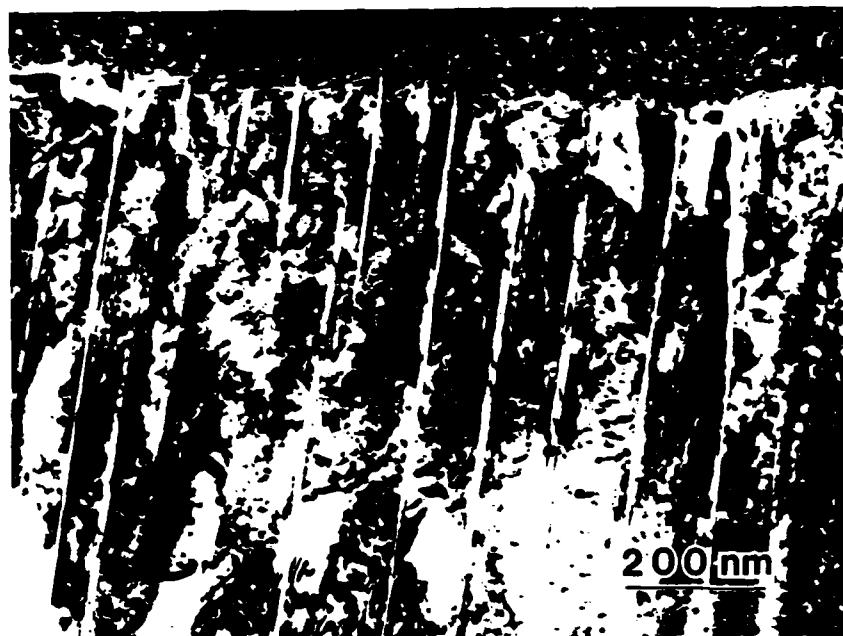


FIG. 3: Eutectoid decomposition product of  $m$ -ZrO<sub>2</sub> and MgO in Mg-PSZ. The grain being consumed is at the top of the micrograph.

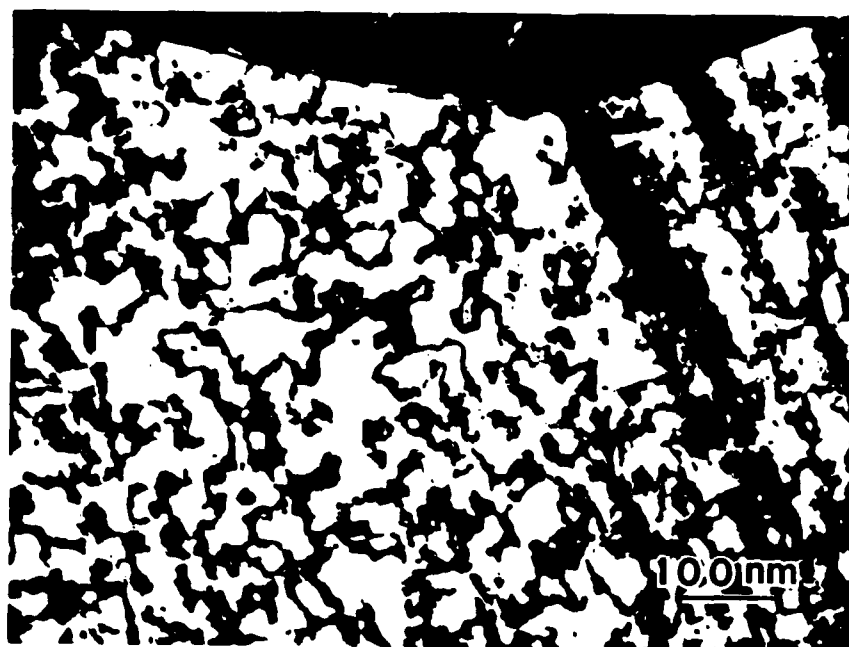


FIG. 4: Antiphase domain boundaries arising from a diffusionless but non-martensitic  $c \rightarrow t$  transformation in 6.3 m/o Y-PSZ.

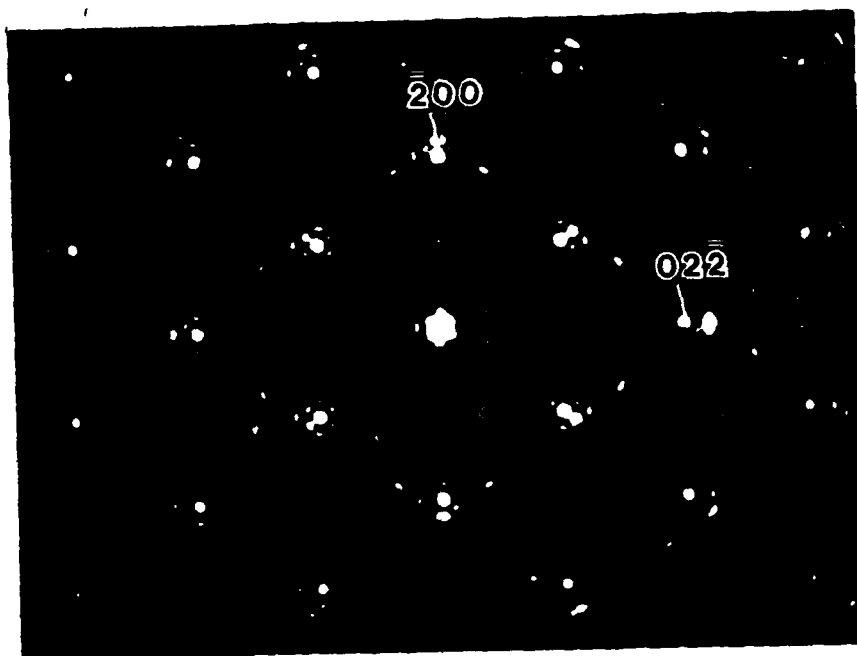


FIG. 5:  $\langle 011 \rangle_F$  zone axis diffraction pattern of possible ordered phase in 6.3 m/o Y-PSZ.

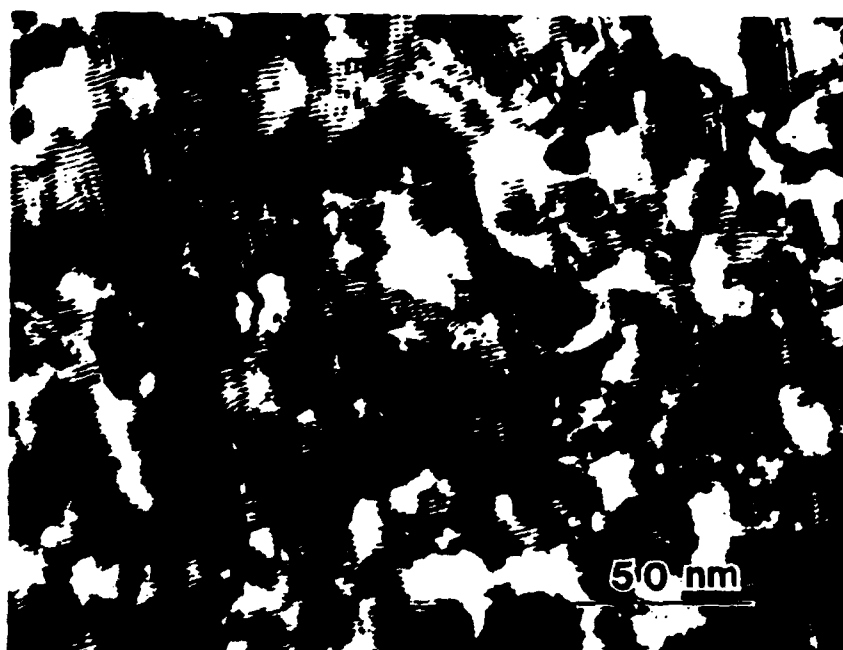


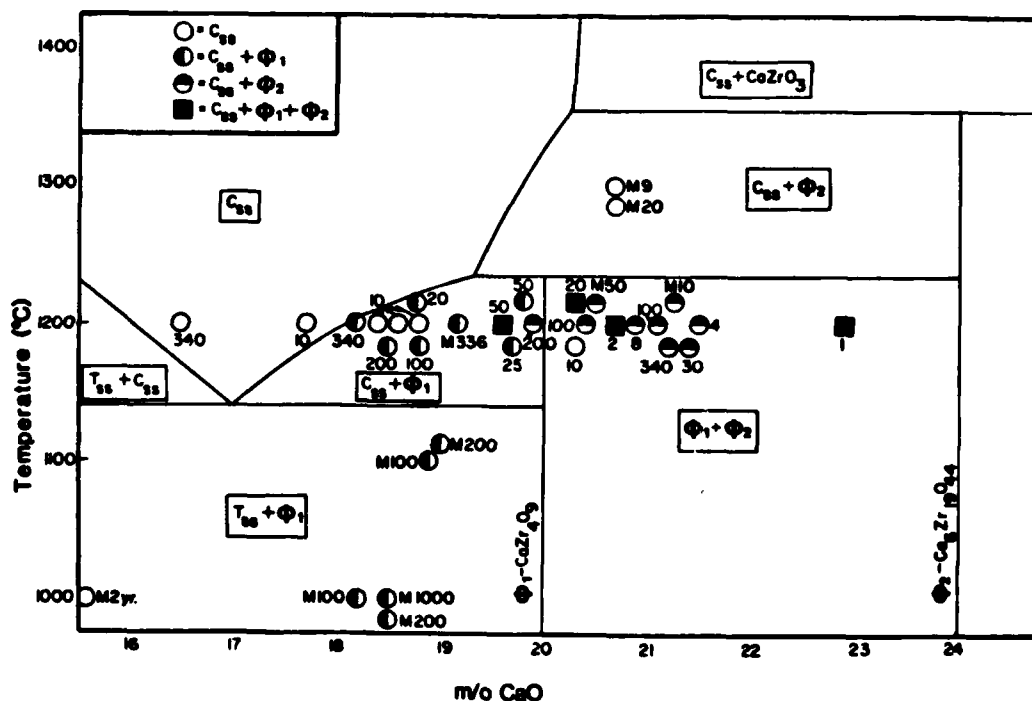
FIG. 6: Bright field image of 6.3 m/o Y-PSZ oriented to a  $\langle 111 \rangle_F$  zone axis orientation.

A bright field image of the region giving rise to the diffraction pattern in Figure 5 appears in Figure 6. The fringes correspond in spacing and direction to the satellite spacing in the diffraction pattern. EDS analysis confirmed that the grains showing this superstructure were richer in  $Y_2O_3$  than the 6.3 m/o matrix. Further work is continuing on the identification of this phase, and particularly on the thermal history required for its formation.

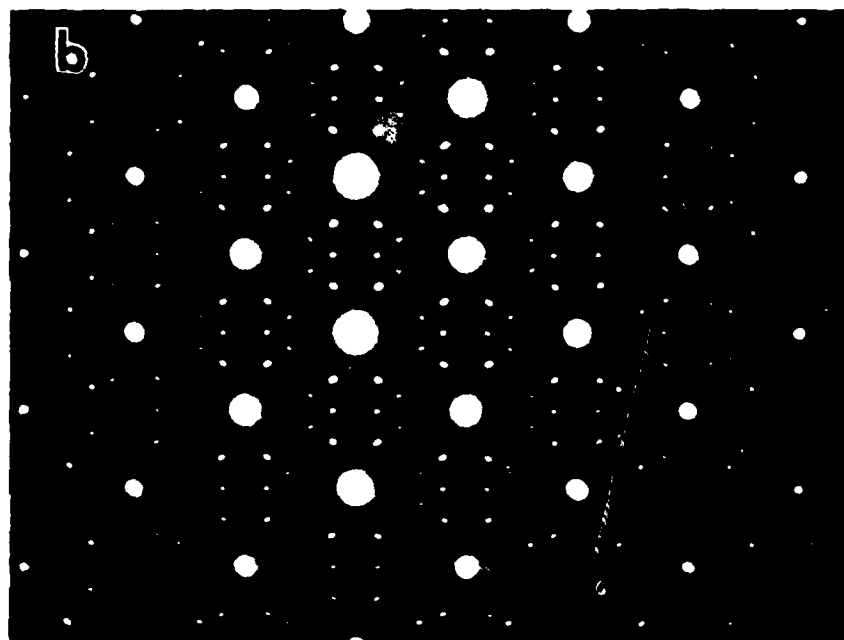
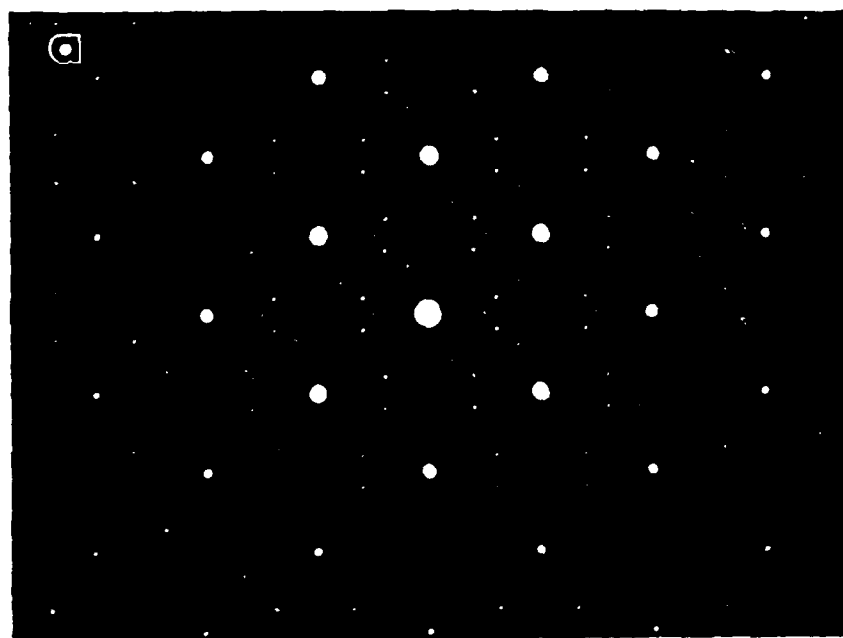
#### IV. The $CaO-ZrO_2$ System

Three ordered compounds are known in the  $CaO-HfO_2$  system, two of which have analogues in the  $CaO-ZrO_2$  system, namely  $\phi_1$  ( $Ca_{10}O_{16}$ ),  $\phi$  ( $Ca_2Hf_7O_{16}$ ) (the  $ZrO_2$  analogue apparently does not form), and  $\phi_2$  ( $Ca_{19}Zr_{44}O_{144}$ ). All involve different arrangements of 6-coordinated cations.  $\phi_1$  contains linked clusters of three such cations (26),  $\phi_2$  has the cations linked in helical chains (26), and  $\phi$  has isolated cations (27). In some senses, the degree of cation order increases from  $\phi_1$  to  $\phi_2$  to  $\phi$ . When present as precipitate phases in  $CaO-ZrO_2$  samples, they can readily be distinguished by electron diffraction (Fig. 7).

The recently determined phase diagram for this system (28) is shown in Figure 8. The data in this figure were obtained from 18-22 m/o  $CaO$  skull-melted single crystals heat treated at 1100-1300°C for up to 336 hours (29, 30); the compositions shown were determined by EDS, using a  $CaZrO_3/c-ZrO_2$  eutectic as a standard for chemical calibration standards; the compositions are thought to be accurate to better than  $\pm 0.5$  m/o. The absence of appreciable quantities of  $\phi_1$  in compositions between 20 and 24 m/o  $CaO$  aged for long times suggests that  $\phi_1$  may be a metastable phase, in spite of the fact that it coarsened from elongated striated particles into the blocky



- FIG. 8: Phase diagram for  $CaO-ZrO_2$  system (28-30) showing compositions that precipitated either  $\phi_1$  or  $\phi_2$  on aging at elevated temperatures.



— FIG. 7:  $\langle 011 \rangle_F$  zone axis diffraction patterns of CaO-stabilized  $ZrO_2$  containing (a)  $\phi_1$  precipitate (19 m/o CaO) and (b)  $\phi_2$  precipitates (21 m/o CaO).

precipitates in Figure 9 in compositions leaner in CaO than 20 m/o aged for long times (30).

The morphology of  $\phi_2$  precipitates in the CaO-rich crystals studied is shown in Figure 10. The  $\phi_2$  particles are equiaxed and exhibit higher coherency strains in bright field images (not shown here) than do  $\phi_1$ , in keeping with the notion that  $\phi_1$  is metastable (31) but nucleates readily. If this is correct, the assemblage c-ZrO<sub>2</sub> plus  $\phi_2$  must be only modestly more stable than the assemblage c-ZrO<sub>2</sub> plus  $\phi_1$ , which combined with the high coherency strains, renders  $\phi_2$  more difficult to nucleate than  $\phi_1$ .

#### ACKNOWLEDGMENT

Our research has been supported by the National Science Foundation (the MgO-ZrO<sub>2</sub> and CaO-ZrO<sub>2</sub> systems) and the AFOSR (the Y<sub>2</sub>O<sub>3</sub>-ZrO<sub>2</sub> system).

1. A.H. Heuer and M. Rühle, Adv. in Ceramics, Science and Technology of Zirconia, eds. N. Claussen M. Rühle and A.H. Heuer, The Amer. Cer. Soc., (1984). To be published.
2. O. Ruff and F. Ebert; Z. anorg. allg. Chem., 180, 19 (1929).
3. A.H. Heuer, "Advances in Ceramics 3, Science and Technology of Zirconia", ed. A.H. Heuer and L.W. Hobbs, Amer. Cer. Soc., 98-115 (1981).
4. N. Claussen, R. Wagner, L.J. Gouckler and G. Petzow, J. Amer. Cer. Soc., 61, 369-370 (1968).
5. R.E. Carter and W.L. Roth; in "Electromotive Force Measurements in High Temperature Systems. Institution of Mining and Metallurgy, 125-144 (1968).
6. M. Morinaga, J.B. Cohen and J. Faber, Jr., Acta Cryst., A-36, 520-530 (1980).
7. K. Hagamark and M. Broli, J. Inorg. Nucl. Chem., 28, 3632 (1966).
8. L. Eyring, in "Nonstoichiometric Oxides", ed. O.T. Sorensen, Acad. Press Inc., 337-398 (1981).
9. S.F. Bartram, Inorg. Chem., 5, 749-754 (1966).
10. M.R. Thornber, D.J.M. Bevan and J. Graham, Acta. Cryst., B24, 118-1191 (1968).
11. R.T. Tvenge and L. Eyring, J. of Solid State Chem., 29, 165-179 (1979).
12. C.F. Grain, J. Amer. Cer. Soc., 50 (6), 288-290 (1967).
13. C. Delamarre, "Hafnium Dioxide - MO Systems. Comparison with Corresponding Systems Based on Zirconia", Rev. Int. Hautes Temper. et. Refract. 9 (2), 209-224 (1972).
14. O. Yoranovitch and C. Delamarre, Mat. Res. Bull., 11 (8), 1005-1010 (1976).
15. R.H.J. Hannink and R.C. Garvie, J. Mat. Sci. 17, 2637-2643 (1982).
16. R.H.J. Hannink, J. Mat. Sci. 18, 457-470 (1983).
17. S.C. Farmer, L.H. Schoenlein and A.H. Heuer, J. Amer. Ceram. Soc. 66, 107-109 (1983).
18. D.J.M. Bevan and E. Summerville, "Handbook of the Physics and Chemistry of Rare Earths", Vol. 3, ed. C.A. Gschneider and L. Eyring, North-Holland Publishing Co, 401-523 (1979).
19. H.G. Scott, J. Mat. Sci. 10 (1975) 1527.
20. V.S. Stubican and S.P. Ray, J. Amer. Ceram. Soc. 60 (1977) 534.
21. C. Pascual and P. Duran, J. Amer. Ceram. Soc. 66 (1983) 23.
22. V. Lanteri, T.E. Mitchell and A.H. Heuer, in Ref. 1.
23. M. Rühle, N. Claussen and A.H. Heuer, in Ref. 1.
24. V. Lanteri, T.E. Mitchell, A.H. Heuer and M. Rühle, to be published.
25. R. Chaim, M. Rühle and A.H. Heuer, to be published.
26. J.G. Allpress, H.J. Rossell and H.G. Scott, J. Solid State Chem., 14, 264-273 (1975).
27. H.J. Rossell and H.G. Scott, J. Solid State Chem., 13, 345-350 (1975).
28. J.R. Hellmann and V.S. Stubican, J. Amer. Cer. Soc., 66, 260-264 (1983).
29. J.M. Marder, T.E. Mitchell and A.H. Heuer, Acta Metall. 31, 387 (1983).
30. J. Hangan, T.E. Mitchell and A.H. Heuer, in Ref. 1.
31. V.S. Stubican, G.S. Corman, J.R. Hellmann and G. Senft, in Ref. 1.

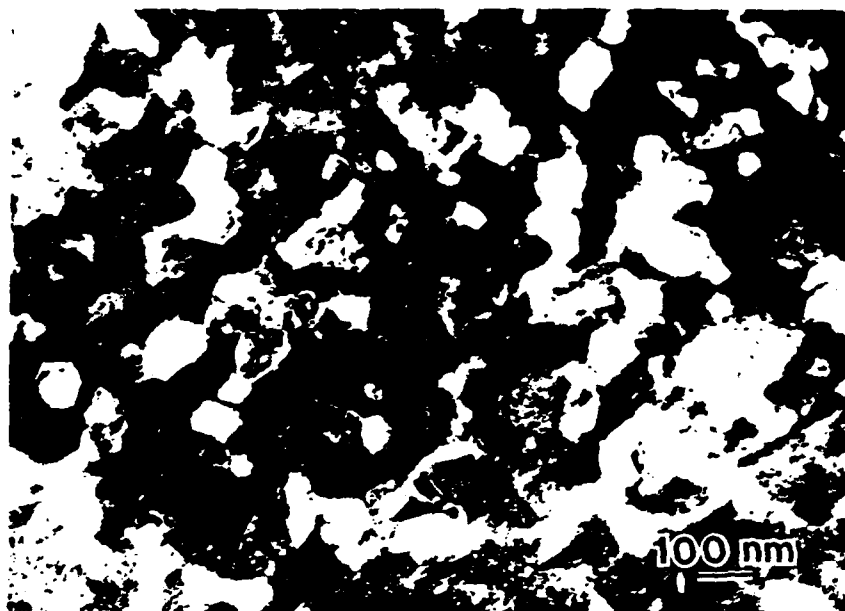


FIG. 9:  $\varnothing_1$  precipitates in 19 m/o CaO-stabilized  $\text{ZrO}_2$  aged 336 hours at  $1200^\circ\text{C}$ .



FIG. 10:  $\varnothing_2$  precipitates in 21 m/o CaO-stabilized  $\text{ZrO}_2$  aged 100 hours at  $1200^\circ\text{C}$ .

## HREM STUDIES OF COHERENT AND INCOHERENT INTERFACES IN $\text{ZrO}_2$ -CONTAINING CERAMICS: A PRELIMINARY ACCOUNT

A.H. HEUER, S. KRAUS-LANTERI, P.A. LABUN, V. LANTERI and T.E. MITCHELL

Department of Metallurgy and Materials Science, Case Western Reserve University, Cleveland, Ohio 44106, USA

Received 18 June 1985; presented at Symposium January 1985

HREM has been applied to the study of interfaces in various  $\text{ZrO}_2$ -containing ceramics. In dispersion-toughened ceramics, such as  $\text{ZrO}_2$ -toughened  $\text{Al}_2\text{O}_3$ , fine  $\text{ZrO}_2$  particles can be either *intra-* or *inter-* granular. *Intragranular*  $\text{ZrO}_2$  particles form *incoherent* interfaces with their  $\text{Al}_2\text{O}_3$  hosts, and such interfaces have been imaged by HREM. The interfaces between *inter-* granular  $\text{ZrO}_2$  particles and  $\text{Al}_2\text{O}_3$  grains are generally covered with a glassy phase, 1–3 nm in thickness, and evidence for this phase is also present in HREM images. If the  $\text{ZrO}_2$  transforms from tetragonal to monoclinic symmetry during cooling from the fabrication temperature, it is generally twinned, and the *coherent* twin boundaries have also been imaged in HREM. Tetragonal precipitate colonies which occur on annealing certain  $\text{ZrO}_2$ - $\text{Y}_2\text{O}_3$  alloys have also been studied. Each colony consists of alternating variants which are  $90^\circ$  twins. HREM shows that the twin boundaries are highly coherent with a slight tilt between the variants. The “matrix” between the tetragonal colonies is shown by optical diffraction analysis of the HREM images to have tetragonal rather than cubic symmetry, indicating the occurrence of a diffusionless cubic  $\rightarrow$  tetragonal transformation.

### 1. Introduction

$\text{ZrO}_2$ -containing ceramics have attracted much attention in recent years because of their unusual mechanical and electrolytic properties [1,2]. Their considerable potential for high-technology structural applications derives from the phenomenon of *transformation toughening*. Briefly,  $\text{ZrO}_2$  is polymorphic, the three polymorphs being shown in fig. 1 [3]. The high-temperature form is cubic and is isostructural with  $\text{CaF}_2$  (fluorite structure). At temperatures below  $\sim 2350^\circ\text{C}$  for pure  $\text{ZrO}_2$ , or at temperatures considerably lower for  $\text{ZrO}_2$  alloys, the cubic polymorph (*c*- $\text{ZrO}_2$ ) transforms to a tetragonally distorted version of the fluorite structure shown in fig. 1b (*t*- $\text{ZrO}_2$ ). At still lower temperatures, *t*- $\text{ZrO}_2$  transforms martensitically to the monoclinic structure shown in fig. 1c (*m*- $\text{ZrO}_2$ ). This martensitic *t*  $\rightarrow$  *m* transformation is the origin of transformation toughening in  $\text{ZrO}_2$ -containing ceramics, as will now be described.

In suitably fabricated ceramics, particularly if the *t*- $\text{ZrO}_2$  is present as fine particles, the start or  $M_s$  temperature of the martensitic transformation,

which is  $\leq 1000^\circ\text{C}$  in pure bulk  $\text{ZrO}_2$ , can be reduced to below room temperature, i.e., the *t*- $\text{ZrO}_2$  is retained metastably at room temperature. However, the *t*  $\rightarrow$  *m* transformation can be induced by external stresses, for example, the stress field associated with a propagating crack. This stress-induced tetragonal-to-monoclinic transformation thus “shields” the crack tip from the applied stresses and is the origin of the improved strength and toughness of transformation-toughened  $\text{ZrO}_2$ -containing ceramics.

It should be clear from this introduction that the type, amount, morphology and distribution of the  $\text{ZrO}_2$  polymorphs within  $\text{ZrO}_2$ -containing ceramics are of prime importance, and both homophase ( $\text{ZrO}_2/\text{ZrO}_2$ ) and heterophase ( $\text{ZrO}_2$  particle/non- $\text{ZrO}_2$  matrix) interfaces are of interest. In fact, such studies of interfaces in polycrystalline, polyphase ceramics are crucial for understanding the variety of diffusional and diffusionless transformations that are important when considering microstructural evolution during fabrication and performance during service. Inasmuch as HREM can play a vital role in understanding



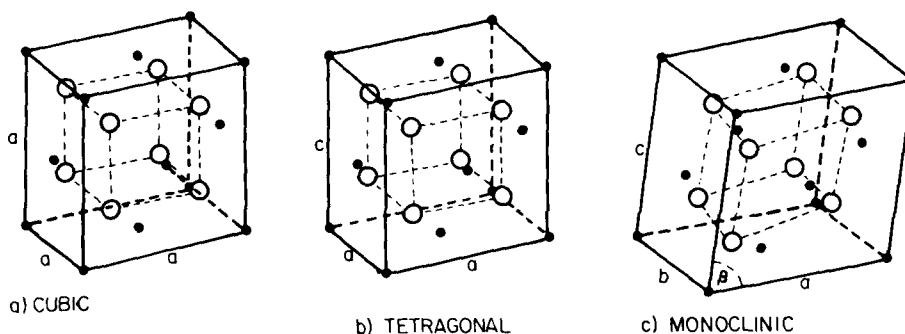


Fig. 1. Three polymorphs of  $\text{ZrO}_2$ : (a) cubic phase; (b) tetragonal phase,  $c/a \approx 1.02$ ; (c) monoclinic phase. The small filled spheres are Zr atoms, the large open spheres are oxygen.

these technologically important ceramics, we have begun a broad program using high-resolution electron microscopy to study interfaces in such ceramics.

## 2. Experimental procedures

15 vol%  $\text{ZrO}_2$ -toughened  $\text{Al}_2\text{O}_3$  (ZTA) specimens were obtained from Dr. N. Claussen (Max-Planck-Institut für Metallforschung, Stuttgart, Fed. Rep. of Germany). The starting powders were Alcoa A-16  $\text{Al}_2\text{O}_3$  and Magnesium Electron ARZ52  $\text{ZrO}_2$ . Processing consisted of attritor milling for 12 h, followed by hot pressing at  $1550^\circ\text{C}$  for 30 min; the density of the resulting ceramic was 99.5% of theoretical.

Single crystal skull-melted  $\text{ZrO}_2$ -8 wt%  $\text{Y}_2\text{O}_3$  was obtained from the Ceres Corporation. This material was then heat-treated for 50 h at  $1600^\circ\text{C}$  and furnace-cooled; Laue back-reflection photographs were used to orient the crystal to a  $\langle 111 \rangle$  zone.

Both materials were prepared for TEM examination using standard techniques, i.e. diamond-wafering thin slices, grinding and polishing to approximately  $50\ \mu\text{m}$  thickness, followed by ion-beam thinning to electron transparency. A thin carbon coat was sputtered on one surface before insertion into a JEOL 200CX having a  $C_s$  of 1.1 mm and a point resolution of  $\leq 0.24\ \text{nm}$ . An Intellect 200 image analysis system is used for

on-line image processing; Skarnulis' CELLS program [4] is available for image simulation.

## 3. Zirconia-toughened alumina

ZTA, an example of a wider class of dispersion-toughened ceramics, is one of the three useful types of  $\text{ZrO}_2$ -containing ceramics. These materials typically contain 15 vol%  $\text{ZrO}_2$  in a fine-grained  $\text{Al}_2\text{O}_3$  matrix; the  $\text{ZrO}_2$  can be *inter-* or *intragranular* and the propensity for undergoing the martensitic transformation depends markedly on the morphology of the  $\text{ZrO}_2$  particles [5]. Furthermore, the stability of *t*- $\text{ZrO}_2$ , i.e. its resistance to undergoing the martensitic transformation, involves stress concentrations at interfaces. It now appears that nucleation of the *t*  $\rightarrow$  *m* martensitic transformation is always stress-assisted [6], and the magnitude of these stresses is very sensitive to particle morphology [7]. Understanding of the *t*  $\rightarrow$  *m* martensitic transformation depends on increased knowledge of the interface structure, and a variety of  $\text{ZrO}_2$ - $\text{Al}_2\text{O}_3$  interfaces have been imaged with high-resolution electron microscopy.

The first example is shown in fig. 2. A roughly spherical *m*- $\text{ZrO}_2$  particle is completely enclosed within an  $\text{Al}_2\text{O}_3$  grain. As has been discussed elsewhere [8], this morphology arises from "break-away" grain growth of  $\text{Al}_2\text{O}_3$  grain boundaries during densification or extended high-temperature

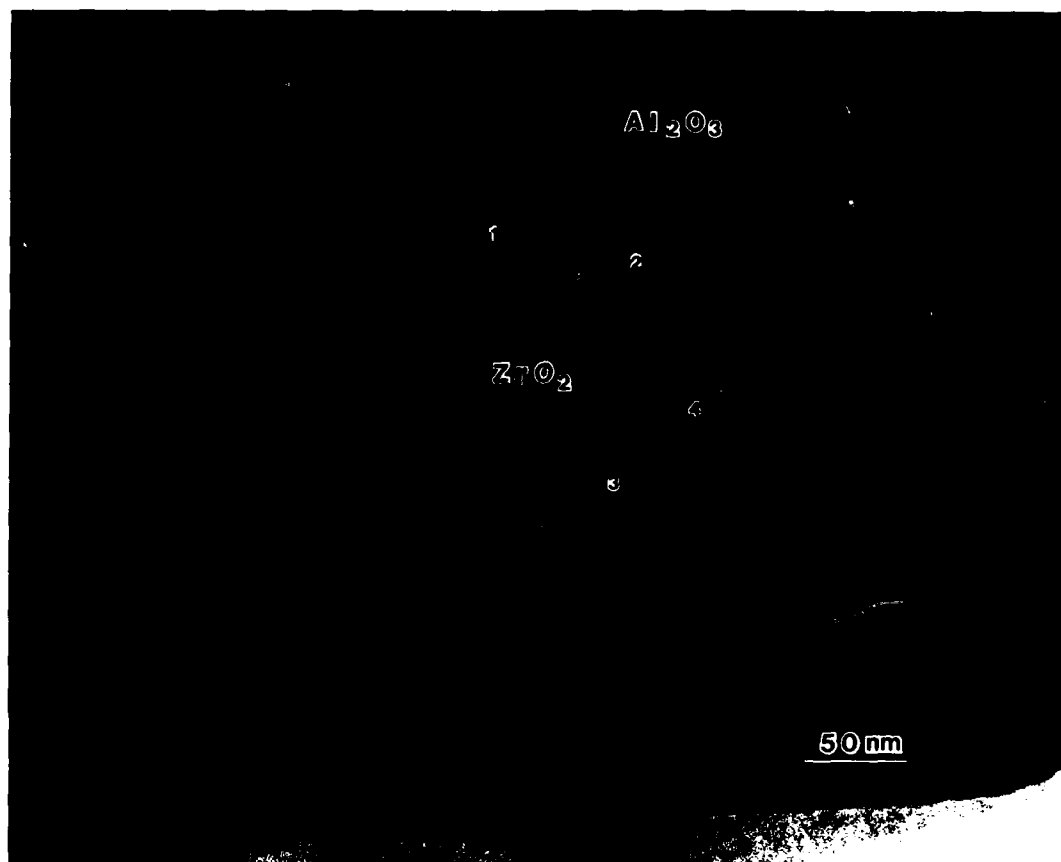


Fig. 2. Bright-field micrograph of intragranular  $\text{ZrO}_2$  particle in  $\text{Al}_2\text{O}_3$  grain.

annealing. While particles such as these are generally resistant to the martensitic transformation in bulk ceramics [5], foil preparation has been found to induce the  $t \rightarrow m$  transformation, especially if, as in the present case, the  $\text{ZrO}_2$  is free of any "stabilizer" solute. Thus, the  $\text{ZrO}_2$  particle shown in fig. 2 has  $m$  symmetry, having transformed during foil preparation, and a conventional selected-area diffraction pattern of both the  $\text{ZrO}_2$  particle and the  $\text{Al}_2\text{O}_3$  matrix (not shown here) reveals the fortunate circumstance that the particle and matrix are oriented such that both are within a few degrees of a low-index zone axis orientation, [001] for  $\text{ZrO}_2$  and [0001] for  $\text{Al}_2\text{O}_3$ . Furthermore, the foil is of relatively uniform thickness over the

whole area of fig. 2, and could be imaged in HREM. A structure image of the  $\text{ZrO}_2$  particle after tilting to the exact [001] orientation is shown in fig. 3, along with an image calculated by computer simulation. It is clear that the image matching in this particular instance is acceptable. We also hope to model the interfaces (at regions 1–4 in fig. 2 to be shown next), although such interface simulations have not yet been completed.

The particle–matrix interface is shown at higher resolution in fig. 4: the  $\text{ZrO}_2$  is oriented exactly on the zone axis in fig. 4a, while the  $\text{Al}_2\text{O}_3$  is oriented exactly on the zone axis in fig. 4b. The feature marked F in figs. 4a and 4b is a fault in the  $m$ - $\text{ZrO}_2$  which we have not yet analyzed. The

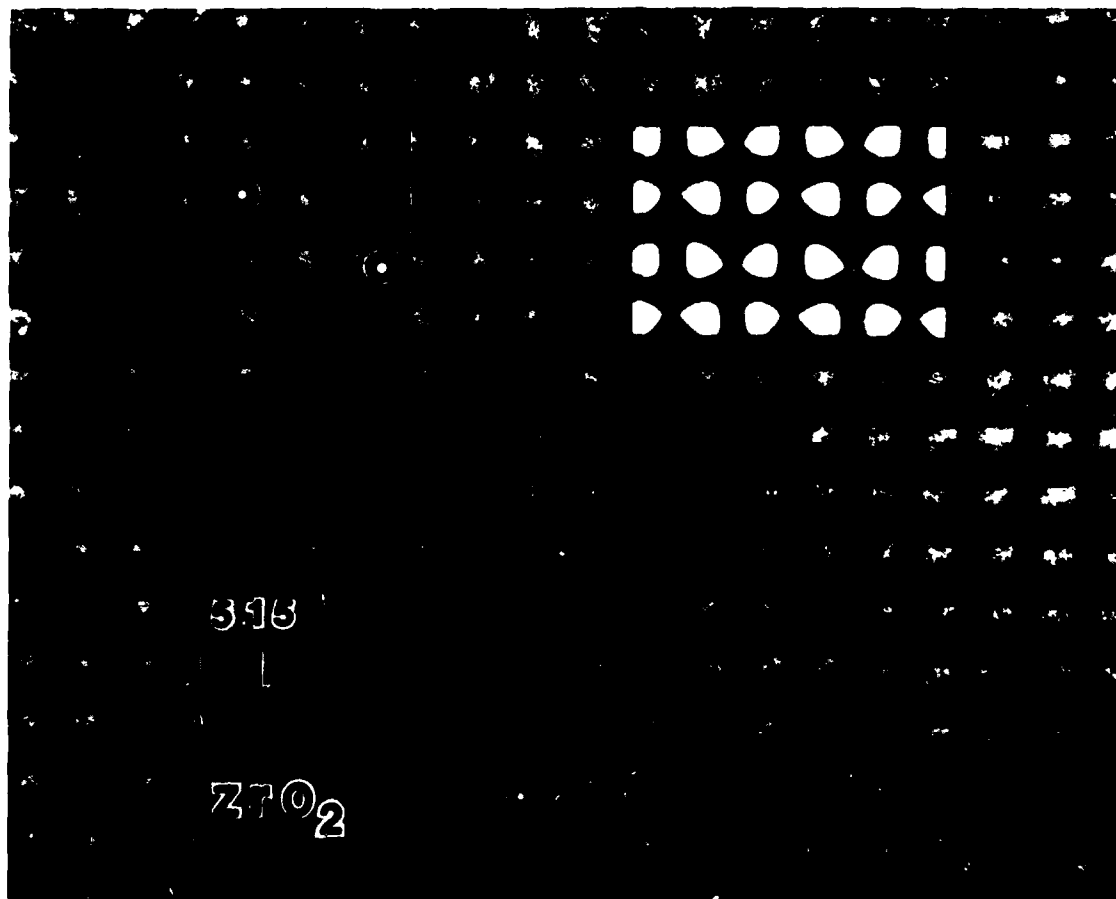


Fig. 3. High-resolution image of  $[001]_m \text{ZrO}_2$ , with calculated image match. The unit cell is shown.

features marked 1 and 2 in fig. 4a denote particular interface regions which are shown at higher magnifications in fig. 5. We believe that the interface is most nearly parallel to the electron beam in region 1 in fig. 5a, and expect that sensible image interpretation of the atomic structure of this interface will be possible. On the other hand, the region shown in fig. 5b is judged to be uninterpretable because the interface is inclined to the electron beam; no further analysis is being contemplated for this image.

Slight tilting brings the  $\text{Al}_2\text{O}_3$  grain into its symmetry position, and fig. 6 shows two regions (marked 3 and 4) on the opposite side of the

faulted particle. Fig. 6a shows an area in which the interface is more or less parallel to the electron beam and for which we hope to provide suitable image simulations in the near future. Fig. 6b, on the other hand, shows a region of interface that is inclined to the electron beam and is judged unsuitable for further interpretation. Figs. 5a and 6a are remarkable in that they show the images extend right to the  $\text{Al}_2\text{O}_3$ - $\text{ZrO}_2$  interface, and that this *incoherent* interphase interface appears to accommodate the two dissimilar lattices without undue difficulty.

With regard to transformation toughening, intergranular particles are preferred in  $\text{ZrO}_2$ -

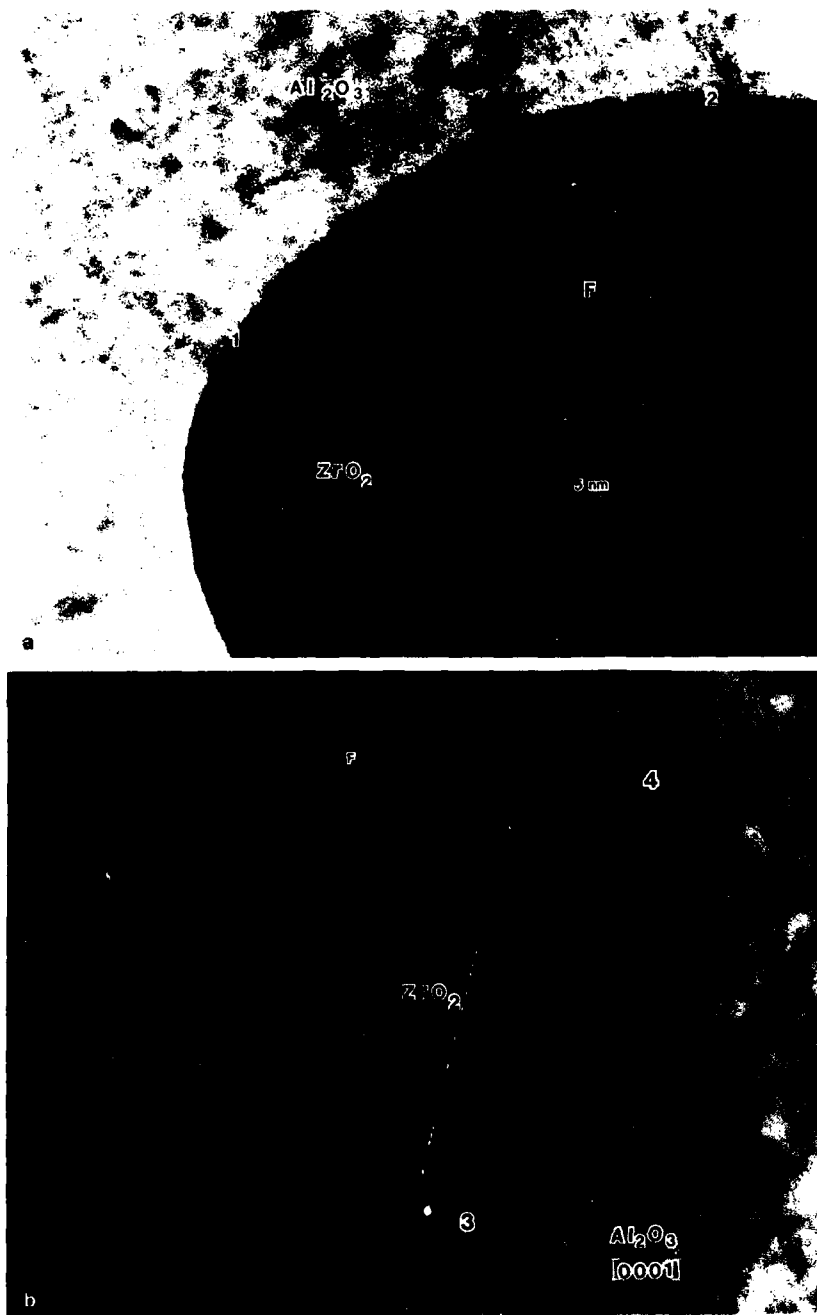


Fig. 4. (a) Higher-magnification micrograph of ZrO<sub>2</sub> particle in fig. 2 with interfacial regions 1 and 2 indicated. F is a fault in the particle. The foil is oriented so that ZrO<sub>2</sub> is exactly on the [001] orientation. (b) ZrO<sub>2</sub> particle with interfacial regions 3 and 4 indicated. The foil is oriented so that Al<sub>2</sub>O<sub>3</sub> is exactly on the [0001] orientation.



Fig. 5. (a) High-resolution image of interfacial region 1. (b) High-resolution image of interfacial region 2.

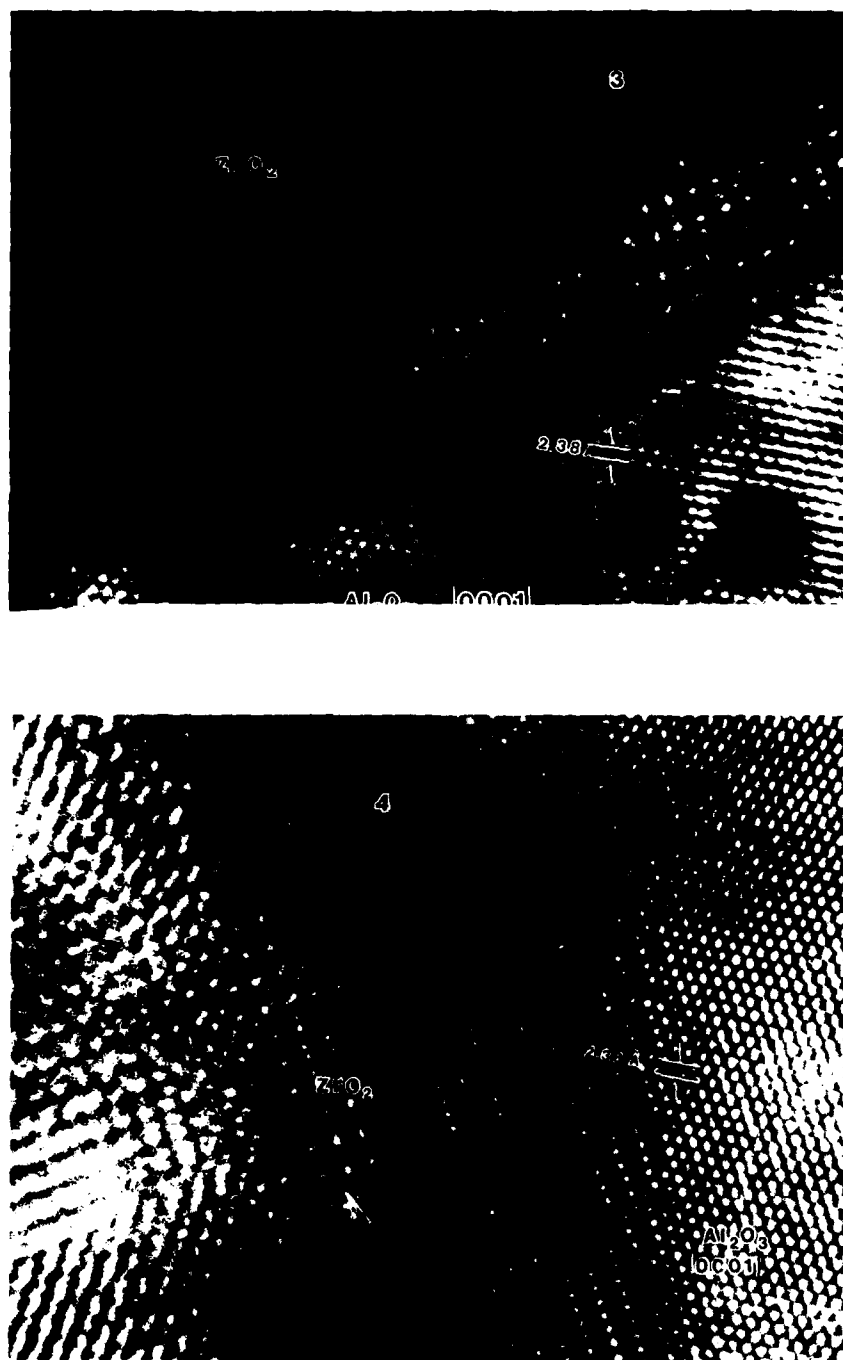


Fig. 6. (a) High-resolution image of interfacial region 3. (b) High-resolution image of interfacial region 4.

toughened  $\text{Al}_2\text{O}_3$ , and the sample of figs. 2–6 in fact contains more inter- than intragranular particles. However, it should be mentioned that virtually all  $\text{Al}_2\text{O}_3/\text{Al}_2\text{O}_3$  grain boundaries and  $\text{Al}_2\text{O}_3/\text{ZrO}_2$  intergranular boundaries in this sample are coated with a thin film (1–3 nm) of a  $\text{SiO}_2$ -containing amorphous phase (the  $\text{SiO}_2$  impurity having been introduced during processing); such a grain boundary phase appears to be ubiquitous in all the  $\text{ZrO}_2$ -toughened  $\text{Al}_2\text{O}_3$ 's studied to date. This glassy phase can best be imaged by forming a dark field image using diffuse inelastically scattered electrons. The glass is thus located at the bright regions in fig. 7 and the particular arrowed feature is glass along an  $\text{Al}_2\text{O}_3$ – $\text{Al}_2\text{O}_3$  grain boundary. The presence of

such an amorphous phase at the  $\text{Al}_2\text{O}_3$ – $\text{ZrO}_2$  interface does not detract from detailed HREM studies of the interfaces. A HREM image of a twinned  $m$ - $\text{ZrO}_2$  particle in this sample is shown in fig. 8. (This is not the same region as shown in fig. 7.) The  $\text{ZrO}_2$  particle is extensively twinned, the twinning occurring during spontaneous transformation on cooling following fabrication. This twinning occurs to minimize the shape strain of the particle during the martensitic transformation, and is present in virtually all  $m$ - $\text{ZrO}_2$  particles, except those which have transformed in a thin foil, as in fig. 2.

The orientations of the two  $\text{Al}_2\text{O}_3$  grains and the several twinned "domains" of the  $\text{ZrO}_2$  particle were determined by taking optical diffracto-



Fig. 7. Diffuse dark-field micrograph of intergranular  $\text{ZrO}_2$  in an  $\text{Al}_2\text{O}_3$  matrix, showing glassy phase at grain boundaries. (The arrowed region is an  $\text{Al}_2\text{O}_3/\text{Al}_2\text{O}_3$  boundary.)

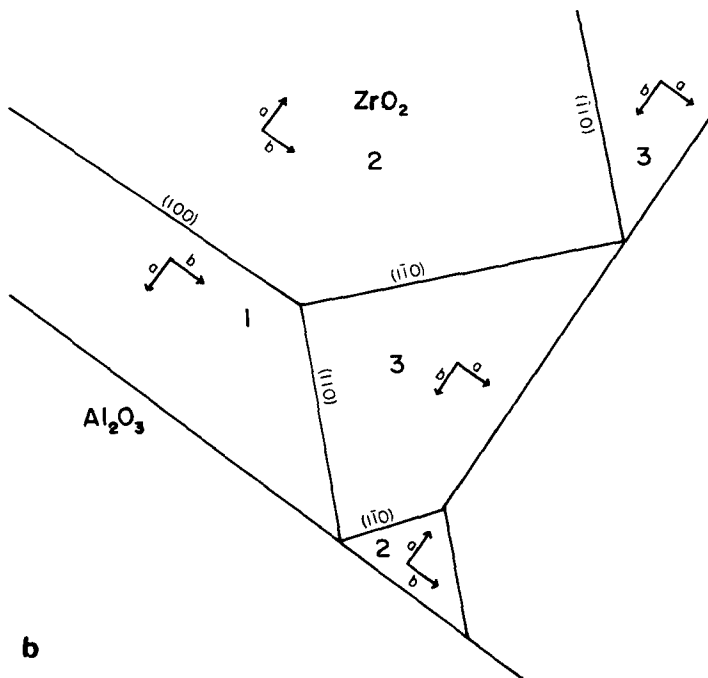
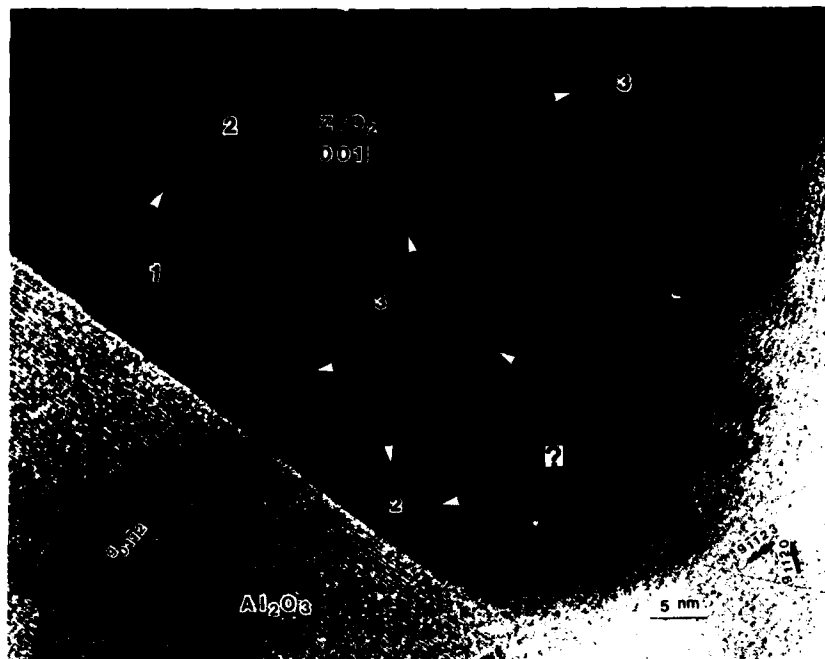


Fig. 8. (a) High-resolution image of intergranular  $\text{ZrO}_2$  particle showing microtwins. The twin boundaries are arrowed, as is an  $\text{Al}_2\text{O}_3/\text{Al}_2\text{O}_3$  grain boundary. 1, 2, and 3 refer to specific twin orientations shown in (b); the question-mark is a region of serious overlap between the  $\text{ZrO}_2$  and  $\text{Al}_2\text{O}_3$ . (b) Diagram of (a) showing twin planes and orientations.



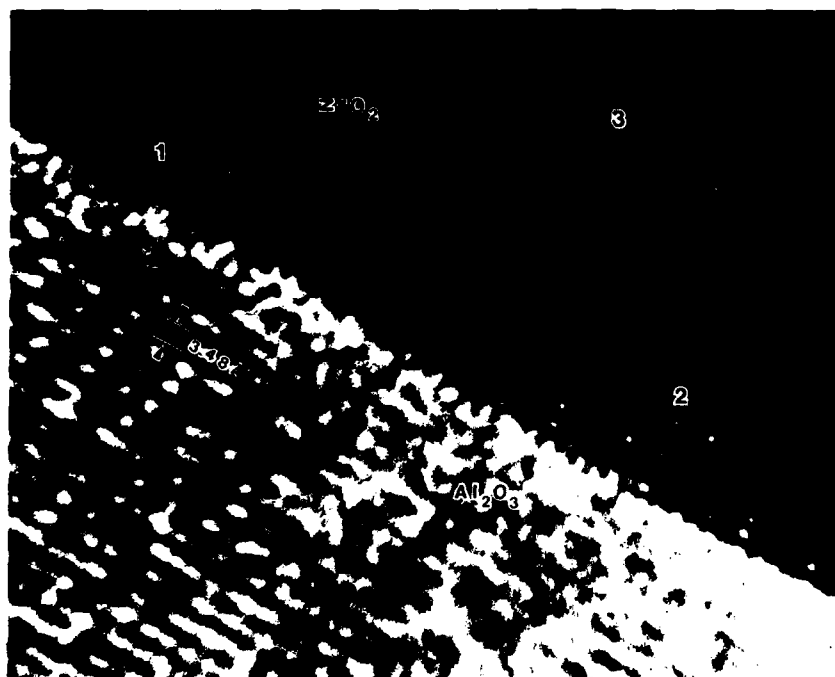


Fig. 9. High-resolution image of  $\text{ZrO}_2$  particle in fig. 8a showing possible glassy phase at grain boundary. 1, 2, and 3 refer to the twin orientations shown in fig. 8b.

grams from fig. 8a, and yielded the results shown schematically in fig. 8b. The morphology of the twinned domains, as well as the existence of  $(100)_m$ ,  $(110)_m$ , and  $(\bar{1}\bar{1}0)_m$  twin boundaries, are identical to the results described by Van Tendeloo et al. in  $\text{ZrO}_2\text{-ZrN}$  alloys [9].

The final figure for this section (fig. 9) shows the  $\text{Al}_2\text{O}_3\text{-ZrO}_2$  interface at high magnification. It is tempting to argue that the broad bright region between the  $\text{Al}_2\text{O}_3$  and  $\text{ZrO}_2$  is a manifestation of the amorphous phase believed to be present, but image simulation is clearly needed to resolve this point. Even lacking such image simulation, it is again remarkable that the features in the structure image extend virtually undisturbed to the incoherent interphase interface. (It is fortunate that the interface in this region of foil is essentially parallel to the electron beam.)

#### 4. $\text{ZrO}_2\text{-Y}_2\text{O}_3$ alloys

$\text{ZrO}_2\text{-Y}_2\text{O}_3$  alloys represent a second major class of  $\text{ZrO}_2$ -containing ceramics which have also been subject to significant commercial exploitation. Low  $\text{Y}_2\text{O}_3$ -content (2–4 mol%) compositions in this system are in use as strong and tough wear-resistant ceramics [10]; medium  $\text{Y}_2\text{O}_3$ -content (4–8 mol%) compositions find use as oxygen sensors in automotive application [11]; and single crystals containing ~10 mol%  $\text{Y}_2\text{O}_3$  are used as imitation diamonds [12]. We have been studying phase equilibria at temperatures between 1300 and 1600°C in this system using a range of compositions between 3 and 9 mol%  $\text{Y}_2\text{O}_3$ . Our strategy is to anneal various compositions for long times to allow the pro-eutectoid precipitation reaction to go to completion and to use analytical electron mi-

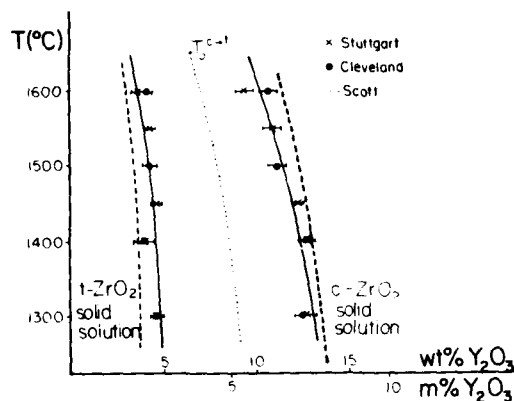
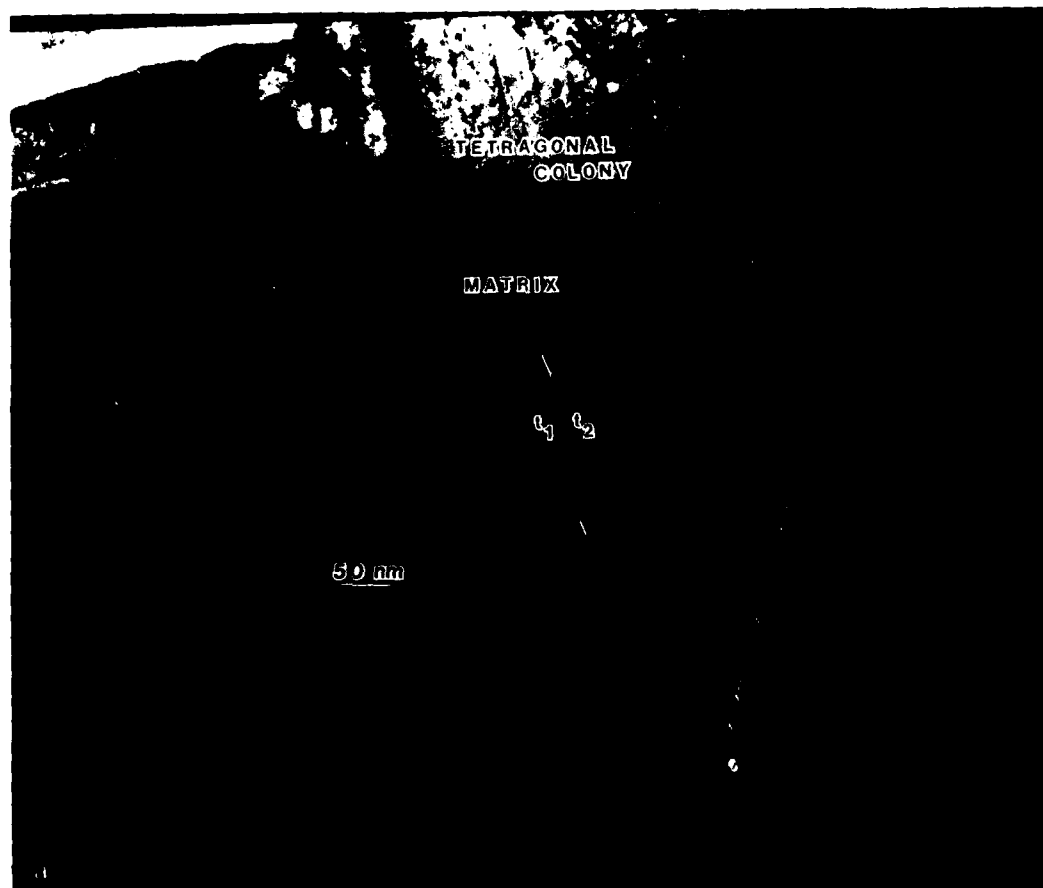


Fig. 10.  $\text{ZrO}_2$ -rich portion of the equilibrium phase diagram in the  $\text{ZrO}_2$ - $\text{Y}_2\text{O}_3$  system. The equilibrium compositions were determined by EDS methods.

croscopy to study the compositions of the coexisting  $c$  and  $t$  solid solutions ( $\text{Y}_2\text{O}_3$  is very potent in stabilizing  $t\text{-ZrO}_2$  and reducing  $M_c$  well below room temperature) [3]. The results of these AEM studies are shown in the partial phase diagram in fig. 10 [3]. For most compositions in the two-phase  $t + c$  solid solution phase field, the  $t\text{-ZrO}_2$  occurs as twinned "colonies", whose structure will be discussed in the remainder of this paper. The colony structure is shown in fig. 11a; this micrograph is taken from a 4 mol%  $\text{Y}_2\text{O}_3$   $\text{ZrO}_2$  single crystal oriented to an exact  $\langle 111 \rangle$  matrix zone-axis orientation. Each colony contains two  $t$  variants, which are actually  $90^{\circ}$  twins (fig. 11b); this morphology occurs to minimize strain between the colony precipitates and the matrix. As will be discussed next, the matrix also has tetragonal sym-



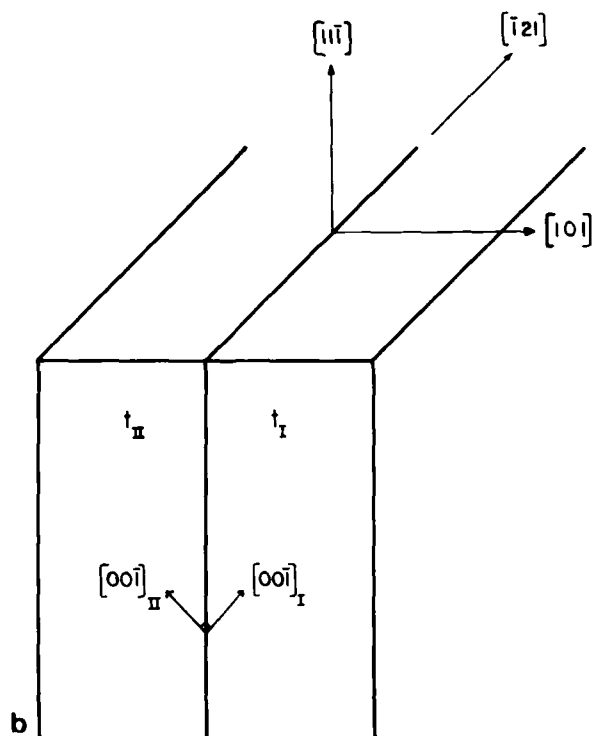


Fig. 11. (a) Tetragonal colony structure in  $\text{ZrO}_2$ -4 mol%  $\text{Y}_2\text{O}_3$  showing a typical interface of interest (arrowed). (b) Schematic diagram showing twin variant crystallography. (The interface is perpendicular to  $[101]$ .)

metry, having undergone a diffusionless  $c \rightarrow t$  transformation on cooling from the annealing temperature [3]. The twinned colony structure of the  $t$ - $\text{ZrO}_2$  precipitates is very stable even during extended annealing; the number of twins per colony remains constant even as the colonies coarsen [13].

A HREM image of a twin variant interface is shown in fig. 12; this interface is similar to the one arrowed in fig. 11a, but of course was taken in a thinner region of the foil. It can be seen that the  $(1\bar{1}0)$  planes are imaged in one  $t$  variant, while the  $(2\bar{2}0)$  planes are imaged in its twin. This difference is believed to result from the very small tilt of one twin relative to the other, and would not occur were the  $c/a$  ratio exactly unity.

The origin of the colony stability is also apparent from fig. 12. The twin interface of fig. 12 (marked TB) can hardly be discerned; were it not for the slight tilt of the two twins, the twin

boundary might not be visible. The good atomic matching thus implied assures that the twin boundary energy is correspondingly low. Thus, interface energy in the twinned structure must always be less than the reduced strain energy between colony precipitate and matrix.

The HREM study has also helped resolve a question concerning the matrix crystallography. As first suggested by Scott [14], and as is discussed elsewhere [3,13,15],  $c$ - $\text{ZrO}_2$  alloys quenched from high temperature can undergo a displacive  $c \rightarrow t$  transformation below a certain critical temperature,  $T_0$ . (The variation in  $T_0$  with composition is indicated by the dashed line in fig. 10 marked  $T_0^{c \rightarrow t}$ .) The equilibrium composition of the  $c$ - $\text{ZrO}_2$  matrix annealed at  $1600^\circ\text{C}$  is 6.0 mol%  $\text{Y}_2\text{O}_3$ ;  $T_0$  for this composition is  $\sim 900^\circ\text{C}$ . We thus expect both the matrix and the colonies of fig. 11 to have  $t$  symmetry, but to differ in  $\text{Y}_2\text{O}_3$  content by a

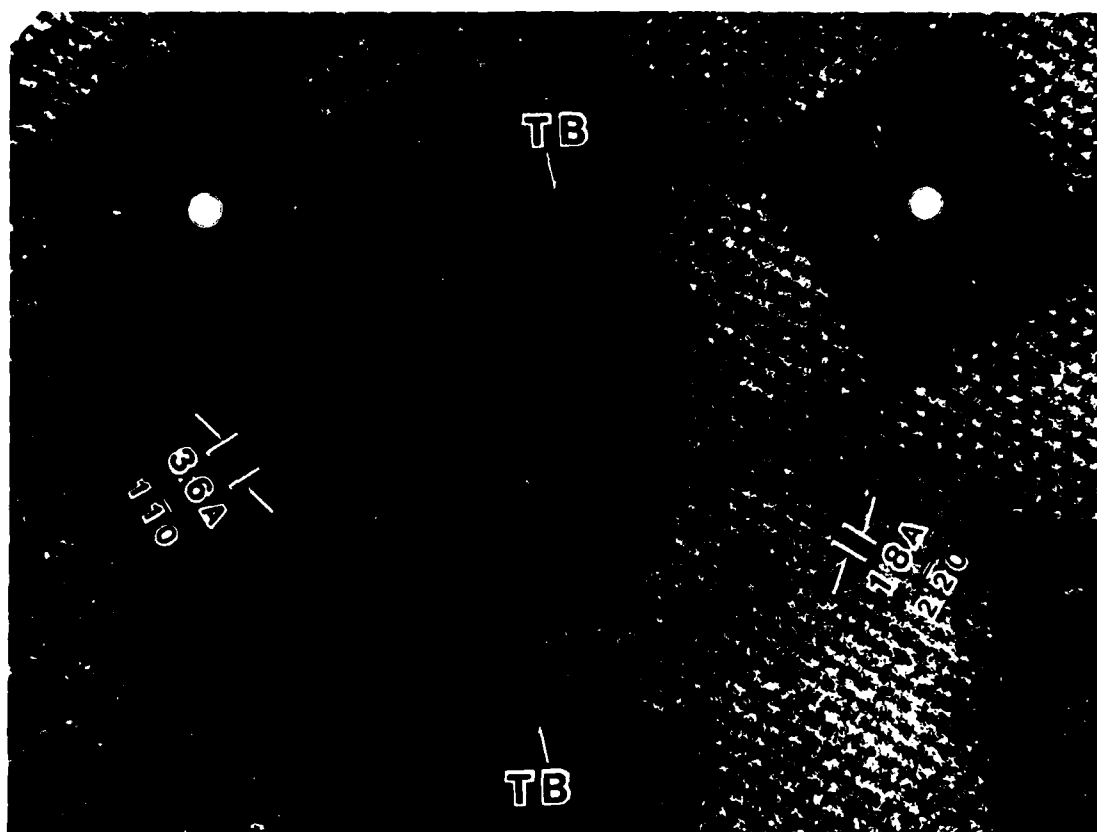


Fig. 12. High-resolution image of a coherent twin boundary (TB) between two tetragonal variants within the same colony. Optical diffractograms are shown as inserts.

factor of  $\sim 3$ . This chemical difference has been confirmed by AEM [13]. However, the variation in lattice parameter with  $\text{Y}_2\text{O}_3$  solute is too small in this system to give rise to any spot splitting in the *odd, odd, even* reflections unique to *t*- $\text{ZrO}_2$  in conventional large-area SAD patterns, and it is difficult to be certain that there is no contribution from the colonies in any SAD pattern taken only from the matrix.

Fig. 13 shows a high-resolution image of the matrix, along with two optical diffractograms taken from different regions of the image. The  $\{220\}$

planes with 0.18 nm spacing imaged on the left portion of fig. 13 are consistent with either *c* or *t* symmetry. Slight bending of the foil has caused the adjacent area to be slightly off the exact orientation. In this region, (110) planes with 0.36 nm spacing are being imaged. (110) is a forbidden reflection for both *c*- $\text{ZrO}_2$  and *t*- $\text{ZrO}_2$ , but often occurs in *t*- $\text{ZrO}_2$  by double diffraction from (112) planes. In any event, this spacing in the optical diffraction pattern is unambiguous evidence that the matrix has undergone the *c*  $\rightarrow$  *t* transformation.

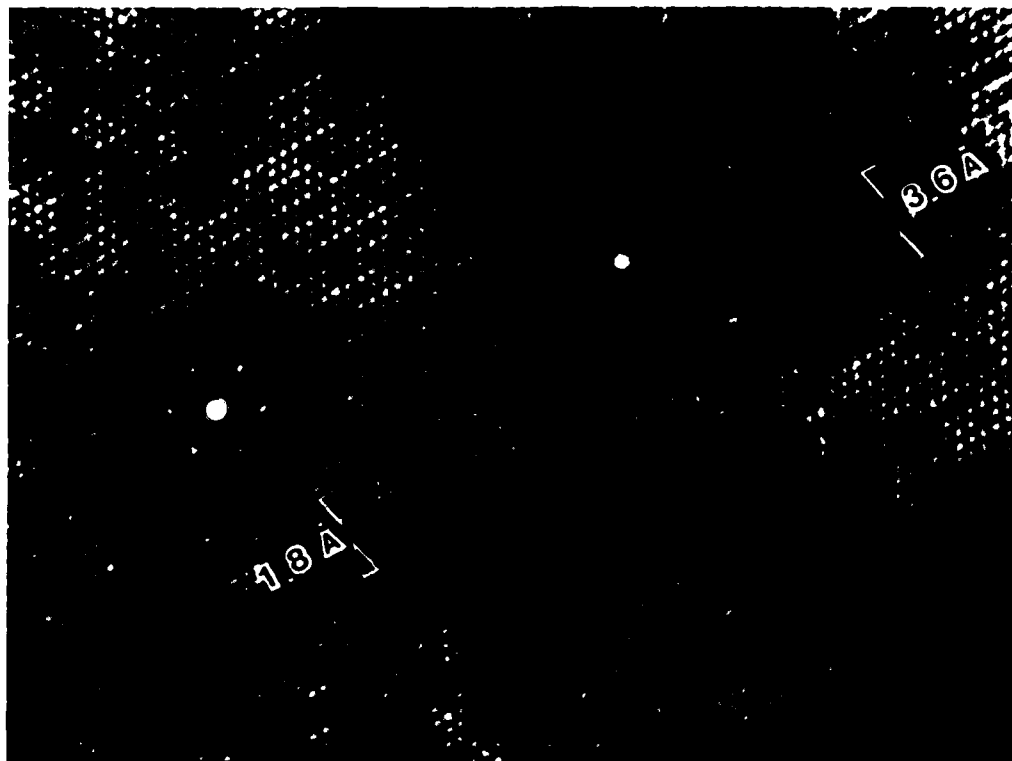


Fig. 13. High-resolution image and optical diffractograms of the matrix between two colonies.

### Acknowledgments

This research was supported by the Air Force Office of Scientific Research, Grant No. AFOSR-82-0227. We also gratefully acknowledge the National Science Foundation who provided the funds to establish our HREM facility.

### References

- [1] A.H. Heuer and L.W. Hobbs, Eds., *Science and Technology of Zirconia*, Advances in Ceramics, Vol. 3 (American Ceramic Society, Columbus, OH, 1981).
- [2] N. Claussen, M. Rühle and A.H. Heuer, Eds., *Science and Technology of Zirconia II*, Advances in Ceramics, Vol. 12 (American Ceramic Society, Columbus, OH, 1984).
- [3] A.H. Heuer and M. Rühle, ref. [2], p. 1.
- [4] A.J. Skarnulis, *J. Appl. Cryst.* 12 (1979) 636.
- [5] A.H. Heuer, N. Claussen, M.W. Kriven and M. Rühle, *J. Am. Ceram. Soc.* 65 (1982) 642.
- [6] A.H. Heuer and M. Rühle, *Acta Met.*, in press.
- [7] S. Schmauder, W. Mader and M. Rühle, ref. [2], p. 126.
- [8] B.W. Kibbel and A.H. Heuer, ref. [2], p. 260.
- [9] G. Van Tendeloo, L. Anders and G. Thomas, *Acta Met.* 31 (1983) 1619.
- [10] M. Rühle, N. Claussen and A.H. Heuer, ref. [2], p. 360.
- [11] E.M. Logothetis, ref. [1], p. 388.
- [12] E.C. Subbarao, ref. [1], p. 1.
- [13] V. Lanteri, T.E. Mitchell and A.H. Heuer, ref. [2], p. 187.
- [14] H.G. Scott, *J. Mater. Sci.* 10 (1975) 1527.
- [15] R. Chaim, M. Rühle and A.H. Heuer, *J. Am. Ceram. Soc.* 68 (1985) 427.

## HREM STUDIES OF INTERFACES IN $\text{ZrO}_2/\text{Al}_2\text{O}_3$ CERAMICS

S. Kraus

Case Western Reserve University, Department of Metallurgy  
Cleveland, Ohio 44106

Because of its unusual mechanical and electrolytic properties, zirconia ( $\text{ZrO}_2$ ) finds a wide variety of uses, such as refractories, oxygen sensors, heaters and extrusion dies.<sup>1,2</sup>  $\text{ZrO}_2$  exists in three polymorphic forms; the high temperature phase is cubic and is isostructural with  $\text{CaF}_2$  (fluorite); below 2350°C (in pure  $\text{ZrO}_2$ ), a tetragonally-distorted version of the fluorite structure exists. At still lower temperature, the tetragonal form ( $t\text{-ZrO}_2$ ) transforms martensitically to a monoclinic structure ( $m\text{-ZrO}_2$ ). This  $t \rightarrow m$  transformation gives rise to the phenomenon of transformation toughening in  $\text{ZrO}_2$ -containing ceramics, and thus provides ceramics with potential for high technology structural applications.

$\text{ZrO}_2$ -toughened  $\text{Al}_2\text{O}_3$  (ZTA) is an example of a wide class of dispersion-toughened ceramics. These materials typically contain 15 vol.%  $\text{ZrO}_2$  in a fine-grained  $\text{Al}_2\text{O}_3$  matrix; the  $\text{ZrO}_2$  is dispersed as both intra- and intergranular particles, and can have monoclinic or tetragonal symmetry. The propensity for undergoing the martensitic transformation depends markedly on the morphology of the  $\text{ZrO}_2$  particles, and nucleation of transformation invariably occurs at the interface between  $\text{ZrO}_2$  and  $\text{Al}_2\text{O}_3$ . Since HREM can contribute vital information in helping to understand these interfaces, a variety of  $\text{ZrO}_2$ -containing ceramics are being investigated on a JEOL 200CX high resolution microscope with a point resolution of 2.4 Å. This paper reports data obtained from a 15vol.% ZTA ceramic, sintered at 1600°C for four hours.

Since the  $\text{ZrO}_2$  particles are randomly oriented, it was a fortunate circumstance to find a roughly spherical, intragranular particle, such that both particle and matrix were oriented within a few degrees of a low index zone; [001] for  $\text{ZrO}_2$  and [0001] for  $\text{Al}_2\text{O}_3$ . A high resolution image of the  $\text{ZrO}_2$  particle tilted exactly to the [001] zone is shown in Fig. 1; the calculated image is inset. The particle has monoclinic symmetry, but is believed to have transformed during thin foil preparation. A high resolution image of the particle-matrix interface can be seen in Fig. 2; where the  $\text{Al}_2\text{O}_3$  grain is tilted to the exact [0001] orientation. The feature marked F is a fault in the  $m\text{-ZrO}_2$ . Fig. 3 shows a higher magnification of the interface structure with the  $\text{ZrO}_2$  exactly on zone. In this region, the interface is nearly parallel to the electron beam, and sensible image interpretation should be possible. (Calculated images are presently being produced using several interface models.) Interface images with the  $\text{Al}_2\text{O}_3$  grain oriented on zone have also been obtained.

A high resolution image of a twinned, intergranular  $m\text{-ZrO}_2$  particle is shown in Fig. 4A. The twinning occurs on transformation during cooling after fabrication, and minimizes the shape strain of the particle resulting from the martensitic transformation. Optical diffractograms of twins permitted determination of the twinned structure, which is shown schematically in Fig. 4B. Our results agree exactly with the findings of Van Tendeloo, et al. in  $\text{ZrO}_2\text{-ZrN}$  alloys.<sup>5</sup> It is believed that a thin (1-3 nm) glassy phase exists at the  $\text{ZrO}_2$  particle- $\text{Al}_2\text{O}_3$  matrix interface (Fig. 5). However, image simulation is again needed to correctly interpret the interface structure and determine whether or not an amorphous phase is actually present. It is tempting, however, to suggest that the bright broad region at the interface is the amorphous phase.<sup>6</sup>

# REFERENCES

1. A.H. Heuer and L.W. Hobbs, Edts, Science and Technology of Zirconia, Adv. in Ceramics, Vol. 3 (The American Ceramic Society, Columbus 1981).
2. N. Claussen, M. Ruhle and A.H. Heuer, Edts, Science and Technology of Zirconia II, Adv. in Ceramics, Vol. 12 (The American Ceramic Society, Columbus 1985).
3. A.H. Heuer, et al., J. Amer. Ceram. Soc., 65 (1982) 642.
4. A.H. Heuer and M. Ruhle, submitted to Acta Met.
5. G. Van Tendeloo, et al., Acta Met., 31 (1983) 1619.
6. This work is supported by the Air Force Grant No. AFSOR-82-0227. I thank my advisors A.H. Heuer and T.E. Mitchell for their guidance and P. Labun for her patience and support.

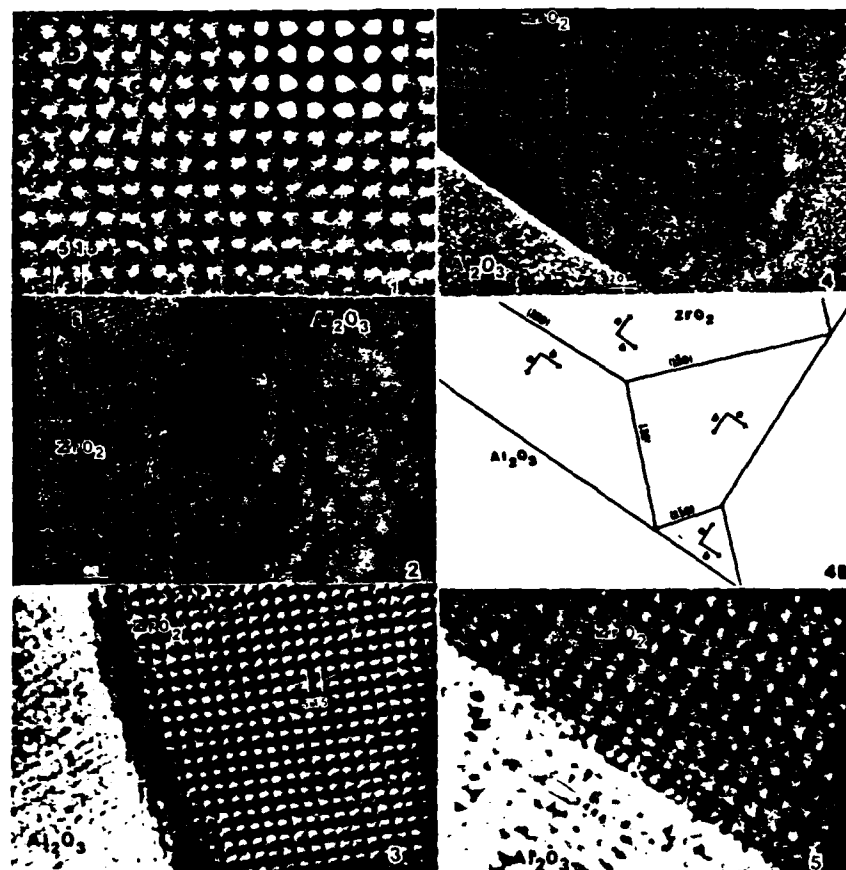


Fig. 1--High resolution image of [001]  $ZrO_2$ , with calculated image match. Unit cell is shown.  
 Fig. 2--High resolution image of  $ZrO_2$ - $Al_2O_3$  interface.  $Al_2O_3$  is on [0001] zone, and F is fault in particle.  
 Fig. 3--Higher magnification of interface structure. Interface is nearly parallel to electron beam.  
 Fig. 4--(A)High resolution image of intergranular  $ZrO_2$  particle showing microtwins. (B)Diagram showing twin planes and orientations.  
 Fig. 5--High magnification image of  $ZrO_2$  particle in Fig. 4A showing possible glassy phase at grain boundary.

## Tetragonal Phase in the System $\text{ZrO}_2\text{-Y}_2\text{O}_3$

V. LANTERI, A. H. HEUER, AND T. E. MITCHELL

Case Western Reserve University  
Department of Metallurgy and Materials Science  
Case Institute of Technology  
Cleveland, OH 44106

Analytical electron microscopy has been used to obtain information on tetragonal ( $t$ )  $\text{ZrO}_2$  in the system  $\text{ZrO}_2\text{-Y}_2\text{O}_3$ . Evidence of two tetragonal solid solutions ( $t$  and  $t'$ ) has been found in single crystals obtained from skull melting. Of the two,  $t'$ - $\text{ZrO}_2$  has the higher  $\text{Y}_2\text{O}_3$  content and has been described by previous workers as "nontransformable"; it is present in as-grown crystals but is metastable. After annealing at high temperatures (1600°C),  $t'$ - $\text{ZrO}_2$  decomposes into a mixture of the two equilibrium phases: a low- $\text{Y}_2\text{O}_3$ -content  $t$ - $\text{ZrO}_2$  and a high- $\text{Y}_2\text{O}_3$ -content cubic ( $c$ ) phase,  $c$ - $\text{ZrO}_2$ . The  $t$ - $\text{ZrO}_2$  appears as precipitate colonies consisting of two twin-related variants in contact along the coherent  $\{101\}$  twin plane.

Precipitates of the high- $\text{ZrO}_2$  tetragonal distorted-fluorite phase in the system  $\text{ZrO}_2\text{-Y}_2\text{O}_3$  appear to be quite different from those observed in other well-studied partially stabilized zirconias (Mg-PSZ, Ca-PSZ).<sup>1-3</sup> In this paper, we discuss the nature of the tetragonal phase in  $\text{Y}_2\text{O}_3$  partially stabilized zirconia (Y-PSZ) single crystals. We note that three versions<sup>4-6</sup> of the phase diagram exist, which differ in detail mainly at the high- $\text{ZrO}_2$  region; our work thus also sheds light on the subsolidus phase equilibria in this system.

Scott<sup>4</sup> described a metastable "nontransformable" high- $\text{Y}_2\text{O}_3$ -content tetragonal  $\text{ZrO}_2$  solid solution ( $t$ - $\text{ZrO}_2$ ), which he and other workers<sup>7,8</sup> suggested formed from the cubic  $\text{ZrO}_2$  solid solution ( $c$ - $\text{ZrO}_2$ ) via a displacive phase transformation; the nontransformability relates to its reluctance to undergo the stress-assisted martensitic transformation to monoclinic symmetry found in lower- $\text{Y}_2\text{O}_3$ -content  $t$ - $\text{ZrO}_2$  (Fig. 1). This form of nontransformable  $t'$ - $\text{ZrO}_2$  is widely encountered in plasma-sprayed Y-PSZ<sup>7-9</sup> and may form only in nonequilibrium situations, as suggested by Scott. For example,  $t'$ - $\text{ZrO}_2$  was not found by Stubican et al.,<sup>5</sup> who used reactive gels and powders in the experiments that led to their construction of the phase diagram for this system.

Virtually all prior studies of this nontransformable  $t$ - $\text{ZrO}_2$  have utilized X-ray studies of powders. One of the goals of this study has been the electron microscopy examination of this form of  $\text{ZrO}_2$  in single crystals. According to Miller et al.,<sup>7</sup> the nontransformable  $t'$ - $\text{ZrO}_2$  formed in plasma-sprayed Y-PSZ is unstable; if these materials are annealed in the two-phase ( $t$ - $\text{ZrO}_2$  +  $c$ - $\text{ZrO}_2$ ) phase field,  $t$ - $\text{ZrO}_2$  forms via a diffusion-controlled precipitation reaction and may subsequently transform martensitically to monoclinic symmetry on cooling.

Attention has been given in this work to a single composition (8 wt%  $\text{Y}_2\text{O}_3$ ) in the two-phase field, which should be single phase with cubic symmetry at high temperatures but which, according to the experiments of Miller et al.,<sup>7</sup> should transform to  $t'$ - $\text{ZrO}_2$  on cooling from high temperature. The stability of  $t'$ - $\text{ZrO}_2$



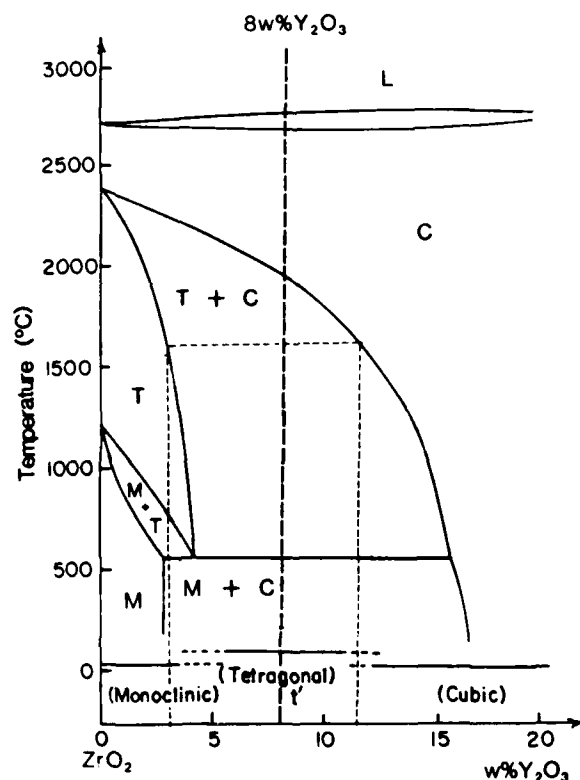


Fig. 1. Phase diagram of the  $\text{ZrO}_2$ -rich region of the system  $\text{ZrO}_2$ - $\text{Y}_2\text{O}_3$  (Ref. 4).

has been investigated with respect to annealing at high temperatures (1600°C), and the phases present after this heat treatment have been characterized.

#### Experimental Procedure

As mentioned above, the single-crystal sample used contained 8 wt%  $\text{Y}_2\text{O}_3$  and was grown by skull melting.\* The crystals were opaque and white, a physical appearance characteristic of nonreduced zirconia. For X-ray diffraction, the sample was crushed into fine powder in an agate mortar. Plates (1 by 10 by 10 mm) were annealed in air at 1600°C for 24, 50, and 100 h and quenched by removal from the furnace. The microstructure of the as-received and annealed specimens was characterized by analytical electron microscopy using a Philips EM400T microscope with standard dark-field techniques, supplemented by energy dispersive X-ray analysis (EDX).

Before proceeding to the results, it is appropriate to describe the techniques used to form dark-field images of  $t$ - $\text{ZrO}_2$ . To distinguish this phase from  $c$ - $\text{ZrO}_2$ ,

\*This crystal was furnished by NRL and manufactured by CERES Corp., Waltham, MA. For further information, see Ref. 10.

only certain foil orientations can be used, where reflections that are unique to the  $t$  phase are present. When transformation from  $c$  to  $t$  symmetry occurs in this system, whether by precipitation or via a displacive phase transformation, three  $t$  variants result, the  $t$   $c$  axis being parallel to any of the three original  $\langle 100 \rangle_c$  directions. To image all the  $t$  variants, the most convenient foil orientation is  $\langle 111 \rangle$ . Also,  $t$ -ZrO<sub>2</sub> can be described in terms of either a nonprimitive base-centered unit cell, which in fact is a slightly distorted version of the  $c$  fluorite unit cell, or a conventional primitive  $t$  unit cell.<sup>11,12</sup> For convenience in this paper, the former C-centered  $t$  cell will be used for comparison with the fluorite cell of  $c$ -ZrO<sub>2</sub>.

### Results

Figure 2 is a typical  $[\bar{1}11]$  diffraction pattern of the as-received material. The most intense ("fundamental") reflections are those allowed by both  $c$ - and  $t$ -ZrO<sub>2</sub>, whereas the weaker reflections are due to the  $t$  phase and have the subscript  $t$ . For all  $\{1\bar{1}2\}_t$ -type reflections to be present in a  $[\bar{1}11]$  zone axis selected-area diffraction (SAD) pattern, three  $t$  variants must be present in the area of foil giving rise to the SAD, each variant giving rise to one  $\{1\bar{1}2\}_t$  reflection.<sup>13</sup> It is thus possible to image all the  $t$  variants in the dark field using the three  $\{1\bar{1}2\}_t$  reflections (see below). X-ray diffraction performed on the as-received specimen showed that only a very small amount of  $c$ -ZrO<sub>2</sub> was present, indicating that the material contains almost 100%  $t$ -ZrO<sub>2</sub>.

Figure 3 shows dark-field micrographs of the as-received material using the three  $\{1\bar{1}2\}_t$  reflections just described. The  $t$ -ZrO<sub>2</sub> particles imaged in Fig. 3(a) appear to be precipitates  $\approx 10$  nm thick by  $\approx 50$  nm long, lying on two  $\{101\}$  habit planes. The  $t$ -ZrO<sub>2</sub> precipitates in Y-PSZ thus appear to be different from  $t$ -ZrO<sub>2</sub>.

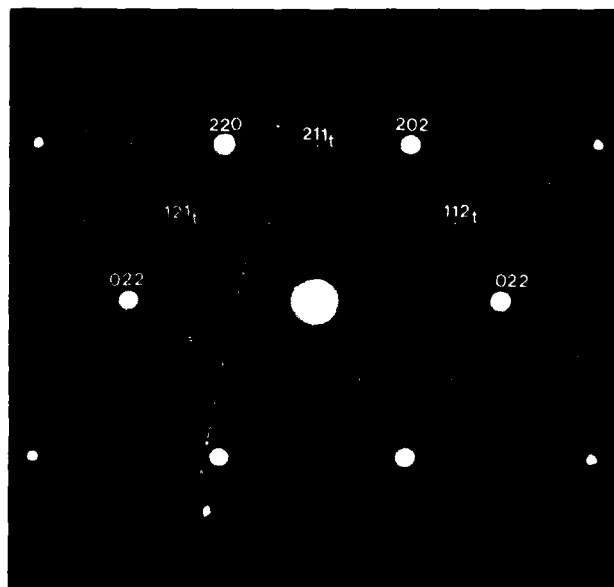


Fig. 2. Diffraction pattern,  $[\bar{1}11]$  zone axis.

precipitates in Mg-PSZ, where the precipitate/matrix habit plane is invariably  $\{100\}$ , and Ca-PSZ, where the precipitates tend to be equiaxed. Figure 3(b) is obtained by using a second  $\{1\bar{1}2\}_t$  reflection in the same area of the foil. A second tetragonal variant is imaged in this case and is also present as well-defined precipitates with a  $\{101\}$  habit plane. The third  $\{1\bar{1}2\}_t$  tetragonal reflection (Fig. 3(c)) gives rise to a different microstructure in the same area of the foil—the “matrix” in which the precipitates of Fig. 3(a) and (b), are contained. If the three micrographs are superimposed, all the foil area has been illuminated; it appears that the entire foil area has  $t$  symmetry, confirming the X-ray analysis.

It thus appears that the single crystal consists of a  $t$  matrix containing  $t$  precipitates! We believe that, during the slow cooling that is part of the skull-melting crystal-growth process, a high-temperature displacive transformation from  $c$  to  $t$  symmetry occurred, giving rise to the  $t'$  matrix structure of Fig. 3(c). The precipitates of Fig. 3(a) and (b) are believed to be low- $Y_2O_3$   $t$ -ZrO<sub>2</sub>, which formed via a conventional diffusion-controlled reaction, either from the  $c$  phase or from the  $t'$ -ZrO<sub>2</sub> itself. The small amount of  $c$ -ZrO<sub>2</sub> indicated by the X-ray analysis was not detectable in the area of foil imaged in Fig. 3. It has been suggested<sup>14,15</sup> that the  $c \rightarrow t'$  displacive reaction should give rise to antiphase domain boundaries (APBs), which have been imaged by TEM by Bender and Lewis<sup>16</sup> in 3 and 6 wt% Y-PSZ single crystals after laser irradiation, by Chaim et al.<sup>15</sup> in a 12 wt% Y-PSZ polycrystal after suitable heat treatment, and by Michel et al.<sup>17</sup> in 5.4 wt% single crystals. The arrowed features in Fig. 3(c) are also thought to be APBs arising from this transformation.

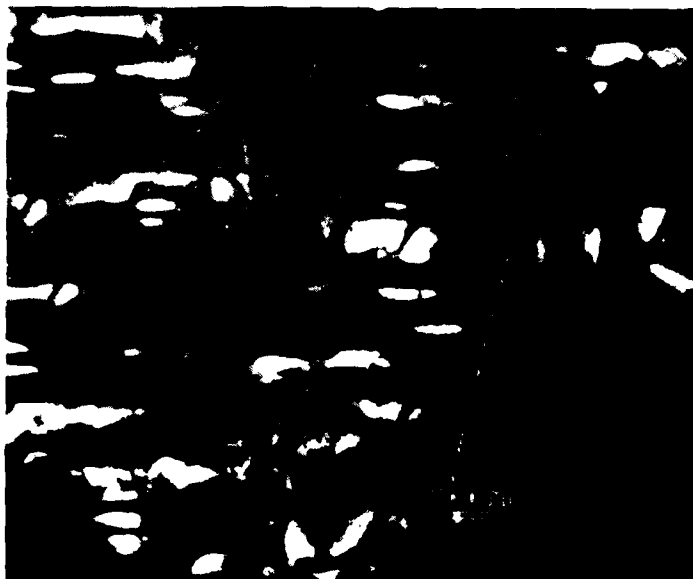
EDX analysis of the matrix of Fig. 3(c) showed a  $Y_2O_3$  content of  $\approx 8$  wt%. If, as has been suggested,  $t$ -ZrO<sub>2</sub> is a precipitate that formed in a  $c$  or  $t'$  matrix, then it should have a lower  $Y_2O_3$  content than the parent  $t'$  matrix (see Fig. 1). Unfortunately, the small size of the  $t$ -ZrO<sub>2</sub> precipitates and the difficulty of distinguishing the precipitates during conventional bright-field imaging prevent confirming this prediction by EDAX analysis. Therefore, we studied further decomposition of the  $t'$  matrix during high-temperature (1600°C) annealing, with the expectation that the precipitates would coarsen.

From the phase diagram (Fig. 1),  $t'$ -ZrO<sub>2</sub> should decompose into a low- $Y_2O_3$   $t$ -ZrO<sub>2</sub> solid solution containing  $\approx 3$  wt%  $Y_2O_3$  plus a  $c$ -ZrO<sub>2</sub> solid solution containing  $\sim 12$  wt%  $Y_2O_3$ . Dark-field micrographs of the same area of a foil, again obtained with the three  $\{1\bar{1}2\}_t$  reflections, are shown in Fig. 4 from a specimen which had been aged 24 h at 1600°C. Figure 4(a) and (b) indicates that the  $t$ -ZrO<sub>2</sub> precipitates have grown at the expense of the  $t'$  matrix, the precipitates occurring in the form of large “colonies”; each colony actually consists of plates of two twin-related variants. The two variants have different  $c$  axes but share a habit plane, which is the coherent twin plane. Small colonies can actually be discerned at the arrowed region of Fig. 3(a); it is clear the colonies coarsen during annealing. The remaining  $t'$ -ZrO<sub>2</sub> is imaged in Fig. 4(c); notice that it is located at the periphery of the colonies and has a  $c$  axis different from that of the two variants constituting the colony. The  $t'$ -ZrO<sub>2</sub> is clearly a minor component, confirming that  $t'$ -ZrO<sub>2</sub> is unstable with respect to diffusion at high temperatures. We thus expect the decomposition products of  $t'$ -ZrO<sub>2</sub> to be a mixture of equilibrium phases, namely,  $c$ -ZrO<sub>2</sub> and the colonies of  $t$ -ZrO<sub>2</sub>. Such a microstructure can be seen in Fig. 5 from a specimen aged for 50 h at 1600°C. Figure 5(a) is a bright-field micrograph and shows coarse colonies set among  $c$  regions. Figure 5(b) is the corresponding dark-field micrograph, taken with a  $t$  reflection.

(a)



(b)



(c)

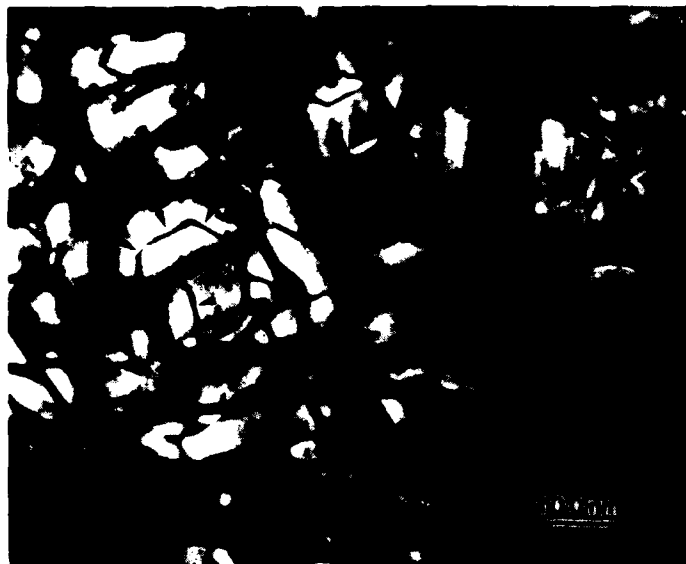


Fig. 3. Dark-field micrographs of as-received single crystal (8 wt%  $\text{Y}_2\text{O}_3$ ). (a)  $\mathbf{g} = \bar{1}1\bar{2}$ , (b)  $\mathbf{g} = 211$ , and (c)  $\mathbf{g} = 12\bar{1}$ .

Microchemical EDX analysis was performed to compare the  $\text{Y}_2\text{O}_3$  content of the colonies and the  $c\text{-ZrO}_2$ . The two spectra are compared in Fig. 6, where it is clear that the  $c$  phase is significantly richer in  $\text{Y}_2\text{O}_3$  than are the  $t$  colonies. Quantification of these data revealed a  $\text{Y}_2\text{O}_3$  content of  $4.1 \pm 0.1$  and  $10.6 \pm 0.1\%$  for the colonies and the  $c\text{-ZrO}_2$ , respectively, close to but not identical with the predictions of Scott's phase diagram (Fig. 1).

The twin relation of variants within the same colony is best illustrated in Fig. 7 from a specimen aged at  $1600^\circ\text{C}$  for 100 h; the same features as in Fig. 5 are present, and the coarsening of the tetragonal colonies has progressed further. The selected-area diffraction pattern from one colony shows that only two variants are present. The third variant, which in fact was the original  $t'\text{-ZrO}_2$  in the starting material, is not contained in this area of foil. By imaging the colony with the two remaining  $\{1\bar{1}2\}$  reflections, reverse contrast is observed, showing that the colony indeed contains two twin-related variants.

#### Discussion

This study has shown evidence of two tetragonal solid solutions,  $t\text{-ZrO}_2$  and  $t'\text{-ZrO}_2$ . These two phases have a quite different microstructure and composition. In the as-received crystal, metastable bulky  $t'\text{-ZrO}_2$  is present, while after annealing, the equilibrium  $t\text{-ZrO}_2$  precipitates are in the form of colonies. The colony orientation appears to be closely related to the original orientation of the  $t'\text{-ZrO}_2$ . Within each colony, there are two twin-related variants, whose respective  $c$  axes

(a)



(b)



(c)



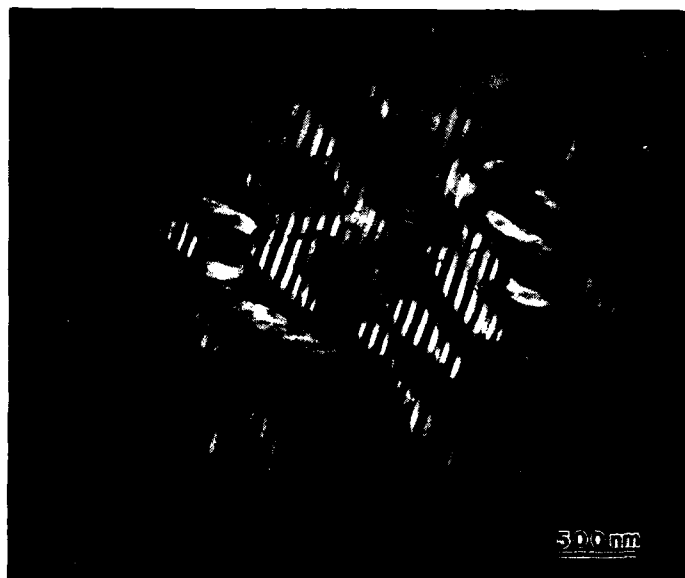
Fig. 4. Dark-field micrographs of specimen aged 24 h at 1600°C: (a)  $g = \bar{1}1\bar{2}$ , (b)  $g = 211$ , and (c)  $g = 12\bar{1}$ .

are along the  $a$  and  $b$  axes of the original  $t'$ -ZrO<sub>2</sub>. These colonies have also been observed in polycrystalline sintered ceramics with the same Y<sub>2</sub>O<sub>3</sub> content<sup>18</sup> and in a 12 wt% Y<sub>2</sub>O<sub>3</sub> polycrystal.<sup>15</sup> (In the former material the tetragonal colonies nucleated and grew in a cubic matrix.) The formation of colonies at the expense of the  $t'$  matrix, and in  $c$ -ZrO<sub>2</sub> grains in a sintered ceramic, and their stability after lengthy annealing suggest that the twin interface within the colonies has an unusually low interfacial energy and that formation of colonies in both  $t'$  and  $c$ -ZrO<sub>2</sub> minimize lattice strain very effectively. In fact, as the habit plane of the colony is perpendicular to the  $a$  axis of  $t'$ -ZrO<sub>2</sub> and of  $c$ -ZrO<sub>2</sub>, the "fit" between the  $t$  colony and its matrix is very similar in both situations.

Earlier workers also pointed out that  $t'$ -ZrO<sub>2</sub> is nontransformable, in the sense that it does not undergo the martensitic transformation to monoclinic symmetry even under stress (e.g., during grinding). However, the  $t$  colonies formed from  $t'$ -ZrO<sub>2</sub> are also quite stable in that no monoclinic phase was found by X-ray diffraction in crushed specimens that had been annealed for 50 h. This is quite different from what has been observed in other partially stabilized zirconias and is not well understood at this time.

Finally, it is interesting to provide a thermodynamic/kinetic rationale for the existence of two  $t$ -ZrO<sub>2</sub> solid solutions in this system. We assume that (i)  $c$ -ZrO<sub>2</sub> does form in 8 wt% materials from the melt, (ii) during cooling following skull melting, the cooling history is such that diffusional decomposition to  $c$ - and  $t$ -ZrO<sub>2</sub>, which should occur at  $T < 2000^\circ\text{C}$  (Fig. 1), does not occur, and (iii) the  $c$ -ZrO<sub>2</sub> undergoes a displacive transformation to tetragonal symmetry at some critical

(a)



(b)

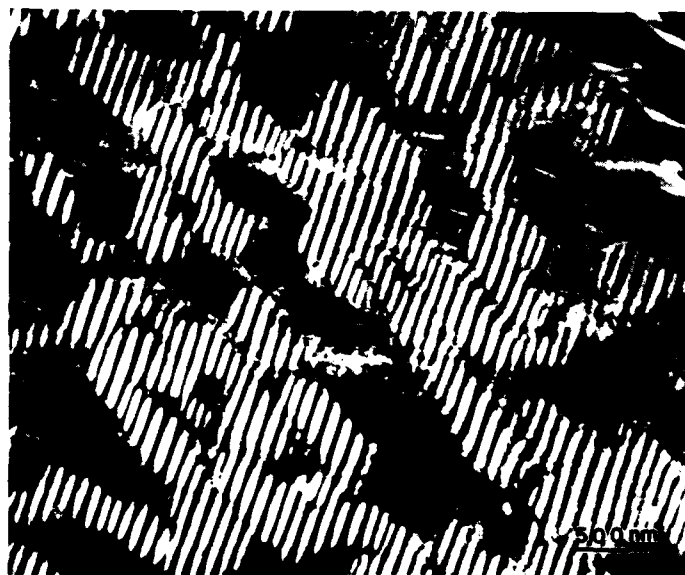


Fig. 5. Micrographs of specimen aged 50 h at 1600°C: (a) bright field and (b) dark field,  $\mathbf{g} = \bar{1}12$ .



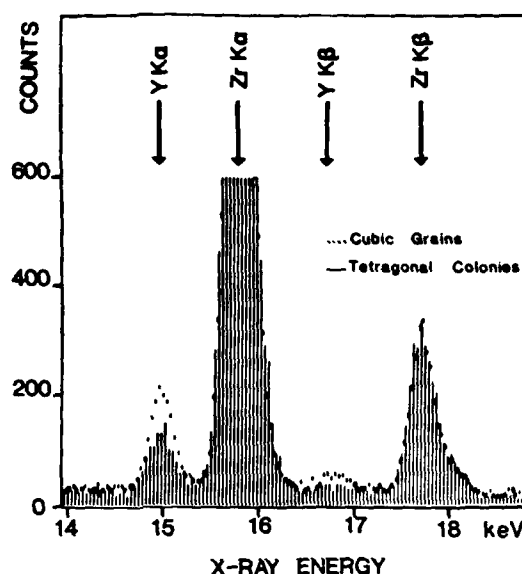


Fig. 6. Energy dispersive X-ray spectra of *c* matrix and *t* colonies.

temperature  $T_0$ . Plausible free energy vs composition curves above and below  $T_0$  are depicted in Fig. 8. Although a two-phase assemblage has the minimum free energy for an 8 wt% material for the situation depicted in Fig. 8(a), supersaturated *c*-ZrO<sub>2</sub> solid solution will persist until *t*-ZrO<sub>2</sub> of the equilibrium composition can be nucleated. If cooling below  $T_0$  without nucleation of *t*-ZrO<sub>2</sub> occurs (Fig. 8(b)), a displacive transformation in an 8 wt% material from supersaturated *c*-ZrO<sub>2</sub> to supersaturated *t'*-ZrO<sub>2</sub> can occur and will lower the free energy from  $G_s$  to  $G_i$  ( $\Delta G'$ ). The solid solution *t'*-ZrO<sub>2</sub> can further lower its energy by forming *t*-ZrO<sub>2</sub> of free energy  $G_t$  and *c*-ZrO<sub>2</sub> of free energy  $G_c$  for a further energy reduction of  $\Delta G''$ , but this will be a sluggish transformation, as considerable diffusion is required.

Further study is under way on the mechanism of the displacive *c*  $\rightarrow$  *t'* transformation and on the variation of  $T_0$  with composition. These experiments should also assist in determining the actual boundaries of the two-phase (*c*-ZrO<sub>2</sub> + *t*-ZrO<sub>2</sub>) field by using EDX microchemical analysis of the equilibrium microstructures (*c*-ZrO<sub>2</sub> and colonies of *t*-ZrO<sub>2</sub>).

#### Acknowledgments

The authors thank the Naval Research Lab in Washington, DC, for providing the single crystals and R. F. Hehemann for informative discussions. This research was supported by AFOSR under Contract 82-0227. A. H. Heuer also acknowledges the Alexander von Humboldt Foundation for a Senior Scientist Award, which made possible his sabbatical leave at the Max-Planck-Institut Für Metallforschung in Stuttgart, Federal Republic of Germany, where this paper was written.

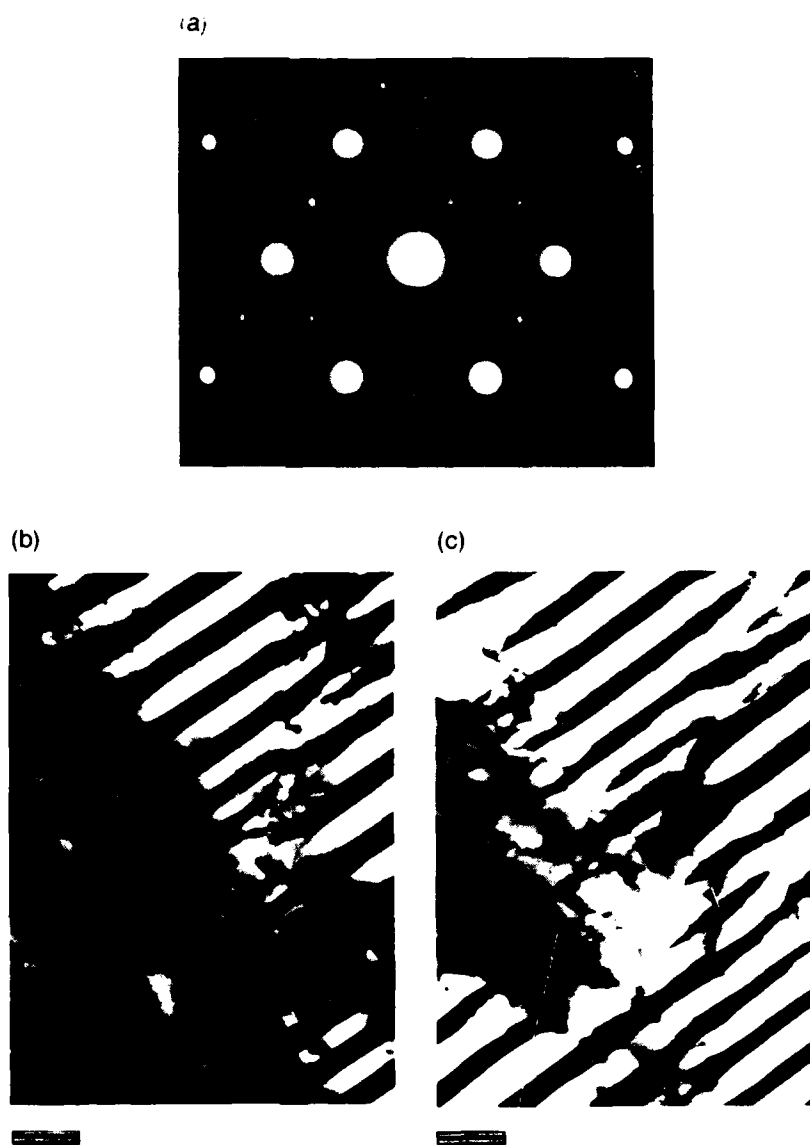


Fig. 7. Specimen aged 100 h at 1600°C: (a) SAD pattern,  $[111]$  zone axis from one colony, (b) dark-field micrograph,  $\mathbf{g} = 11\bar{2}$ , and (c) dark-field micrograph,  $\mathbf{g} = 211$ . The arrows in (b) and (c) point to the same feature. Bar = 500 nm.

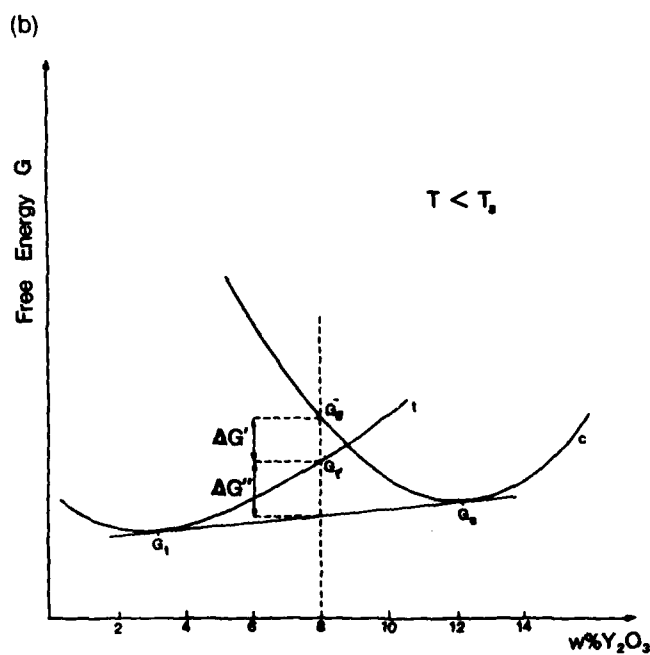
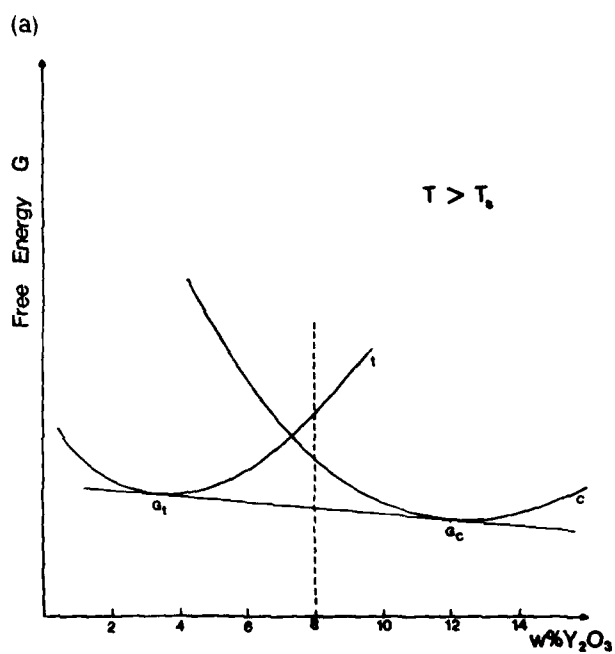


Fig. 8. Free energy vs composition curves: (a) above the critical temperature  $T_c$  and (b) below the critical temperature  $T_c$ .

## References

- <sup>1</sup>R. H. J. Hannink, *J. Mater. Sci.*, **13**, 2487-97 (1978).
- <sup>2</sup>D. L. Porter and A. H. Heuer, *J. Am. Ceram. Soc.*, **62** [5-6] 298-305 (1979).
- <sup>3</sup>J. M. Marder, T. E. Mitchell, and A. H. Heuer, *Acta Metall.*, **31** [3] 387-95 (1983).
- <sup>4</sup>H. J. Scott, *J. Mater. Sci.*, **10** [9] 1527-35 (1975).
- <sup>5</sup>V. S. Stubican, R. C. Hink, and S. P. Ray, *J. Am. Ceram. Soc.*, **61** [1-2] 17-21 (1978).
- <sup>6</sup>C. Pascual and P. Duran, *J. Am. Ceram. Soc.*, **66** [1] 23-27 (1983).
- <sup>7</sup>R. B. Miller, J. L. Smialek, and R. G. Garlick; pp. 241-53 in *Advances in Ceramics*, Vol. 3. Edited by L. W. Hobbs and A. H. Heuer. The American Ceramic Society, Columbus, OH, 1981.
- <sup>8</sup>C. A. Andersson and T. K. Gupta; pp. 184-201 in *Advances in Ceramics*, Vol. 3. Edited by L. W. Hobbs and A. H. Heuer. The American Ceramic Society, Columbus, OH, 1981.
- <sup>9</sup>R. J. Bratton and S. L. Lau; pp. 226-40 in *Advances in Ceramics*, Vol. 3. Edited by L. W. Hobbs and A. H. Heuer. The American Ceramic Society, Columbus, OH, 1981.
- <sup>10</sup>R. P. Ingel; Ph. D. Thesis, The Catholic University of America, Washington, DC (1982).
- <sup>11</sup>G. Teufer, *Acta Crystallogr.*, **15** [11] 1187 (1962).
- <sup>12</sup>J. Lefevre, *Ann. Chim.*, **8**, 117-49 (1963).
- <sup>13</sup>L. H. Schoenlein; Ph. D. Thesis, Case Western Reserve University, Cleveland, OH, 1982.
- <sup>14</sup>A. H. Heuer and M. Rühle; this volume, pp. 1-13.
- <sup>15</sup>R. Chaim, A. H. Heuer, and M. Rühle; unpublished results.
- <sup>16</sup>B. A. Bender and D. Lewis; private communication.
- <sup>17</sup>D. Michel, L. Mazerolles, M. Perex, and Y. Jorba; this volume, pp. 131-38.
- <sup>18</sup>P. G. Valentine; M.S. Thesis, Case Western Reserve University, Cleveland, OH, 1982.

## **HREM of incoherent $\text{ZrO}_2/\text{Al}_2\text{O}_3$ interfaces**

A H Heuer, S P Kraus-Lanteri, P A Labun, and T E Mitchell  
Case Western Reserve University  
Cleveland, Ohio 44106 USA

### Introduction

Dispersion-toughened ceramics have received much attention in recent years due to their impressive mechanical properties. In particular,  $\text{ZrO}_2$  additions to  $\text{Al}_2\text{O}_3$  can increase the strength of the material to greater than 1 GPa (1). Typically, small amounts of  $\text{ZrO}_2$  ( $\leq 30$  vol.%) are dispersed in a fine-grained  $\text{Al}_2\text{O}_3$  matrix; the  $\text{ZrO}_2$  exists as both intragranular and intergranular, incoherent particles with either monoclinic (m) or tetragonal (t) symmetry. The enhanced strength and toughness arise from the phenomenon known as transformation toughening, involving the martensitic t- $\text{ZrO}_2$  to m- $\text{ZrO}_2$  transformation. Nucleation of the transformation invariably occurs at the  $\text{ZrO}_2/\text{Al}_2\text{O}_3$  interface (2).

High resolution electron microscopy contributes vital information in helping to understand these interfaces. In the past, HREM has been performed on materials of known orientation containing coherent or semi-coherent interfaces. In polycrystalline  $\text{ZrO}_2$ -toughened  $\text{Al}_2\text{O}_3$  (ZTA), the  $\text{ZrO}_2/\text{Al}_2\text{O}_3$  interface is not only incoherent but the particle and matrix are of random orientation. In spite of these adverse conditions, HREM is still possible, and yields interesting results.

### Experimental procedure

As-sintered ZTA samples containing 3.8, 10, and 15 vol.%  $\text{ZrO}_2$  were studied using HREM. Thin foils were prepared by conventional ion-milling techniques. After ion-milling, the thin foils received a short heat treatment (15 min. at 1200°C) to reverse any t  $\rightarrow$  m transformation which may have occurred during foil preparation. Samples were examined in a JEOL 200CX transmission electron microscope fitted with a top entry  $\pm 10^\circ$  tilting stage; the microscope has a  $C_s$  of 1.1 mm, and has a point-to-point resolution of 0.236 nm.

### Results and discussion

In order to image the  $\text{ZrO}_2/\text{Al}_2\text{O}_3$  interface successfully, each phase must be exactly on zone, while the interface should be parallel to the electron beam. Due to the random distribution of  $\text{ZrO}_2$  particles, these conditions are difficult to meet; hundreds of particles were investigated, but few were in (or could be tilted to) the proper orientation.

Fig. 1a shows an intragranular, t- $\text{ZrO}_2$  particle from a 10 vol.% sample at low magnification. The  $\text{Al}_2\text{O}_3$  matrix is oriented to the  $[01\bar{1}1]$  zone, while a single set of  $\{111\}$  planes is visible in the  $\text{ZrO}_2$ , as it is about two degrees off its  $\langle 110 \rangle$  zone. The  $\{111\}$   $\text{ZrO}_2$  planes and  $(0\bar{1}11)$   $\text{Al}_2\text{O}_3$  planes are misoriented by about five degrees; furthermore, the d-spacings of these two sets of planes differ significantly, 0.295 nm for  $\{111\}$   $\text{ZrO}_2$  and 0.393 nm for  $(0\bar{1}11)$   $\text{Al}_2\text{O}_3$ . In spite of this apparent

lattice mismatch, no microcracks or other gross distortions appear at the interface in these HREM images.

Quasi-periodic fringes give rise to some unusual contrast around the particle. At higher magnification (Fig. 1b), the periodicity of the fringes is seen to arise from every fourth  $\text{Al}_2\text{O}_3$  plane (arrowed) stopping short at the interface, as compared to the three preceding planes. As the interface orientation changes, the periodicity changes from every fourth to every third  $\text{Al}_2\text{O}_3$  plane. These arrowed planes are analogous to misfit dislocations commonly observed in semicoherent interfaces. As the orientation changes, so does the apparent configuration of misfit dislocations in the interface structure; they do not appear periodic in Fig. 1c, and are widely spaced in Fig. 1d.

At some orientations, the lattice mismatch is accommodated by a series of ledges one atomic plane in height (Fig. 1e). It is remarkable that features familiar from semicoherent interfaces, i.e. misfit dislocations and ledges, are also a feature of incoherent interfaces in the present system. This must arise in this instance, because the lattice mismatch is in fact small: four  $\text{ErO}$  (111) planes have a spacing of 1.180 nm, while three  $\text{Al}_2\text{O}_3$  (011) planes are spaced 1.179 nm.

Near the interface in the  $\text{ErO}$  particle, some structure images including planes with half of the (111) planar spacing can be discerned. It is believed that the strains arising from the thermal expansion mismatch of the two materials have bent the  $\text{ErO}$  lattice into a favorable orientation for imaging the (111) planes. This can be seen most clearly in Fig. 1e.

The majority of the intragranular  $\text{ErO}$  particles in the 10 vol.% material are spherical, but some faceted particles are also present (Fig. 2a). The facetting suggests the existence of a low energy interface between  $\text{Al}_2\text{O}_3$  and  $\text{ErO}$ . The  $\text{Al}_2\text{O}_3$  grain is exactly oriented to the (1010) zone, but the Moiré fringes in the particle unfortunately indicate that the  $\text{ErO}$  overlaps the  $\text{Al}_2\text{O}_3$ . The  $\text{ErO}$  orientation was determined using optical diffractometry, which showed that (200) planes from  $\text{t-ErO}$  were parallel to (1110)  $\text{Al}_2\text{O}_3$  planes. Fig. 1 shows that the basal planes of  $\text{Al}_2\text{O}_3$  are also parallel to the facet. Muercolles, et al. (3) have studied  $\text{Al}_2\text{O}_3$ - $\text{ErO}$  ( $\text{Y}_2\text{O}_3$ ) eutectics and found the following planes of  $\text{t-ErO}$  and  $\text{Al}_2\text{O}_3$  to be parallel:  $\text{t-ErO}$  // (0001), (100) // (1110), (010) // (0110); the corresponding directions were also parallel. For the particular faceted particle in Fig. 2b, (200) is parallel to (1110).

Image simulations using Keefe's SHRII (Simulated High Resolution Lattice Imaging) program (4) are currently being performed with various models to obtain a match with experimental images, and thus determine the interface structure. Our strategy is to first create a sharp interface with the ideal  $\text{ErO}$  and  $\text{Al}_2\text{O}_3$  structures in the observed (random) orientation, and then to relax the atomic positions to best fit the observed images. To date, the perfect lattices of  $\text{Al}_2\text{O}_3$  in the [100] and [110] zones have been successfully simulated.

#### Summary

Incoherent  $\text{ErO}/\text{Al}_2\text{O}_3$  interfaces can be successfully imaged with HREM. Lattice mismatch is accommodated by a combination of misfit dislocations and ledges, analogous to those found in semicoherent precipitates. Low energy orientations also exist between  $\text{ErO}$  and  $\text{Al}_2\text{O}_3$ , as attested to by presence of faceted particles.

#### Acknowledgment

This research was supported by Air Force Grant No. AFOSR-82-1177.

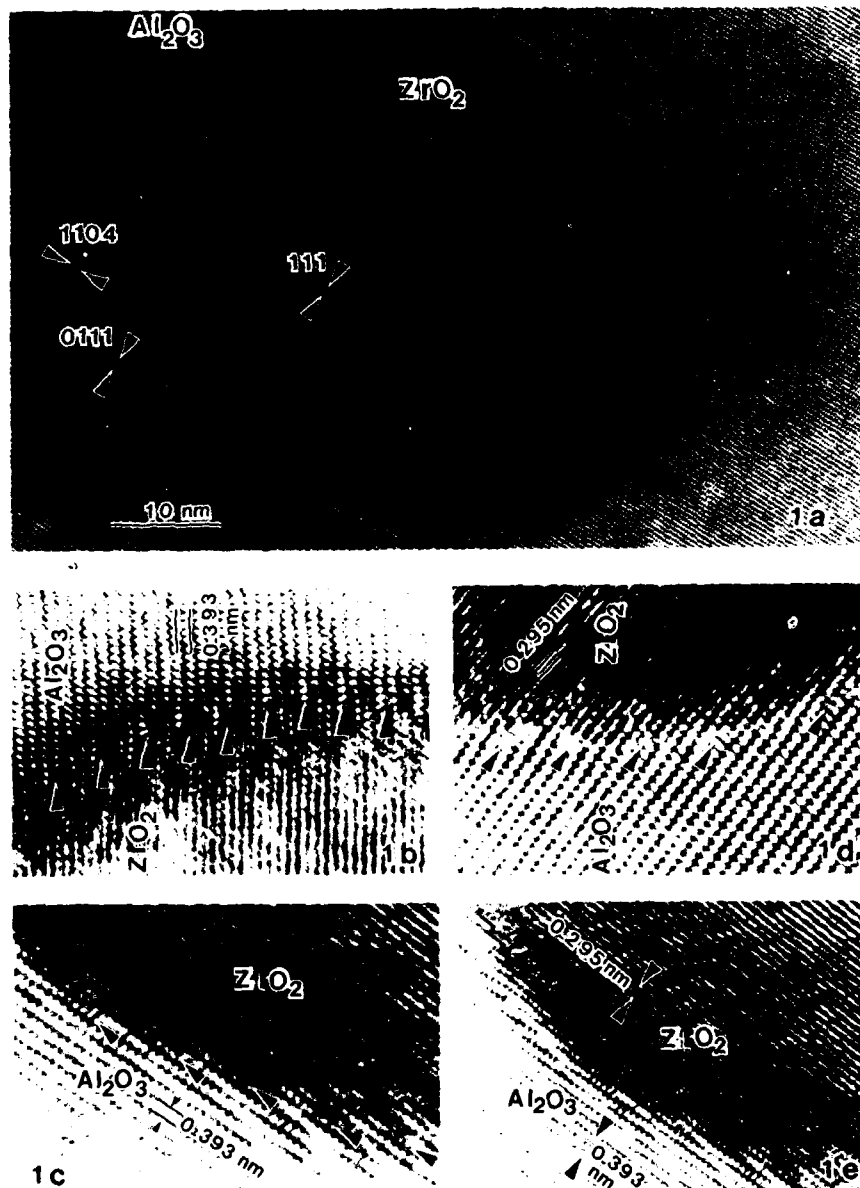


Fig. 1 (a) Intragranular,  $t$ - $\text{ZrO}_2$  particle with higher magnification images of various areas (b-e). See text for details.

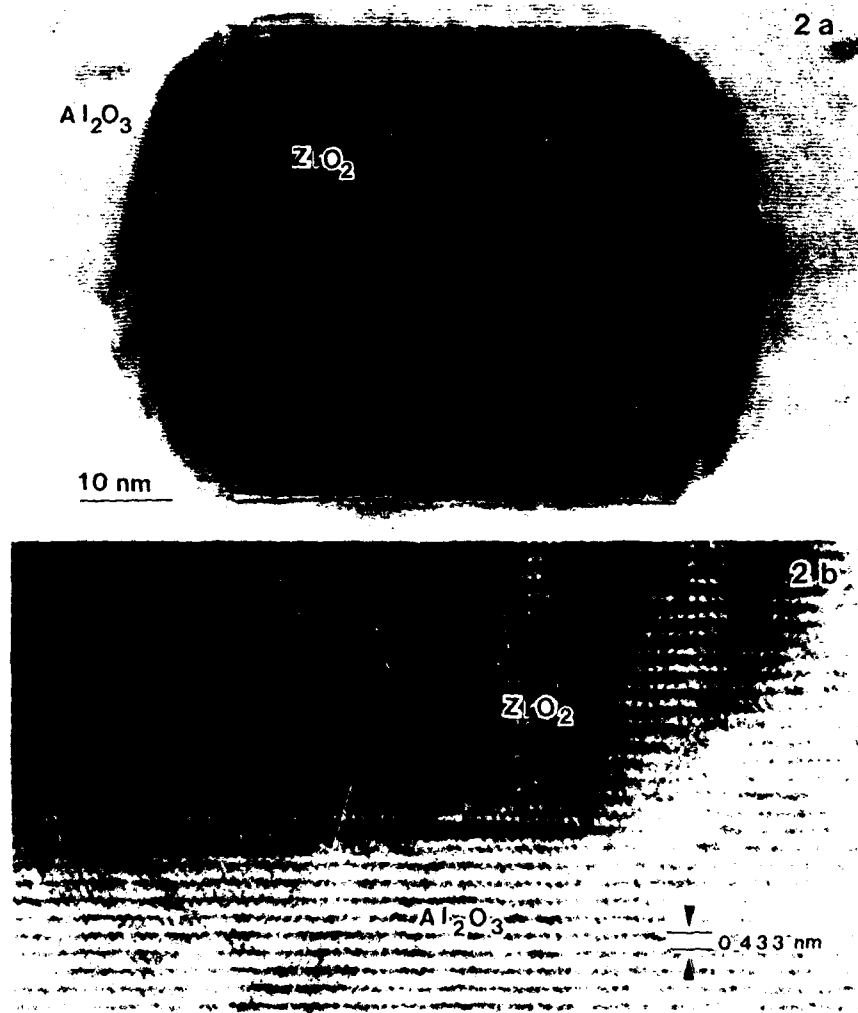


Fig. 2 (a) Intragranular faceted  $t$ - $ZrO_2$  particle. (b) Note  $Al_2O_3$  basal planes parallel to facet.

#### References

1. N. Claussen in *Advances in Ceramics*, Vol. 12, edited by N. Claussen, M. Rühle, and A. H. Heuer, American Ceramic Society (Columbus, Ohio) 1983, p. 325.
2. A. H. Heuer and M. Rühle, in press, *Acta Met.*, 1985.
3. L. Mazerolles, D. Michel, and R. Portier, to be published in *J. Am. Ceram. Soc.*, 1985.
4. M. A. O'Keefe and P. K. Buseck, *Trans. Am. Crystallogr. Assoc.*, 15, 44-46 (1979).



# Structure of Incoherent $\text{ZrO}_2/\text{Al}_2\text{O}_3$ Interfaces

S. P. KRAUS-LANTERI,\* T. E. MITCHELL,\* and A. H. HEUER\*

Department of Metallurgy and Materials Science, Case Western Reserve University, Cleveland, Ohio 44106

High-resolution electron microscopy was used to image incoherent  $\text{ZrO}_2/\text{Al}_2\text{O}_3$  interfaces in  $\text{ZrO}_2$ -toughened  $\text{Al}_2\text{O}_3$  containing intragranular  $\text{ZrO}_2$ . These particles are generally spherical but are sometimes faceted. High-resolution electron micrographs provide atomic-level information on the interfacial structure. For spherical particles, both ledgeline images and misfit dislocation-like images accommodated the lattice misfit, depending on the orientation of the interface, while faceted particles imply at least one low-energy  $\text{ZrO}_2/\text{Al}_2\text{O}_3$  interface.

## I. Introduction

ZIRCONIA-TOUGHENED alumina (ZTA) is the most important member of the wide class of  $\text{ZrO}_2$ -containing dispersion-toughened ceramics.<sup>1</sup> Such materials typically consist of modest amounts of  $\text{ZrO}_2$  (up to 30 vol%) dispersed in a fine-grained  $\text{Al}_2\text{O}_3$  matrix. The  $\text{ZrO}_2$  particles can have tetragonal (*t*) or monoclinic (*m*) symmetry, are incoherent with the  $\text{Al}_2\text{O}_3$  matrix, and can be either intergranular or intragranular (Fig. 1).

In the present paper, we will show high-resolution electron micrographs which provide information on the nature of the incoherent  $\text{ZrO}_2/\text{Al}_2\text{O}_3$  interfaces on an atomic level, particularly for intragranular  $\text{ZrO}_2$  particles. Intergranular  $\text{ZrO}_2/\text{Al}_2\text{O}_3$  interfaces appear to be wetted by an amorphous grain-boundary phase;<sup>2</sup> these interfaces have also been imaged by high-resolution electron microscopy (HREM), but these results will be reported elsewhere.<sup>3</sup>

## II. Experimental Procedure

ZTA samples containing 3.8, 10, and 15 vol%  $\text{ZrO}_2$  have been studied using HREM; the fabrication or provenance of the samples is described elsewhere.<sup>2</sup> All microscopy was performed in a transmission electron microscope\* dedicated to HREM and fitted with a top entry  $\pm 10^\circ$  tilting stage; the TEM pole piece has a *C*, (spherical aberration constant) of 1.1 mm. This microscope routinely provides point-to-point resolution down to 0.236 nm.

Thin-foil HREM samples were prepared by ion beam thinning

using conventional means, except that the thinned foils were annealed at 1200°C for 15 min before HREM examination. This annealing induced the (reverse) *m*  $\rightarrow$  *t* transformation in particles in which the (forward) *t*  $\rightarrow$  *m* transformation had occurred during foil preparation, a common occurrence in ZTA. (A preliminary report showing micrographs of an *m*- $\text{ZrO}_2/\text{Al}_2\text{O}_3$  interface, in which such a *t*  $\rightarrow$  *m* transformation had occurred in an intragranular  $\text{ZrO}_2$  particle during thin-foil preparation, has been published elsewhere.<sup>4</sup>)

Before describing our results, we note that imaging conditions for HREM are very stringent. Firstly, the foil must be very thin,  $\leq 20$  to 30 nm. Secondly, both the  $\text{ZrO}_2$  particle and the  $\text{Al}_2\text{O}_3$  matrix have to be oriented such that a low index zone axis for both phases is exactly (or nearly) parallel to the electron beam. Because the  $\text{ZrO}_2$  particles in these dispersion-toughened ceramics are randomly oriented with respect to their  $\text{Al}_2\text{O}_3$  matrices, this requirement is very difficult to satisfy, particularly as the interface itself should also be parallel to the electron beam. Of the more than 100  $\text{ZrO}_2$  particles examined to date, only a handful satisfied these difficult constraints. In this paper, we report images of two intragranular  $\text{ZrO}_2/\text{Al}_2\text{O}_3$  interfaces from which useful structural information can be obtained.

Thirdly, it is customary to take a through-focus series of images at various amounts of defocus, as the optimum defocus to achieve maximum structural information in the final image (the so-called Scherzer defocus) is difficult to know *a priori*.<sup>5</sup> Finally, unambiguous image interpretation requires exact image matching between computed (simulated) and experimental images, starting with assumed structural models and known microscope parameters (amount of defocus, *C*, etc.). While acceptable image matching for defect-free  $\text{ZrO}_2$  or  $\text{Al}_2\text{O}_3$  is straightforward (we have used both Skarmulis' CELLS program<sup>6</sup> and O'Keefe's SHRLI program<sup>7</sup> for this), modeling of the interface is much more difficult; this topic is currently a subject of much attention in our group. Because of the lack of computed interface images, our conclusions about interface structure must be considered tentative at this time.

## III. Results and Discussion

Two  $\text{ZrO}_2$  intragranular particles, one nearly spherical and one faceted, that satisfied the stringent HREM requirements are shown in Figs. 2(A) and (B), respectively. We discuss the spherical particle first.



Fig. 1. Typical microstructure of  $\text{ZrO}_2$ -toughened  $\text{Al}_2\text{O}_3$  showing (A) intergranular and (B) intragranular  $\text{ZrO}_2$  particles; a few particles are arrowed.

Received August 2, 1985; approved September 3, 1985.

\*Member, the American Ceramic Society.

\*Model 200CX, JEOL USA Inc., Peabody, MA.

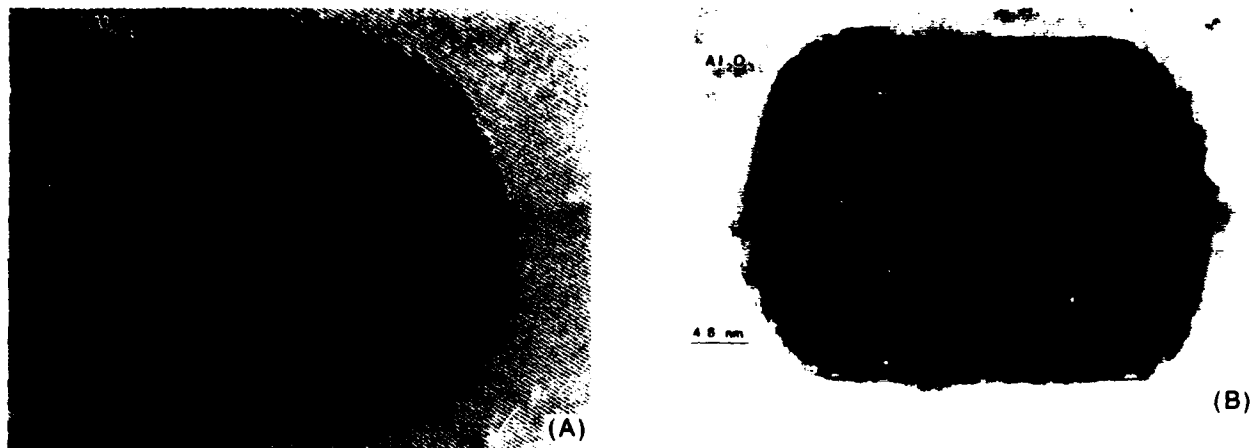


Fig. 2. (A) Intragranular  $\text{ZrO}_2$  particle; a single set of (111) planes is visible in  $\text{ZrO}_2$ , while  $\text{Al}_2\text{O}_3$  matrix is exactly oriented to  $[3\bar{1}2\bar{1}]$  zone. (B) Faceted  $\text{ZrO}_2$  particle in  $\text{Al}_2\text{O}_3$  matrix, which is oriented exactly to  $[10\bar{1}0]$  zone; note Moire fringes in  $\text{ZrO}_2$  particle.

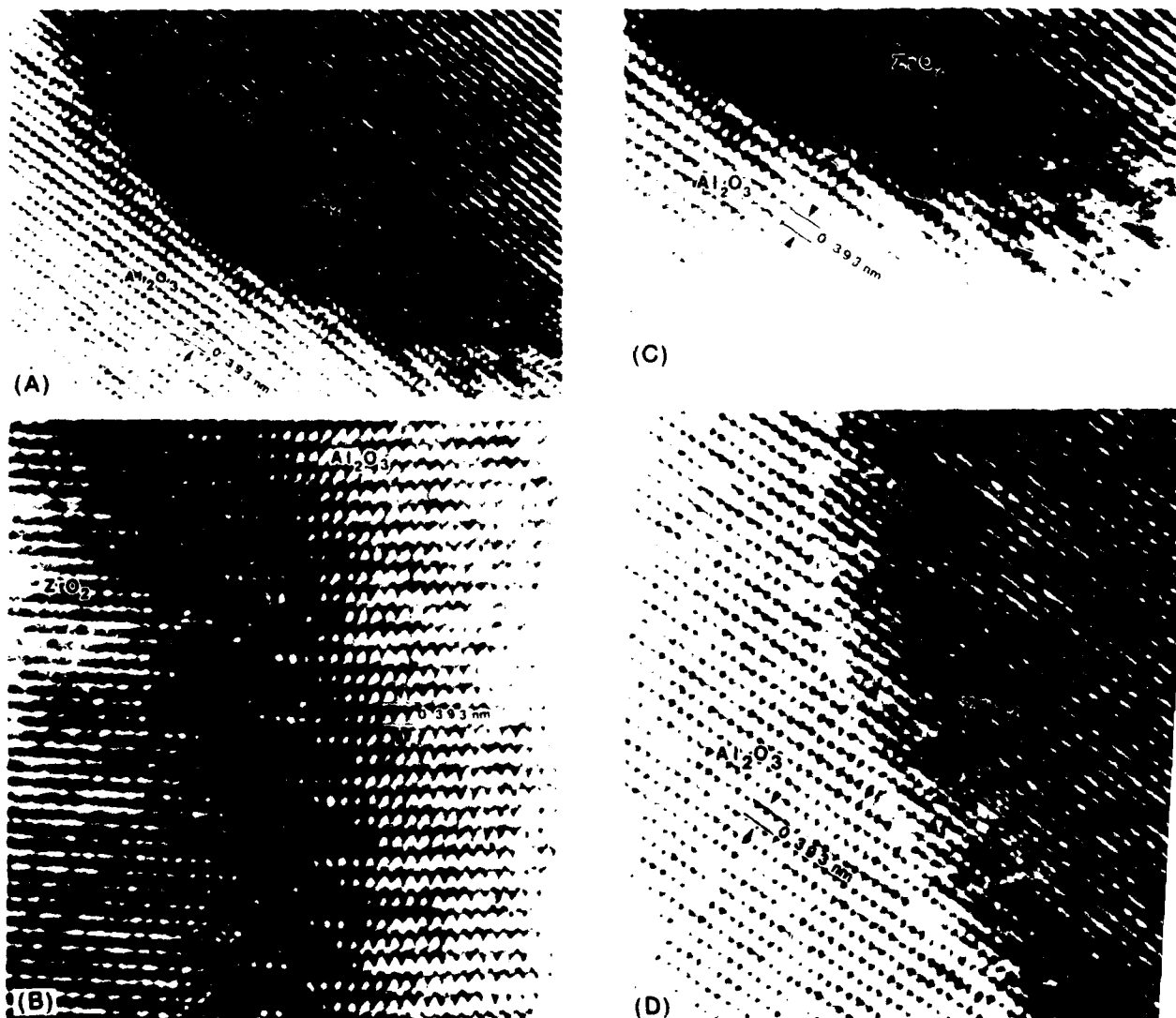


Fig. 3. Higher magnifications of various areas of Fig. 2(A). (A) Lattice mismatch accommodated by a series of ledges. (B) Periodicity changes at interface from every fourth  $\text{Al}_2\text{O}_3$  plane stopping short of interface (arrowed) to every third one. (C) Lattice mismatch accommodated by misfit dislocation. (D) Interface which appears smooth; sighting along atomic planes reveals misfit dislocations.

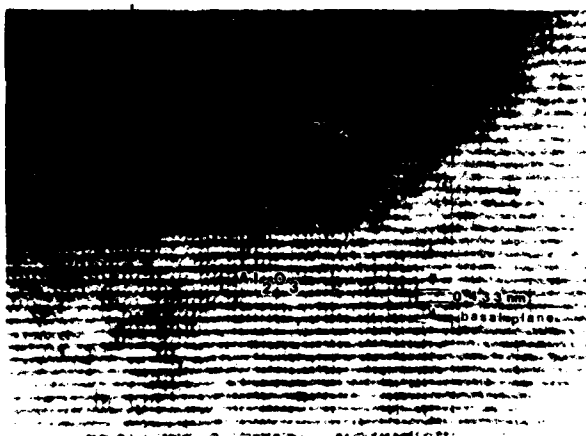


Fig. 4. Higher magnification of Fig. 2(B);  $\text{Al}_2\text{O}_3$  basal plane ( $d$  spacing of 0.433 nm) is parallel to  $\text{ZrO}_2$  facet.

As seen in the low-magnification micrograph of Fig. 2(A), the  $\text{Al}_2\text{O}_3$  matrix is oriented exactly to the  $[3\bar{1}21]$  zone axis and  $(0\bar{1}11)$  and  $(1\bar{1}04)$  planes can be discerned. On the other hand, the  $\text{ZrO}_2$  particle, which has  $t$  symmetry, has only a single set of  $(111)$  planes visible, as the closest zone axis  $[110]$  is tilted by a few degrees to the electron beam. The  $(111)$   $\text{ZrO}_2$  planes are misoriented by  $\approx 5^\circ$  from the  $(0\bar{1}11)$   $\text{Al}_2\text{O}_3$  planes; furthermore, the  $d$  spacings for these two sets of planes differ significantly, 0.295 nm for  $(111)$   $\text{ZrO}_2$  and 0.393 nm for  $(0\bar{1}11)$   $\text{Al}_2\text{O}_3$ . In spite of this marked lattice mismatch, no microcracks or other gross distortions appear in the HREM image of the interface.

Various regions of the  $\text{ZrO}_2/\text{Al}_2\text{O}_3$  interface are shown at higher magnification in Fig. 3. In the region shown in Fig. 3(A), the lattice mismatch between the two phases appears to be accommodated by a series of ledges, each one atomic plane high; such ledges are commonplace in semicoherent interfaces, as can occur between a precipitate and its matrix, but it is somewhat surprising to see them in the incoherent interface in Fig. 3(A).

$\text{Al}_2\text{O}_3$  and  $t\text{-ZrO}_2$  have significantly different thermal expansion coefficients ( $7 \times 10^{-6}$  to  $8 \times 10^{-6}$  and  $9 \times 10^{-6}$  to  $11 \times 10^{-6} \text{ } ^\circ\text{C}^{-1}$ , respectively, depending on orientation), and thermoelastic strains between 0.2% and 0.4% are expected, assuming the system was stress free during sintering and stress relief mechanisms are inoperable below  $\approx 1000^\circ\text{C}$ . (Thermal strains of this order have been detected by Rühle and Kriven<sup>8</sup> using HVEM techniques.)

Evidence for such strain is also available in the image of Fig. 3(A). As noted above, the  $t\text{-ZrO}_2$  is tilted  $\approx 2^\circ$  off its  $[110]$  zone axis such that only one set of  $(111)$  planes is being imaged. Near the interface, however, one set of  $(222)$  planes, with half the spacing of the  $(111)$  set, is visible, as well as an apparent structure image. We believe that the lattice bending due to these thermal expansion mismatch strains has tilted the lattice toward the  $[110]$  zone axis so that the  $(222)$  planes are apparent, but computer simulation is necessary to confirm this interpretation.

Figure 3(B) shows another region of the  $\text{ZrO}_2/\text{Al}_2\text{O}_3$  interface, which accommodates the lattice mismatch without any apparent use of ledges. This region of the interface exhibits a type of periodic quasi-fringe contrast in the low-magnification image of Fig. 2(A). At higher magnification this periodic contrast (at the top of Fig. 3(B)) is seen to be due to every fourth  $\text{Al}_2\text{O}_3$  plane (arrowed) extending less far into the interface than its neighboring planes. As

the interface orientation changes, so does the period of the interface structure, so that near the center of Fig. 3(B), it is every third  $\text{Al}_2\text{O}_3$  plane which stops short of the interface.

This periodic contrast has some similarities to misfit dislocations which can also exist in semicoherent interfaces to accommodate lattice mismatch; this type of mismatch accommodation is certainly in evidence in the region of interface shown in Fig. 3(C), although there are also ledge-like regions in conjunction with the dislocation-like regions in this micrograph. Finally, Fig. 3(D) shows a region of the interface which is apparently smooth and free of ledges; however, viewing along the planes of the images reveals the presence of periodic misfit dislocations. It appears that for this incoherent  $\text{ZrO}_2/\text{Al}_2\text{O}_3$  interface, the lattice mismatch is accommodated by a combination of ledges and misfit dislocations, depending on interface orientation.

A higher-magnification image of the faceted interface of Fig. 2(B) is shown in Fig. 4. As noted in this figure, the facet plane is parallel to the basal plane of  $\text{Al}_2\text{O}_3$ , and this orientation of  $\text{ZrO}_2/\text{Al}_2\text{O}_3$  interface must have a lower interfacial energy than any of the interface orientations of Fig. 3. Unfortunately, as will now be discussed, we have been unable so far to specify the  $\text{ZrO}_2$  orientation that leads to this low-energy interface.

It is common in HREM to determine the crystal orientation of the material under study by taking an optical diffraction pattern of the image, using a laser diffractometer; and the crystal orientations shown in Fig. 3 were determined in this way. The Moiré fringes visible in Fig. 4 indicate that this is not possible with this image; in spite of the fact that this region of foil appeared to be quite thin ( $\leq 20$  nm), the  $\text{ZrO}_2$  particle apparently does not go through the foil and must be overlaid with some of the  $\text{Al}_2\text{O}_3$  matrix. In fact, this suggests the existence of still another low-energy faceted  $\text{ZrO}_2/\text{Al}_2\text{O}_3$  interface, in this case parallel to the  $(10\bar{1}0)$  foil plane of Fig. 4. We are presently seeking other examples of faceted  $\text{ZrO}_2/\text{Al}_2\text{O}_3$  interfaces in which the  $\text{ZrO}_2$  extends through both the top and bottom of the foil so that the interface orientation can be specified exactly.

#### IV. Conclusion

HREM can be used to image incoherent  $\text{ZrO}_2/\text{Al}_2\text{O}_3$  interfaces in ZTA. Both spherical and faceted  $\text{ZrO}_2$  particles occur in ZTA; in the spherical particles, the mechanism of lattice accommodation of the two phases is a combination of ledges and misfit dislocations which depends on interface orientation.

The occurrence of faceted particles implies the existence of low-energy  $\text{ZrO}_2/\text{Al}_2\text{O}_3$  interfaces. Although we are not yet able to specify the  $\text{ZrO}_2$  orientation that leads to the low-energy interfaces, both basal  $(0001)$  and prism plane  $\{11\bar{2}0\}$   $\text{Al}_2\text{O}_3$  orientations appear to be present.

#### References

- Advances in Ceramics, Vol. 12, Science and Technology of Zirconia II. Edited by N. Claussen, M. Rühle, and A. H. Heuer. American Ceramic Society, Columbus OH, 1984.
- B. Kibbel and A. H. Heuer, "Exaggerated Grain Growth in  $\text{ZrO}_2$ -Toughened  $\text{Al}_2\text{O}_3$ ," this issue, pp. 231–36.
- S. P. Kraus-Lanteri, unpublished work.
- A. H. Heuer, S. Kraus-Lanteri, P. A. Labun, V. Lanteri, and T. E. Mitchell, "HREM Studies of Coherent and Incoherent Interfaces in  $\text{ZrO}_2$ -Containing Ceramics. A Preliminary Account," to be published in *Ultramicroscopy*.
- J. C. H. Spence, *Experimental High-Resolution Electron Microscopy*. Oxford University Press, New York, 1981.
- J. Skamulis, "A System for Interactive Electron Image Calculations," *J. Appl. Crystallogr.*, **12**, 636–38 (1979).
- M. A. O'Keefe and P. R. Buseck, "Computation of High Resolution TEM Images of Minerals," *Trans. Am. Crystallogr. Assoc.*, **15**, 27–46 (1979).
- M. Rühle and W. M. Kriven, "Analysis of Strain Around Tetragonal and Monoclinic Zirconia Inclusions," Proceedings of an International Conference on Solid-Solid Phase Transformations, Edited by H. I. Aaronson, D. E. Laughlin, R. F. Sekerka, and C. M. Wayman. American Institute of Mining, Metallurgical and Petroleum Engineers, Pittsburgh, PA, 1982.

TEF

# MORPHOLOGY OF TETRAGONAL PRECIPITATES

## IN PARTIALLY-STABILIZED $ZrO_2$

V. Lanteri, T.E. Mitchell and A.H. Heuer

Case Western Reserve University  
Dept. of Metallurgy and Materials Science  
Cleveland, Ohio 44106

### ABSTRACT

Tetragonal(t)  $ZrO_2$  precipitates in Mg-, Ca-, and Y- partially stabilized  $ZrO_2$  (Mg-PSZ, Ca-PSZ, Y-PSZ) have different habit planes and different morphologies. These differences arise because of differences in lattice parameters of precipitate and cubic (c)  $ZrO_2$  matrix in the three systems. The approximate {001} habit plane and oblate spheroid precipitate morphology observed in Mg-PSZ are explained in terms of anisotropic elasticity using the theory of Khachaturyan. The aspect ratio of  $\sim 5$  of these particles is used to calculate a c/t interfacial energy of  $\sim 0.15 \text{ Jm}^{-2}$ .

The aligned equiaxed precipitates observed in Ca-PSZ and the twinned colonies observed in Y-PSZ can also be explained using this theory and arise from interactions between strain fields during coarsening; the aligned particles in Ca-PSZ may actually represent an intermediate state before the formation of colonies in this system.

SUBMITTED TO  
✓ Adv. Met May 27<sup>th</sup>

Vincent

THE DISPLACIVE CUBIC  $\rightarrow$  TETRAGONAL TRANSFORMATION  
IN  $ZrO_2$  ALLOYS

by

A.H. Heuer, R. Chaim and V. Lanteri

Department of Metallurgy and Materials Science  
Case Western Reserve University, Cleveland, Ohio 44106

ABSTRACT

A displacive but non-martensitic cubic (c) to tetragonal (t) phase transformation is ubiquitous in  $ZrO_2$ - $Y_2O_3$  alloys containing from ~4 to ~13 wt%  $Y_2O_3$ . The microstructures of the transformed phase are characterized by the presence of anti-phase domain boundaries (APB's), similar to those present in ordered alloys, and in fine-grained polycrystals, by {101} twins. The latter are interpreted as mechanical deformation twins, which relieve the strains arising from the (small) tetragonality of the product phase and the (small) molar volume change accompanying transformation.

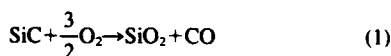
## Bubble Formation in Oxide Scales on SiC

DIANE M. MIESKOWSKI,\* T. E. MITCHELL,\* AND A. H. HEUER\*

Department of Metallurgy and Materials Science, Case Western Reserve University,  
Cleveland, Ohio 44106

*The oxidation of  $\alpha$ -SiC single crystals and sintered  $\alpha$ - and  $\beta$ -SiC polycrystals has been investigated at elevated temperatures. Bubble formation is commonly observed in oxide scales on polycrystalline SiC but is rarely found on single-crystal scales; bubbles result from the preferential oxidation of C inclusions, which are abundant in SiC polycrystals. The absence of bubbles on single crystals in fact implies that diffusion of the gaseous species formed on oxidation, CO (or possibly SiO), controls the rate of oxidation of SiC.*

SILICON carbide, along with other Si-containing nonoxide ceramics, has been studied extensively in recent years because of its potential application as a high-temperature structural material; oxidation resistance is of major importance in these applications. In the temperature range 1200° to 1400°C and at times <100 h,<sup>1-7</sup> passive oxidation of SiC follows a parabolic rate law. In the early stages of oxidation the oxide scale is primarily amorphous SiO<sub>2</sub>, but at longer times devitrification to cristobalite occurs. During passive oxidation, SiC and O<sub>2</sub> react according to



which is believed to occur at the SiC/SiO<sub>2</sub> interface as the result of the inward diffusion of oxygen through the scale.<sup>7-9</sup>

Bubble formation in the scale, which has been observed by several researchers using scanning electron and optical microscopy, has been attributed to CO evolution at the SiC/SiO<sub>2</sub> interface.<sup>4,6,10,11</sup> In the present research, bubble formation has been studied in greater detail by examining and comparing oxide scales on both single-crystal and polycrystalline SiC.

CONTRIBUTING EDITOR—T. O. MASON

Received August 15, 1983; revised copy received September 19, 1983; approved September 21, 1983.

Supported by the AFOSR under Grant No. F49620-78C-0053.

\*Member, the American Ceramic Society.

\*Now with Lewis Research Center, Cleveland, OH.

### EXPERIMENTAL PROCEDURE AND RESULTS

The materials studied included single-crystal  $\alpha$ -SiC<sup>1</sup> and sintered polycrystalline  $\alpha$ -<sup>2</sup> and  $\beta$ -<sup>3</sup> SiC. The surfaces of the samples were polished on polishing paper<sup>4</sup> using, successively, 30-, 15-, 6-, and 1- $\mu$ m diamond paste. Cleaning after polishing included a 1-h soak in a 20% HF solution to remove residual SiO<sub>2</sub> from the specimen surface. Specimens were oxidized in alumina boats in air or oxygen.

Comparison of the oxide scales formed on single-crystal and polycrystalline SiC showed that extensive bubble formation occurred only on the SiC polycrystals. Figure 1 is a scanning electron micrograph of the oxide formed on a sintered specimen and shows bubbles ranging in size from 1 to 4  $\mu$ m. Bubbles on specimens oxidized for longer times or at higher temperatures were larger, up to 20  $\mu$ m in diameter.

We believe that bubble formation arises from inclusions, which are common in both types of polycrystalline SiC we have studied, but rare in SiC single crystals. Figure 2 shows pits on the surface of an  $\alpha$ -SiC polycrystal after removal of

<sup>1</sup>High-purity vapor-phase-grown crystals supplied by R. Potter, General Electric Co., Cleveland, OH, and crystals from the Acheson process supplied by Elektroschmelzwerk, Munich, FRG, were used. They behaved similarly during oxidation and will not be further differentiated.

<sup>2</sup>Carborundum Co., Niagara Falls, NY.

<sup>3</sup>Courtesy of S. Prochazka, General Electric Co., Corporate Research & Development Center, Schenectady, NY.

<sup>4</sup>Texmet, Buehler Corp., Evanston, IL.

the oxide scale, whereas Fig. 3 shows inclusions of quite similar size on a polished but unoxidized sample of this material. The sample of Fig. 3 contained  $4.8 \times 10^4$  inclusions/mm<sup>2</sup>; for comparison, a sample oxidized at 1200°C contained  $4.8 \times 10^4$  pits/mm<sup>2</sup>, whereas samples oxidized at 1300° and 1400°C contained  $3.8 \times 10^4$  and  $4.4 \times 10^4$  pits/mm<sup>2</sup>, respectively. The inclusions in Fig. 3 were analyzed using X-ray energy dispersive spectroscopy on the scanning electron microscope, but only Si was detected; we therefore assume they are C inclusions, as reported by other workers (e.g. Ref. 12). We do not think that these inclusions acted as preferred nucleation sites for bubble formation, since the scale on a single crystal, which was deliberately pitted by "polishing" with 30- $\mu$ m diamond paste, followed by 6-, 3-, and 1- $\mu$ m pastes, was also bubble-free.

Bubbles were not particularly abundant at short oxidation periods, i.e. for scale thicknesses <0.3  $\mu$ m. Of course, C inclusions that intersect the free surface, such as those in Fig. 3, oxidized immediately after specimens were inserted into the oxidation furnace and did not give rise to bubbles. The absence of bubbles in thin scales implies that subsurface inclusions which are exposed by the progressive oxidation to the inward-growing scale do not give rise to bubbles until a critical thickness is reached. This observation permits inferences about gaseous diffusion through the scale. The flow rate,  $F$ , of a gas (in m<sup>3</sup>/s at 0°C and 10<sup>5</sup> Pa (1 atm) pressure per unit area of scale of thickness,  $x$ ) is given by

$$F = \frac{K(p_2 - p_1)}{x} \quad (2)$$

where  $K$  is the permeation constant (in m<sup>2</sup>/s),  $p_1$  the external pressure, and  $p_2$  the gas pressure at the SiC/scale interface. ( $K$  is actually the product of  $D$ , the diffusivity, and  $S$ , the solubility of the diffusing species in the scale.) The formation of bubbles clearly requires buildup of gas at the interface, and the critical scale thickness at which bubbles become abundant ( $\approx 0.3 \mu$ m) must be determined by  $K$  for silica glass for the gaseous species formed on oxidation of the inclusions.

Previous investigators<sup>4,6,7,11</sup> observed

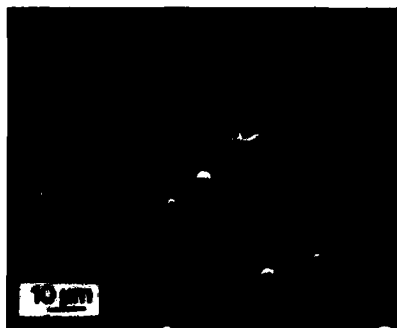


Fig. 1. Bubbles on oxide scale on  $\beta$ -SiC polycrystal (sample oxidized for 12.9 h at 1300°C in 10<sup>5</sup> Pa dry O<sub>2</sub>; scale thickness  $\approx 0.5 \mu$ m).



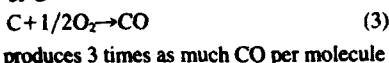
Fig. 2. Surface of  $\alpha$ -SiC polycrystal after removal of 1.1- $\mu$ m oxide scale by dissolution in HF (sample oxidized for 81.3 h at 1200°C in 10<sup>5</sup> Pa dry O<sub>2</sub>).



Fig. 3. Polished and unoxidized surface of sample of Fig. 2.

bubbles on polycrystalline SiC and thought that they resulted from the evolution of CO at the SiC/SiO<sub>2</sub> interface during oxidation—they apparently believed that CO could not diffuse readily through the scale and would, as a result, be released to the atmosphere in the form of bubbles. The lack of bubbles on single-crystal SiC shows that this argument is not correct and that diffusion of CO (and possibly SiO) has a  $K$  value large enough to prevent bubble formation. In fact, bubble formation resulting from oxidation of C inclusions in SiC polycrystals, its absence on SiC single crystals, and the superior oxidation resistance of SiC compared to Si (which also oxidizes by inward diffusion of oxygen) all imply that the rate of oxidation of SiC is controlled by the outward diffusion of CO (or SiO) and not by the inward diffusion of O<sub>2</sub>. This behavior must be related to subtle details of the diffusion processes, since both CO and O<sub>2</sub> are linear molecules with similar interatomic distances (C–O, 0.1128 nm; O–O, 0.1208 nm).<sup>13</sup> Actually, the possibility that the rate-controlling species is SiO rather than CO cannot be excluded at this time (the interatomic distance of SiO is 0.1509 nm<sup>13</sup>).

The CO generated by oxidation of the C inclusions must be produced at a rate sufficiently high that discrete bubbles form. This no doubt occurs because the oxidation of C



of O<sub>2</sub> diffusing through the scale as does the oxidation of SiC (cf. Eqs. (1) and (3)). Bubble formation will occur when the pressure at the substrate/scale interface is sufficient to overcome the ambient pressure and the force exerted by the surface energy of the oxide, i.e.

$$p_2 = p_1 + \frac{2\gamma}{r} \quad (4)$$

where  $\gamma$  is the surface energy of the oxide scale (assumed to be 0.3 J/m<sup>2</sup> for SiO<sub>2</sub><sup>14</sup>) and  $r$  the bubble radius. The bubbles observed on polycrystalline SiC range in size from  $\approx 1$  to  $\approx 20$   $\mu\text{m}$ , and the corresponding bubble pressures therefore range from  $\approx 1.3$  to  $\approx 7 \times 10^5$  Pa.

#### CONCLUSIONS

The permeability coefficients for the gaseous oxidation products formed during passive oxidation of SiC, CO, and possibly SiO are sufficiently high that bubble formation is not observed during oxidation of single-crystal SiC; diffusion of one of these gaseous species must be the rate-controlling step during oxidation. Carbon inclusions in polycrystalline SiC, however, give rise to quantities of CO large enough that bubbles can form. The smallest such bubbles are  $\approx 1$   $\mu\text{m}$  in diameter and contain gas at  $\approx 7 \times 10^5$  Pa pressure.

#### ACKNOWLEDGMENT

A. H. Heuer acknowledges the Alexander von Humboldt Foundation for a Senior Scientist Award, which permitted his sabbatical leave at the Max Planck Institut für Metallforschung, Stuttgart, FRG, where the final draft of this paper was prepared.

#### REFERENCES

- <sup>1</sup>G. Ervin, "Oxidation Behavior of Silicon Carbide," *J. Am. Ceram. Soc.*, **41** [9] 347–52 (1958).
- <sup>2</sup>R. F. Adamsky, "Oxidation of Silicon Carbide in the Temperature Range 1200°C to 1500°C," *J. Phys. Chem.*, **63**, 305–307 (1959).
- <sup>3</sup>P. J. Jorgensen, M. E. Wadsworth, and I. B. Cutler, "Oxidation of Silicon Carbide," *J. Am. Ceram. Soc.*, **42** [12] 613–16 (1959).
- <sup>4</sup>J. W. Hinze, W. C. Tripp, and H. C. Graham, pp. 409–19 in *Mass Transport Phenomena in Ceramics* (Materials Science Research, Vol. 9), Edited by A. R. Cooper and A. H. Heuer, Plenum, NY, 1975.
- <sup>5</sup>L. H. Keyes, pp. 681–96 in *Proceedings of the Symposium on Properties of High-Temperature Alloys with Emphasis on Environmental Effects*, Edited by Z. A. Foroulis and F. S. Pettit, The Electrochemical Society, Princeton, NJ, 1976.
- <sup>6</sup>S. C. Singhal, "Oxidation Kinetics of Hot-Pressed Silicon Carbide," *J. Mater. Sci.*, **11**, 1246–53 (1976).
- <sup>7</sup>J. A. Costello, "The Oxidation Behavior of Sintered Alpha- and Hot-Pressed Silicon Carbide Ceramics," M. S. Thesis, The Pennsylvania State University, August 1980.
- <sup>8</sup>K. Motzfeldt, "On the Rates of Oxidation of Silicon and Silicon Carbide in Oxygen, and Correlation with Permeability of Silica Glass," *Acta Chem. Scand.*, **18**, 1596–1606 (1964).
- <sup>9</sup>J. Schlichting, "Oxidation Kinetics of Silicon Ceramic From the View Point of Refractory Materials Against Hot Corrosion," *Rev. Int. Hautes Temp. Refract.*, **16** [1] 67–72 (1979).
- <sup>10</sup>J. E. Doherty, "Oxidation of Silicon Carbide," *Proc. EMSA*, **30**, 538–39 (1972).
- <sup>11</sup>J. Schlichting and J. Kriegesmann, "Oxidation Behavior of Hot-Pressed Silicon Carbide," *Ber. Dtsch. Keram. Ges.*, **56** [3–4] 72–75 (1975).
- <sup>12</sup>A. J. Bourdillon, N. W. Jepps, W. M. Stobbs, and O. L. Krivanek, "An Application of EELS in the Examination of Inclusions and Grain Boundaries of a SiC Ceramic," *J. Microscopy*, **124** [1] 49–56 (1981).
- <sup>13</sup>Tables of Interatomic Distances and Configuration in Molecules and Ions; Special Publication No. 11; London: The Chemical Society, Burlington House, WI (1958).
- <sup>14</sup>W. D. Kingery, H. K. Bowen, and D. R. Uhlmann, *Introduction to Ceramics*, 2d ed., Wiley, NY, 1976. □

Reprinted from the Journal of the American Ceramic Society, Vol. 68, No. 2, February 1985.  
Copyright 1985 by The American Ceramic Society

J. Am. Ceram. Soc., 68 [2] 49-58 (1985)

## REVIEW — Graphical Displays of the Thermodynamics of High-Temperature Gas-Solid Reactions and Their Application to Oxidation of Metals and Evaporation of Oxides

V. L. K. LOU\*

General Electric Company, Research and Development Center, Schenectady, New York 12301

T. E. MITCHELL\* and A. H. HEUER\*

Department of Metallurgy and Materials Science, Case Institute of Technology, Case Western Reserve University, Cleveland, Ohio 44106

The construction and utility of volatility diagrams — isothermal plots showing the partial pressures of two gaseous species in equilibrium with the several condensed phases possible in a system — are demonstrated for simple oxides with reference to the Mg-O, Al-O, and Si-O systems and compared with Ellingham-type representations of these same data. Both types of diagrams are useful for providing a condensed format for a great deal of thermodynamic information. Their use is illustrated by analyzing the oxidation of Mg, Al, and Si and the volatilization of MgO, Al<sub>2</sub>O<sub>3</sub>, and SiO<sub>2</sub> in both neutral and reducing gases.

### I. Introduction

THERMODYNAMIC data on many oxides, nitrides, carbides, and other high-temperature ceramics are readily available. Extensive compilations of such data are found in the Appendix of Kubaschewski's Metallurgical Thermochemistry,<sup>1</sup> the Metals Handbook,<sup>2</sup> the JANAF Tables,<sup>3</sup> and the Thermodynamical Properties of Inorganic Substances.<sup>4</sup> This information is essential for understanding high-temperature processing and high-temperature service of these ceramics, as well as the native metals from which they are made, but the data can be overwhelming. In the V-O system for example, the JANAF Tables report on the four states of vanadium metal and 10 different forms of oxides, and it is virtually impossible to use these data in practice without further calculation. Thus, when one is investigating the thermodynamics of a particular system, the question often is not whether the relevant data are available, but how to utilize the data.

Lengthy calculations can always be done on the dozen or more reactions that are possible in each system. This is not only inconvenient but often unsatisfactory, because in a complex system where many compounds exist, it is pertinent to have an overview of the relations between them, and formulae and calculations alone are generally unsatisfactory for this purpose. The best approach is often by graphical representation. The Ellingham or Richardson diagram is one example of the value of graphical representation. One single Ellingham diagram contains more information on metals and their oxides than pages of tabulated thermodynamic free

energies. In fact, this diagram contains full data on the oxidation/reduction behavior of solid oxides in all types of environments and at all temperatures and has proved to be indispensable to large numbers of users. Pourbaix diagrams are of similar usefulness to corrosion scientists. As will be discussed below it is possible to extend the utility of Ellingham diagrams to include data on volatilization of oxides.

High-temperature materials engineers are often confronted with gas-solid reactions of various types — oxidation, reduction, evaporation, etc. For example, gas-solid reactions are currently of considerable interest in nitride ceramics, in that these materials are much less stable than the traditional oxide ceramics, and N<sub>2</sub> evolution may be unavoidable during high-temperature processing or service. For more familiar ceramics, many oxides are sintered in H<sub>2</sub> or CO/CO<sub>2</sub> environments so that reactions involving volatile sub-oxides are important. The loss of dopants at high temperatures and the contamination of ceramic wares by impurities are further examples.

The standard Ellingham-type diagram can be helpful in some cases, but alternate representations are also useful. In particular, we have found that "volatility" diagrams are appropriate for dealing with high-temperature ceramics when more than one gaseous species is involved. Volatility diagrams are isothermal plots showing the partial pressures of two gaseous species in equilibrium with the various condensed phases possible in the system. They permit ready understanding of the high-temperature chemistry and allow appropriate processing and service conditions to be specified. Wagner<sup>5</sup> used them in his study of the volatilization of SiO and SiO<sub>2</sub> and Blegan.<sup>6</sup> Colguhoun, Wild, Grieveson, and Jack,<sup>7</sup> Gulbransen and Jansson,<sup>8,9</sup> and Singhal<sup>10</sup> used them to define stable phase fields in the Si-O-N and Si-O-C systems. The intent of this paper is to promote the use of this type of construction in ceramic applications and also to explore new ways of simplifying and clarifying the existing construction method. Three new construction features to be introduced are the *isomolar line*, the *isobaric lines*, and the *constant H<sub>2</sub>O/H<sub>2</sub> (or CO<sub>2</sub>/CO) lines*. This paper is devoted to three simple oxides — MgO, Al<sub>2</sub>O<sub>3</sub>, and SiO<sub>2</sub>; further papers will deal with the Si-O-N system and with ternary oxides, transition-metal oxides, and refractory metal oxides.

The new construction features and additional relevant data, in particular, the partial pressure of dominant metal vapor species, can be plotted on conventional Ellingham-type diagrams, and this graphical representation will be contrasted and compared with volatility diagrams. We also note that manipulation of the thermodynamic information we are treating can be handled by some of the

Received August 4, 1983; revised copy received May 17, 1984; approved October 17, 1984.

Supported by APOSR under Contract No. F49620-78C-0053.

\*Member, the American Ceramic Society.



Table I. Reactions in Mg-O, Al-O, and Si-O Systems Needed for Plotting Volatility Diagrams

Equation No.	Reaction	log K (1900 K)
1*	$2\text{MgO}(c) \rightarrow 2\text{Mg}(l) + \text{O}_2$	-21.32
2*	$\text{Mg}(l) \rightarrow \text{Mg}(g)$	1.28
3	$2\text{MgO}(c) \rightarrow 2\text{Mg}(g) + \text{O}_2$	-18.75
4*	$2\text{Mg}(l) + \text{O}_2 \rightarrow 2\text{MgO}(g)$	7.12
5	$\text{MgO}(c) \rightarrow \text{MgO}(g)$	-7.10
6	$\text{Al}_2\text{O}_3(c) \rightarrow 2\text{Al}(l) + \frac{3}{2}\text{O}_2$	-29.36
7	$\text{Al}(l) \rightarrow \text{Al}(g)$	-2.55
8	$\text{Al}_2\text{O}_3(c) \rightarrow 2\text{Al}(g) + \frac{3}{2}\text{O}_2$	-34.46
9	$4\text{Al}(l) + \text{O}_2 \rightarrow 2\text{Al}_2\text{O}(g)$	14.44
10	$\text{Al}_2\text{O}_3(c) \rightarrow \text{Al}_2\text{O}(g) + \text{O}_2$	-22.14
11	$\text{Al}_2\text{O}_3(c) + 4\text{Al}(l) \rightarrow 3\text{Al}_2\text{O}(g)$	-7.69
12	$2\text{Al}(l) + \text{O}_2 \rightarrow 2\text{AlO}(g)$	2.90
13	$2\text{Al}_2\text{O}_3(c) \rightarrow 4\text{AlO}(g) + \text{O}_2$	-52.91
14	$\text{Al}_2\text{O}_3(c) + \text{Al}(l) \rightarrow 3\text{AlO}(g)$	-25.00
15	$\text{Al}(l) + \text{O}_2 \rightarrow \text{AlO}_2(g)$	5.16
16	$2\text{Al}_2\text{O}_3(c) + \text{O}_2 \rightarrow 4\text{AlO}_2(g)$	-38.09
17	$2\text{Al}_2\text{O}_3(c) \rightarrow 3\text{AlO}_2(g) + \text{Al}(l)$	-43.25
18	$\text{SiO}_2(l) \rightarrow \text{Si}(l) + \text{O}_2$	-15.68
19	$\text{Si}(l) \rightarrow \text{Si}(g)$	-4.92
20	$\text{SiO}_2(l) \rightarrow \text{Si}(g) + \text{O}_2$	-20.60
21	$2\text{Si}(l) + \text{O}_2 \rightarrow 2\text{SiO}(g)$	13.86
22	$2\text{SiO}_2(l) \rightarrow 2\text{SiO}(g) + \text{O}_2$	-17.50
23	$\text{SiO}_2(l) + \text{Si}(l) \rightarrow 2\text{SiO}(g)$	-1.82
24	$\text{Si}(l) + \text{O}_2 \rightarrow \text{SiO}_2(g)$	8.29
25	$\text{SiO}_2(l) \rightarrow \text{SiO}_2(g)$	-7.30

\*Note that 1900 K is above the boiling point of Mg.

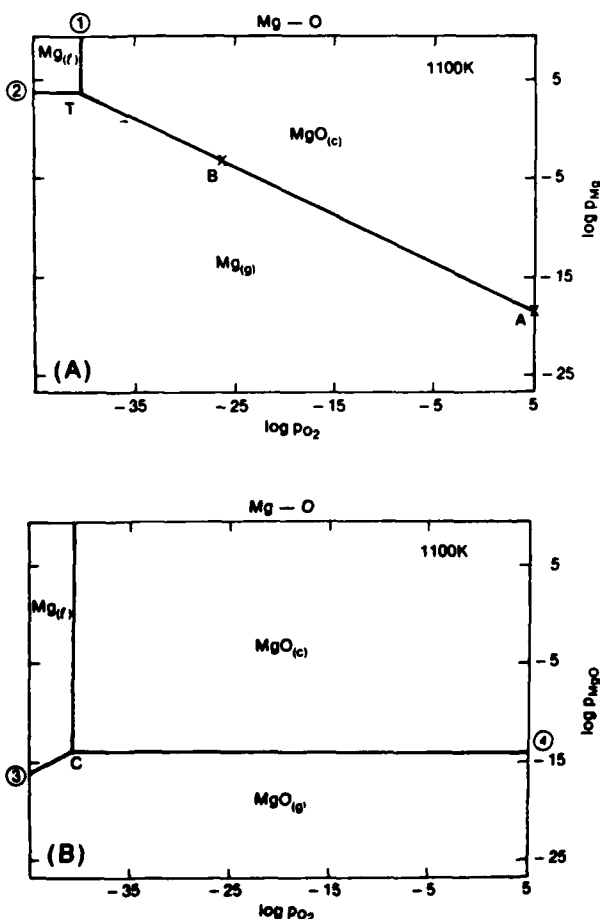


Fig. 1. (A) Volatility diagram for the Mg-O system at 1100 K for case when only Mg(g) is considered. In this and all other figures, pressures are given in Pa (1 atm =  $1.013 \times 10^5$  Pa). (B) Volatility diagram as per (A) but with MgO(g) considered.

computer programs now extant, e.g., SOLGASMIX.<sup>11</sup> However, graphical techniques have some advantages and our intention in this paper is to emphasize the ease of handling these data graphically using only the JANAF Tables. Before beginning our discussion, we note that, whether a computer program or a graphical display is used, there is always the danger of missing important species. *Caveat emptor!*

## II. Data Base—Gaseous and Nongaseous Phases

Three common oxide systems will be dealt with here—Mg-O, Al-O, and Si-O. The thermodynamic data appropriate for these systems are tabulated in the JANAF Tables. In the Mg-O system, they are Mg (reference state), Mg(c),<sup>\*</sup> Mg(l), Mg(g), Mg<sup>+</sup>(g), MgO(c), MgO(l), and MgO(g); in the Al-O system, they are Al (reference state), Al(c), Al(l), Al(g), Al<sup>+</sup>(g), AlO(g), AlO<sup>+</sup>(g), AlO<sub>2</sub>(g), AlO<sub>2</sub><sup>+</sup>(g), Al<sub>2</sub>O(g), Al<sub>2</sub>O<sub>2</sub>(g), α-Al<sub>2</sub>O<sub>3</sub>(c), γ-Al<sub>2</sub>O<sub>3</sub>(c), and Al<sub>2</sub>O<sub>3</sub>(l); and in the Si-O system, they are Si (reference state), Si(c), Si(l), Si(g), Si<sub>2</sub>(g), Si<sub>2</sub>(g), Si<sub>3</sub>(g), SiO(g), quartz SiO<sub>2</sub>(c), cristobalite SiO<sub>2</sub>(c), SiO<sub>2</sub>(l), and SiO<sub>2</sub>(g). For the temperature range of interest, all three metals and SiO<sub>2</sub> are in the liquid state, and one can reduce the condensed phases to Mg(l), Al(l), Si(l), MgO(c), α-Al<sub>2</sub>O<sub>3</sub>(c), and SiO<sub>2</sub>(l). Furthermore one can reduce the number of gaseous species to be considered, as many of them have very low vapor pressures. Thus, one can eliminate all the charged radicals as well as dimeric and trimeric compounds for their influences are exerted by their monomeric counterparts. The gaseous phases that need to be considered are Mg(g), MgO(g), Al(g), AlO(g), Al<sub>2</sub>O(g), Si(g), SiO(g), and SiO<sub>2</sub>(g).

Even with this reduced number of species in each system, a large number of reactions have to be considered. Volatility diagrams are useful when reactions involving at least one condensed species and no more than one volatile species (except oxygen) are considered: reactions involving only gases are neglected. Table I is a tabulation of the 25 various reactions in these systems needed for the diagrams; for convenience, log K values at 1900 K are also given. All can be represented in standard thermodynamic form, i.e.

$$\Delta G = RT \ln K \quad (K = \prod p_i^{a_i} / \prod p_i^{a_i})$$

where  $P$  stands for product,  $R$  for Reactant,  $a$  for activity, and  $n$  for integer.

## III. Construction and Utilization of Volatility Diagrams

### (1) The Mg-O System

(A) Construction: Volatility diagrams for oxides are always constructed with log p<sub>O<sub>2</sub></sub> as the abscissa and log p<sub>M</sub> or log p<sub>MO</sub> as the ordinate. At 1100 K, equilibrium constants for Eqs. (1) to (5) in Table I can be taken directly from the JANAF Tables or calculated from data given in these tables. Equation (1), which describes the oxidation of Mg to MgO, has an equilibrium constant of  $10^{-45.6}$  and, as it is independent of p<sub>Mg</sub>, is shown in Fig. 1(A) as vertical line 1-T, that separates the Mg(l) and MgO(c) phase fields. Similarly Eq. (2), the evaporation of liquid Mg, is independent of p<sub>O<sub>2</sub></sub> and is shown as the horizontal line 2-T. Equation (3) describes the evaporation of MgO to form Mg(g) and O<sub>2</sub>; as it involves both p<sub>Mg</sub> and p<sub>O<sub>2</sub></sub>, it is plotted in Fig. 1(A) as the sloping line T-A with a gradient of -1/2. The intersection of these three lines, T, indicates the minimum p<sub>O<sub>2</sub></sub> needed to prevent reduction of MgO(c) and the maximum p<sub>Mg</sub> possible in the system. At 1100 K the minimum log p<sub>O<sub>2</sub></sub> is -40.6 (Pa) and the maximum log p<sub>Mg</sub> is 3.8 (Pa). The significance of the sloping line is that p<sub>Mg</sub> decreases with increasing p<sub>O<sub>2</sub></sub>; thus, in an ambient pressure of  $10^5$  Pa (1 atm) of oxygen (point A), volatilization of MgO is unlikely because of the very low equilibrium partial pressure of Mg,  $10^{-14}$  Pa.

Normally, weight loss due to evaporation in a high-temperature experiment is important only if the vapor pressure of the evapo-

\*The suffix c stands for crystal, l for liquid, and g for gas.

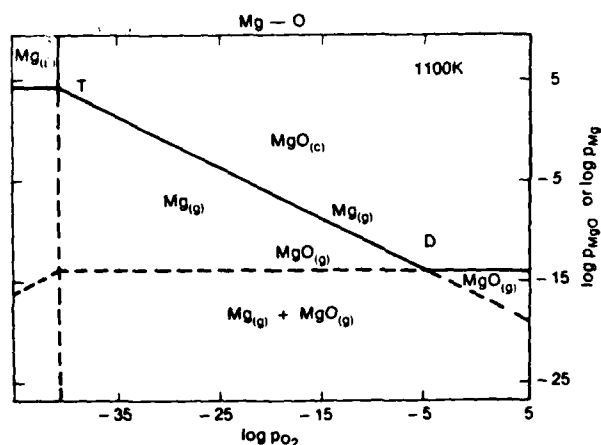


Fig. 2. Volatility diagram for the Mg-O system at 1100 K.

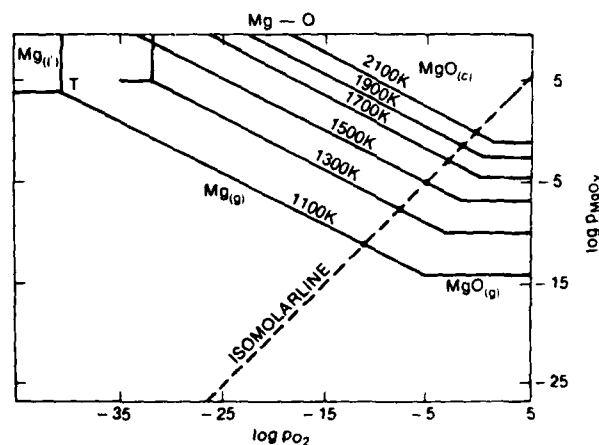


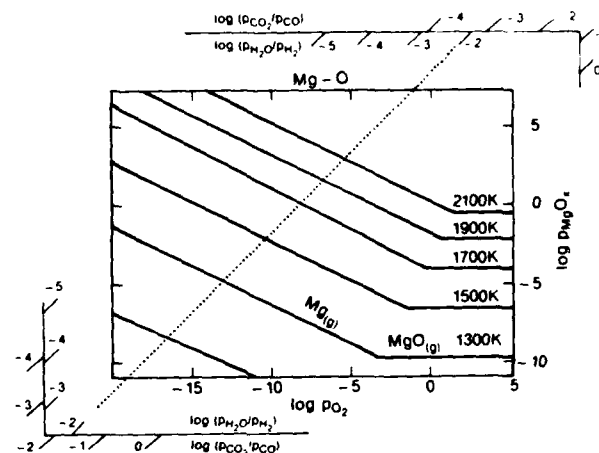
Fig. 3. Master volatility diagram for the Mg-O system from 1100 to 2100 K; isomolar line is defined in text.

rating species is higher than  $10^{-3}$  Pa. Point B in Fig. 1(A) corresponds to this arbitrary condition, and a decrease in  $p_{O_2}$  beyond this point will result in significant weight loss.

A similar diagram can be constructed for MgO vapor by utilizing Eqs. (1), (4), and (5), as shown in Fig. 1(B) where  $\log p_{MgO}$  is plotted on the ordinate instead of  $\log p_{Mg}$ . Equation (4) is an alternative oxidation reaction and depends on both  $p_{MgO}$  and  $p_{O_2}$ ; it is shown as the sloping line 3-C with a gradient of  $+1/2$ ; Eq. (5), which describes the evaporation of MgO vapor over solid MgO, is independent of  $p_{O_2}$  and constant at  $10^{-14}$  Pa (line C-4). The next step in the construction is to combine Figs. 1(A) and (B) into one diagram and to discard unimportant lines, as shown in Fig. 2. In the approximation we use, only the solid lines are important in this figure because the dashed lines represent species with smaller vapor pressures; we henceforth refer to these solid lines as maximum equilibrium pressure lines for obvious reasons. The intersection D, which we shall call the major vapor transition point, delineates the field where the major vapor species changes; to its right, it is MgO vapor and to its left, it is Mg vapor. It is easy to construct a number of such simple isothermal volatility diagrams which can be combined into a master diagram covering the temperature range of interest. Figure 3 is such a diagram for the Mg-O system and contains all the vital thermodynamic data on volatilization reactions between 1100 and 2100 K.

(B) *Evaporation of MgO in Vacuum and Inert Gases and the Use of the Isomolar Line:* When MgO(g) is the major species, i.e., at values of  $p_{O_2}$  to the right of point D, the vapor pressure of MgO in a closed system will be constant; the evaporation of MgO to MgO(g) (reaction 5) does not depend on  $p_{O_2}$ . However, if the  $p_{O_2}$  is reduced, the principal vapor species will change to Mg(g) and the vapor pressure will increase following the line T-D in Fig. 2.

However, there is one other important fact of such an experiment that must be considered, the *mass balance criterion*. When 1 mol of MgO(c) undergoes evaporation via Eq. (3), 1 mol of Mg(g) and  $1/2$  mol of  $O_2$  are produced. Assuming ideal gas behavior and equal diffusivity of all gaseous species, the mass balance criterion stipulates that  $p_{Mg} = 2p_{O_2}$  or  $\log p_{Mg} = \log p_{O_2} + \log 2$ . This relation is shown in Fig. 3 as the dashed line. We henceforth refer to it as an *isomolar line* and its gradient is always 1. At the point of intersection of the isomolar line with a maximum equilibrium pressure line, both the mass balance criterion and the thermochemistry are satisfied. The predicted equilibrium vapor pressures above crystalline MgO at 1900 K, for example, are  $p_{Mg} = 0.1$  Pa and  $p_{O_2} = 0.05$  Pa. Other isomolar points are also indicated by filled circles. Conceptually, when an MgO crystal dissociates into Mg vapor and  $O_2$ , the respective partial pressures are controlled in a fixed ratio by the equilibrium constant. The isomolar line defines the maximum  $p_{Mg}$  over MgO(c) in a

Fig. 4. Volatility diagram for Mg-O system with H<sub>2</sub>O/H<sub>2</sub> and CO<sub>2</sub>/CO nomographs included.

nonreactive environment and sets a limit to the valid portion of the volatility diagram; only conditions to the right of this line are attainable.

(C) *Evaporation of MgO in Reducing Gases and the Use of the Isobaric Lines:* It is well-known that reducing gases can cause severe weight loss of MgO at high temperatures; volatility diagrams can predict the vapor pressures of various gaseous species involved in the high-temperature reactions. In fact the isomolar point at any particular temperature is no longer applicable as the Mg vapor pressure is much higher with a reactive gas. For example, in the case of hydrogen with an H<sub>2</sub>O to H<sub>2</sub> ratio of  $10^{-2}$ , the JANAF Tables predict that  $\log p_{O_2}$  at 1900 K will be  $-6.7$  (Pa), and according to Fig. 3 the corresponding  $\log p_{Mg}$  is 1.5 (Pa). The calculation can be repeated for other temperatures, and the argument presented in the Appendix shows that for a specific H<sub>2</sub>O to H<sub>2</sub> ratio, the equilibrium  $p_{O_2}$  and  $p_{Mg}$  for various temperatures fall on a single straight line; the dotted line in Fig. 4 is constructed for an H<sub>2</sub>O to H<sub>2</sub> ratio of  $10^{-2}$ . As can be seen in this figure, a nomographic-type construction is possible: a straight edge can be placed on any desired H<sub>2</sub>O to H<sub>2</sub> (or CO<sub>2</sub> to CO) ratio so that the equilibrium  $p_{O_2}$  above MgO can be determined at any temperature. The effect of moisture in the ambient is easily predicted from Fig. 4. At 1900 K, for example, if the H<sub>2</sub>O to H<sub>2</sub> ratio changes from  $10^{-2}$  to  $10^{-1}$ ,  $\log p_{Mg}$  increases from 1.5 to 2.5 (Pa) and the

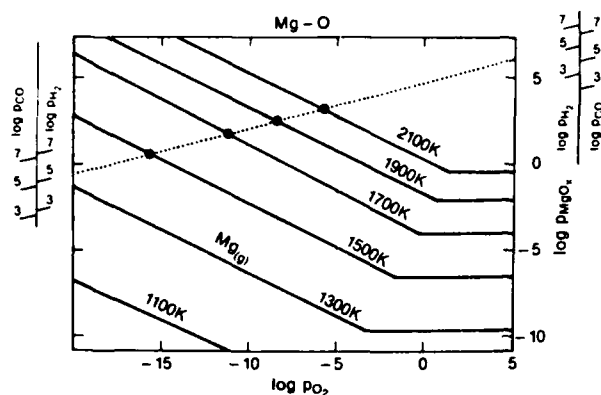


Fig. 5. Volatility diagram for the Mg-O system with isobaric line (dotted) included.

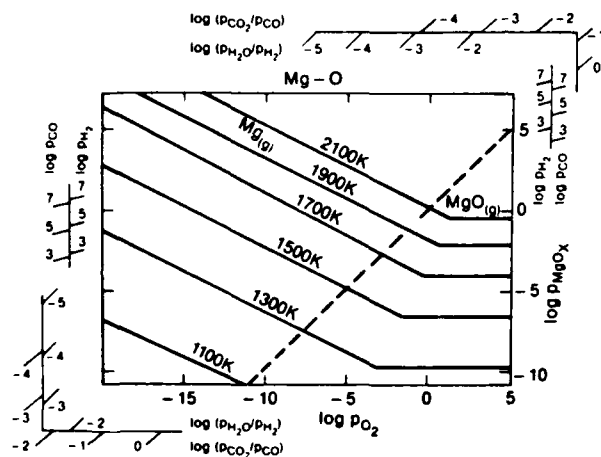
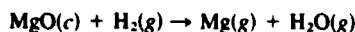


Fig. 6. Complete volatility diagram for the Mg-O system.

evaporation rate should likewise increase.

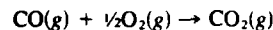
At first sight,  $p_{Mg}$  can increase up to the point  $T$  where  $Mg(l)$  and  $MgO(c)$  are in equilibrium with  $MgO(g)$ . However, such a direct interpretation of the volatility diagram must be modified to take cognizance of the mass balance. The reaction between  $MgO$  and  $H_2$  is



and using the same assumption we made earlier, for every mole of  $Mg$  vapor produced, 1 mol of  $H_2O$  vapor is also produced. As in the case of the nonreactive environment, the volatilization reaction creates its own environment. One can calculate the equilibrium  $p_{Mg}$  and  $p_{H_2O}$  for this reaction by making the simple assumption that  $p_{Mg} = p_{H_2O}$ . At 1900 K in  $10^5$  Pa of dry  $H_2$ , for example, the vapor pressure of  $H_2O$  or  $Mg$  is  $10^{2.2}$  Pa. We refer to this point as the *isobaric point*; it is shown in Fig. 5 as a filled circle and indicates the maximum  $Mg$  vapor pressure allowed for any  $p_{H_2}$  at one particular temperature.

The Appendix also shows that the isobaric points at constant  $p_{H_2}$  and various temperatures should fall on a straight line, the *isobaric line*, as can be seen in Fig. 5. In fact, as shown in this figure, the best way of representation is to include additional scales on the ordinates, i.e., to create another nomograph; the position of an isobaric point can be determined by placing a straightedge across the diagram for the particular  $H_2$  pressure of interest. The effect of  $CO$  can be determined on a similar basis by using the

corresponding  $CO$  scales, which are derived from the reaction



Thus, the final volatility diagram for  $MgO$  is shown in Fig. 6. The range of validity of the diagram for nonreactive ambients is to the right of the isomolar line. For reducing environments,  $H_2/H_2O$  or  $CO/CO_2$ , the  $CO$  or  $H_2$  nomograph is used for any particular pressure to define the validity of the volatility diagram—for any temperature, to the right of the intersection of a straight line connecting the  $CO$  or  $H_2$  scales and the maximum equilibrium pressure line. For a given  $H_2O$  to  $H_2$  or  $CO_2$  to  $CO$  ratio, the appropriate scales are used to determine the equilibrium pressure on the maximum equilibrium pressure line. It is clear that all available thermodynamic information has been included in Fig. 6 in a compact and useful form.

Two additional points concerning the nomographic construction should be noted. Firstly, there is the question of volatile hydroxides and in this case  $Mg(OH)_2(g)$  is the most volatile (OH)-containing species. However, our calculations based on values tabulated in the JANAF Tables suggest that it is a minor species under normal pressures and  $H_2O$  to  $H_2$  ratios of less than  $10^{-2}$ . Therefore, in Fig. 6, the highest  $\log H_2O/H_2$  value on the scale is  $-2$ . Actually, this is not a particularly severe limitation. A  $p_{H_2O}$  to  $p_H$  ratio of  $10^{-2}$  corresponds to a dew point of  $+7^\circ C$ , and  $Mg(OH)_2$  formation therefore requires injection of steam into the system. Under conditions where  $Mg(OH)_2$  does form, a completely different type of volatility diagram is required. Normally hydroxides are important only at high  $p_{H_2O}$  and low temperature.

With regard to the  $CO_2/CO$  scale, the limitation here is sooting of carbon, and the condition for that in the present temperature range is a  $CO_2$  to  $CO$  ratio of about  $10^{-4}$ . Again this is reflected in Fig. 6, where the minimum value on the  $\log CO_2/CO$  scale is  $-4$ .

(D) *Use of Ellingham-Type Diagrams:* A useful alternative to the volatility diagram is to plot the data on the standard Ellingham-type diagram.<sup>1</sup> Clearly, either form will suffice since volatility diagrams are plots of equilibrium  $p_{O_2}$  vs equilibrium  $p_{MO}$ , for various temperatures, while the Ellingham-type diagrams have equilibrium  $p_{O_2}$  and  $T$  as the abscissa and ordinate, respectively, for various  $p_{MO}$  values. Such a diagram for the  $Mg-O$  system is constructed in Fig. 7, where in accord with standard practice, the temperature is given in  $^\circ C$  rather than  $K$  and the abscissa is actually  $RT \ln p_{O_2}$ . The nomographic constructions for  $p_{O_2}$ ,  $H_2O$  to  $H_2$  ratio, and  $CO_2$  to  $CO$  ratio scales are well-known and will not be discussed. The data usually included in the Ellingham diagram define the oxidation of  $Mg$  to solid  $MgO$ , which are plotted as lines 1 and 3. The former represents the oxidation of solid or liquid  $Mg$  and the latter the oxidation of  $10^5$  Pa of  $Mg$  vapor;  $M$  is the melting point of  $Mg$ . Solid  $MgO$  is stable only above these lines, and the intersection of the two lines,  $B$ , is the boiling point of  $Mg$ . The vapor pressure of  $Mg$  over condensed  $Mg$  (Eq. (2)) at various temperatures is shown as a series of vertical lines (below line 1); lines corresponding to  $>10^5$  Pa  $Mg$  pressure are not drawn. The vapor pressure of  $Mg$  over solid  $MgO$  plots as a series of sloping lines which are appropriately labeled in Fig. 7. Finally, the vaporization of  $MgO$  via Eq. (5) is shown as a series of vertical lines at the top of the diagram, line 4 corresponding to  $p_{Mg} = 10$  Pa. Line 5 is the locus of the points marked  $D$  on Fig. 2 and denotes, for a given  $p_{Mg}$ , the  $p_{O_2}/T$  conditions where the major vapor species changes from  $Mg$  vapor (below the line) to  $MgO$  vapor (above the line).

At any  $p_{O_2}$ , the relevant  $p_{Mg}$  or  $p_{MgO}$  pressure can be obtained by noting which isobar passes through the intersection of the line between that  $p_{O_2}$  and point  $O$  on the left-hand vernier of the nomograph at a given  $T$ . (For example,  $p_{Mg}$  is 10 Pa at  $1800^\circ C$  at  $p_{O_2} = 10^{-2.5}$  Pa.) In any  $H_2O/H_2$  (or  $CO_2/CO$ ) mixture, a straightedge is placed between  $H$  (or  $C$ ) on the vernier and the relevant gas mixture and likewise gives the  $p_{MgO}$  pressure as a function of temperature.

As in the volatility diagram, the valid regions of the Ellingham diagram can be determined using the mass balance criterion. In

<sup>1</sup>This was pointed out by a reviewer of an earlier version of this paper.

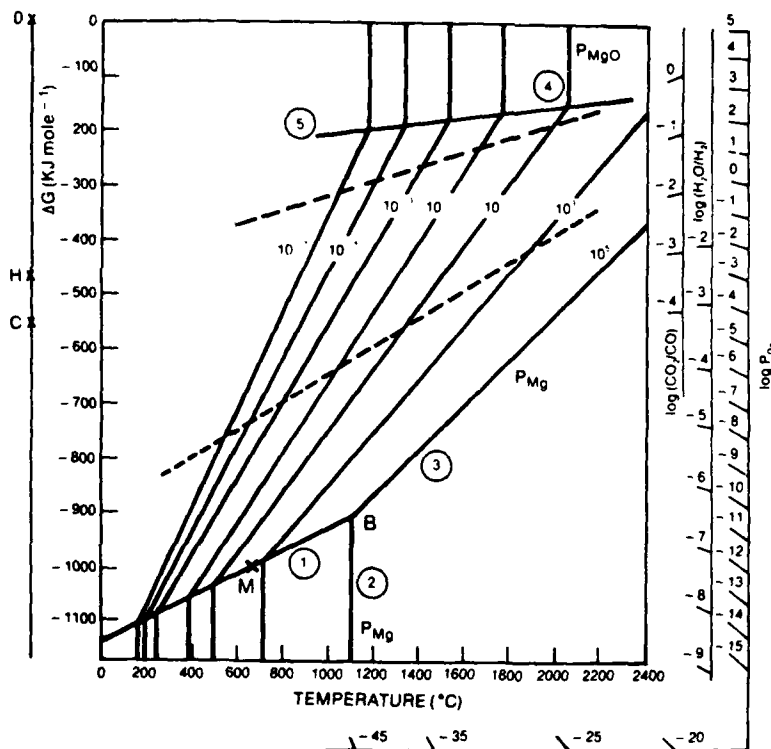


Fig. 7. Ellingham-type diagram for the Mg-O system.

vacuum or inert gases,  $p_{Mg}$  has to be equal to or less than  $2p_{O_2}$  and such a condition is shown by the long-dashed isomolar line; the diagram is only valid above this line. In practice, for a given temperature, say 2000°C, the maximum Mg vapor pressure is found by noting which isobar intersects the point where the isomolar line crosses 2000°C; in addition, placing a straightedge through this point and point O on the vernier yields the minimum  $p_{O_2}$  as  $10^{0.5}$  Pa.

The isobaric lines are constructed in a similar way, by noting that the limiting condition is  $p_{Mg} < p_{H_2O}$ . At  $10^5$  Pa  $H_2$ , for example, the isobaric line is constructed (the short-dashed line in Fig. 7) by noting the temperature at which a straight line between the H vernier and a series of  $H_2O$  to  $H_2$  ratios intersects the appropriate  $p_{Mg}$  isobar; the isobaric point for  $p_{H_2O} = 10^1$  Pa is at 1900°C; for 10 Pa it is 1350°C; for  $10^{-1}$  Pa it is 1050°C, etc. The diagram is only valid above the short-dashed line in such an atmosphere.

## (2) The Al-O System

(A) Construction: The JANAF Tables list 15 metallic and oxide phases in this system, of which six are relevant to the present discussion—Al(l),  $\alpha$ -Al<sub>2</sub>O<sub>3</sub>(c), Al(g), Al<sub>2</sub>O(g), AlO(g), and AlO<sub>2</sub>(g). The 1900 K isothermal section is chosen to demonstrate the construction. The vertical line in Fig. 8 represents the oxidation of Al(l) to  $\alpha$ -Al<sub>2</sub>O<sub>3</sub> (Eq. (6) in Table I) and the logarithmic value of the equilibrium constant is -29.4, from which  $\log p_{O_2}$  is deduced to be -14.6 (Pa). The four lines to the left of this vertical line represent the vapor pressures of the four vapor species over metallic aluminum, namely Al(g), Al<sub>2</sub>O(g), AlO(g), and AlO<sub>2</sub>(g), corresponding to the chemical reactions described by Eqs. (7), (9), (12), and (15). The gradients of these lines can be determined from the ratio between oxygen and the volatile species, such that for Eq. (7) it is 0, for Eq. (9) it is  $\frac{1}{2}$ , for Eq. (12) it is  $\frac{1}{2}$ , and for Eq. (15) it is 1. To the right of the vertical line, the four lines represent vapor pressures of the same four species over  $\alpha$ -Al<sub>2</sub>O<sub>3</sub> and the corresponding reactions are described by Eqs. (8), (10), (13), and (16), for which the corresponding gradients are  $-\frac{3}{4}$ , -1,  $-\frac{1}{4}$ , and  $\frac{1}{4}$ . For each volatile species, the lines intersect on the vertical line to form a "triple" point where Al(l) and Al<sub>2</sub>O<sub>3</sub>(c) are in equilibrium with a gaseous species;

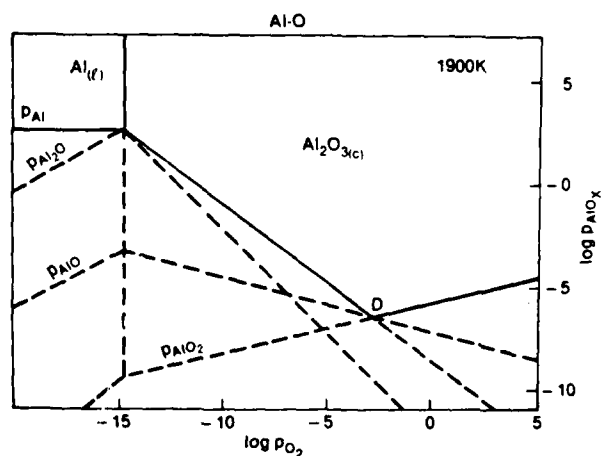


Fig. 8. Volatility diagram for the Al-O system at 1900 K.

in cases where the gases are more reduced than Al<sub>2</sub>O<sub>3</sub>, i.e., Al(g), Al<sub>2</sub>O(g), and AlO(g), the triple points indicate the maximum possible vapor pressure of these gaseous species. These can be calculated according to Eqs. (7), (11), and (14), and their logarithmic values are 3.4, 3.4, and -3.3 (Pa). For AlO<sub>2</sub>(g), which is more oxidized than Al<sub>2</sub>O<sub>3</sub>, the triple point does not represent the maximum vapor pressure, as it continues to increase in the oxide phase field (the reaction at this triple point is Eq. (17)). For practical purposes, the important lines in this diagram are the solid lines which show the vapor pressures of the most volatile species. It is apparent that under the most reducing conditions, the major vapor species is Al vapor but under more oxidizing conditions, i.e., to the right of D in Fig. 8, it is AlO<sub>2</sub>(g). By use of this simplified construction, the 1700 and 2100 K sections are added in Fig. 9.

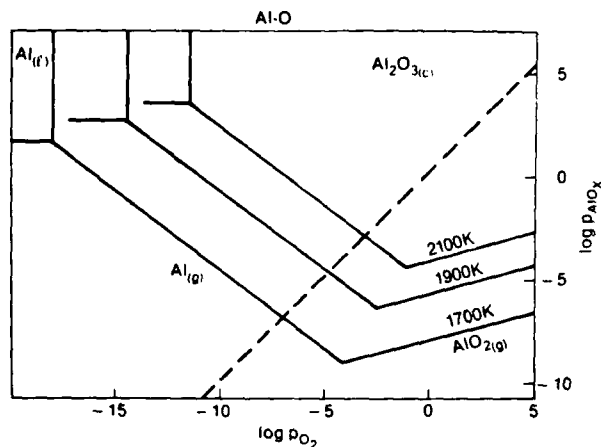


Fig. 9. Master volatility diagram for the Al-O system from 1700 to 2100 K.

(B) *Vacuum and Inert Gases:* The next step in the construction is to put in the isomolar points by considering the decomposition reaction



and the corresponding isomolar lines ( $\log p_{\text{O}_2} = \log \frac{3}{4} + \log p_{\text{Al}}$ —the dashed line in Fig. 9). From the intersections one can predict the maximum vapor pressures of Al(g) and oxygen over  $\alpha\text{-Al}_2\text{O}_3$  in a nonreactive system; for example at 1900 K,  $\log p_{\text{Al}} = -4.8$  (Pa) and  $\log p_{\text{O}_2} = -5.0$  (Pa). We stress again that the significance of the isomolar line is to define the valid portion of the diagram such that only the area to its right is accessible in nonreactive ambients.

(C) *H<sub>2</sub> and CO:* The nomographic construction of the iso-

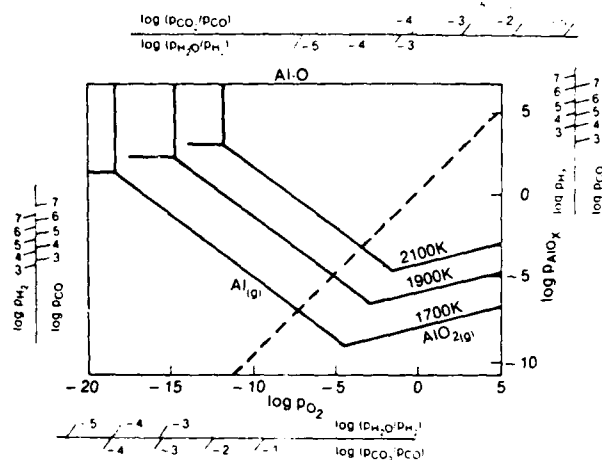
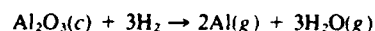


Fig. 10. Complete volatility diagram for the Al-O system.

baric lines in Fig. 10 is similar to that in the Mg-O system except that isobaric points are calculated according to the mass balance criterion  $p_{\text{H}_2\text{O}} = \frac{1}{2}p_{\text{Al}}$  which follows from the reaction



The intersections with the maximum equilibrium pressure lines indicate the maximum vapor pressures at various temperatures; for example, at  $10^5$  Pa of dry hydrogen at 1900 K,  $\log p_{\text{Al}}$  cannot exceed 0.3 (Pa). As with the Mg-O diagram, the CO scale is also included in the diagram. The constant  $\text{H}_2\text{O}/\text{H}_2$  and  $\text{CO}_2/\text{CO}$  lines are likewise included and  $p_{\text{Al}}$  under various ratios of these gases can be readily determined. The range of these scales are again limited by reasons explained previously; for the  $\text{H}_2\text{O}/\text{H}_2$  scale, the upper limit is  $10^{-3}$  (dew point of  $-20^\circ\text{C}$ ) and for the  $\text{CO}_2/\text{CO}$  scale

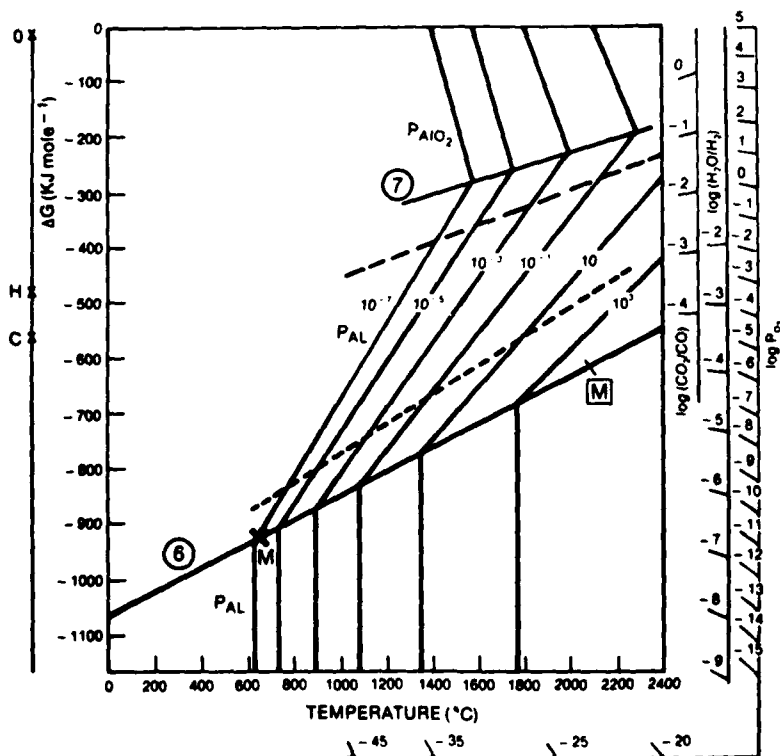


Fig. 11. Ellingham-type diagram for the Al-O system.

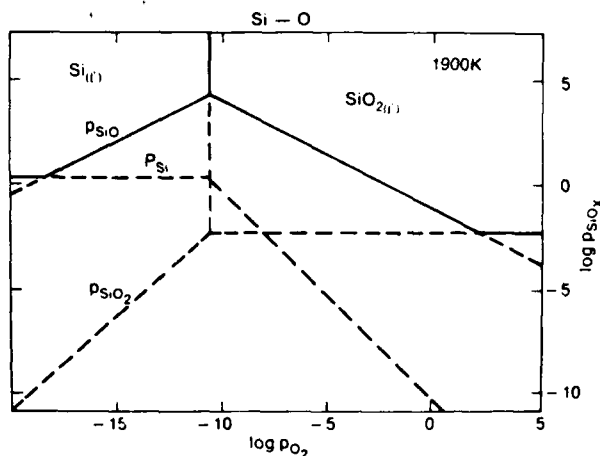


Fig. 12. Volatility diagram for the Si-O system at 1900 K.

the lower limit is  $10^{-4}$ . It should again be cautioned that the region of validity for any  $H_2$  or  $CO$  pressure is to the right of the corresponding isobaric line.

(D) *Ellingham Diagram*: The Ellingham-type compilation of the thermodynamic data for the Al-O system is shown in Fig. 11 and differs from Fig. 7 mainly in the vapor species found at high  $p_{O_2}$ 's; the constant  $p_{AlO_2}$  lines slope to the left and the transition from  $p_{Al}$  to  $p_{AlO_2}$  as the principal vapor species is shown as the line marked 7. Line 6 delineates the transition from Al (solid or liquid) to  $Al_2O_3$  (solid or liquid) as the condensed phase, with  $M$  and  $\bar{M}$  being the conventional symbols for the melting points of the metal and oxide, respectively.

### (3) The Si-O System

(A) *Construction of the Diagram*: The important phases in this system are  $Si(l)$ ,  $SiO_2(l)$ ,  $Si(g)$ ,  $SiO(g)$ , and  $SiO_2(g)$ . By use of values listed in the JANAF Tables, the 1900 K volatility diagram is shown in Fig. 12. The vertical line represents the oxidation of Si to  $SiO_2$  (Eq. (18)), the three lines to its left describe the vapor pressures of  $Si(g)$ ,  $SiO(g)$ , and  $SiO_2(g)$  over  $Si(l)$ , according to Eqs. (19), (21), and (24), respectively, and the three lines to its right describe the vapor pressures over  $SiO_2(l)$ , according to Eqs. (20), (22), and (25). The most volatile species is  $SiO(g)$ , whereas  $Si(g)$  and  $SiO_2(g)$  are relatively unimportant except at low and high  $p_{O_2}$ , respectively, where they become the major vapor species.

The rest of the construction is identical with the previous two systems and only a brief description will be given here. Firstly, in Fig. 13, the 1700 and 2100 K isothermal sections are included and the isomolar line, which satisfies the mass balance conditions of Eq. (22), is also drawn. As before, this line delineates the valid region of the diagram when the system is under a non-reactive environment. In hydrogen, Fig. 14 is drawn to accommodate the mass balance corresponding to the  $SiO_2$ - $H_2$  reactions:  $SiO_2(l) + H_2 \rightarrow SiO(g) + H_2O(g)$ . The maximum  $SiO(g)$  vapor pressure is a function of the hydrogen pressure, and for example at 1900 K and  $p_{H_2} = 10^3$  Pa,  $\log p_{SiO}$  cannot exceed +2.6 (Pa). Isobaric points for other temperatures and pressures can be determined from Fig. 14. The valid portion of the diagram is to the right of the corresponding isobaric line, where  $p_{SiO}$  is determined by the  $H_2O$  to  $H_2$  ratio of the environment. Similarly, in  $CO_2/CO$  mixtures,  $p_{SiO}$  can be determined from the diagram by using the corresponding  $CO_2/CO$  scale and the valid region of this scale is defined as before.

The Ellingham-type compilation of the data is included in Fig. 15. Line 8 delineates the transition from Si to  $SiO_2$  as the condensed phase, and lines 9 and 10 show, respectively, transitions from  $SiO$  to  $SiO_2$  and from Si to  $SiO$  as the principal vapor species.

(B) *Active Oxidation*: The Si-O system is unique in that

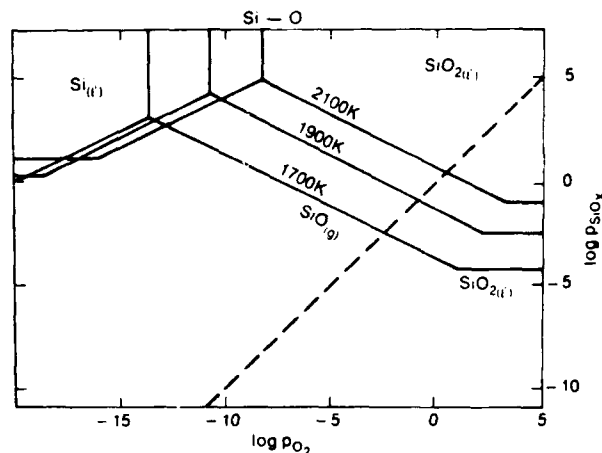


Fig. 13. Master volatility diagram for the Si-O system from 1700 to 2100 K.

over a large range of  $p_{O_2}$ 's, the sub-oxide ( $SiO$ ) is the most important species over silicon. This differs from the Mg-O and Al-O systems where the metallic vapors  $Mg(g)$  and  $Al(g)$  predominate at low  $p_{O_2}$ 's. As a result, active oxidation of Si by the formation of  $SiO$  is important and has been well studied.<sup>5,8</sup> The physical phenomenon of active oxidation involves weight loss, while passive oxidation involves weight gain as a protective oxide film grows. The active-passive transition is defined as the  $p_{O_2}$  at which further evaporation of  $SiO$  is prevented by the formation of a passive  $SiO_2$  film. This point was first emphasized by Wagner<sup>5</sup>; here, we show the utility of volatility diagrams in dealing with the active-passive transition. Our approach is essentially that pioneered by Wagner,<sup>5</sup> except that we ignore possible differences in the diffusivity of various species in the vapor phase.

Consider inserting a piece of Si into a furnace which contains some molecular oxygen. Two oxidation reactions are possible:



The volatility diagram is useful in differentiating active and passive oxidation and defining the active-passive transition. Figure 16(A) shows a schematic view of the active oxidation process. Oxygen molecules diffuse through a stagnant layer at the gas/solid interface and react with Si to form  $SiO$  molecules, which then diffuse away from this interfacial layer into the ambient. According to the

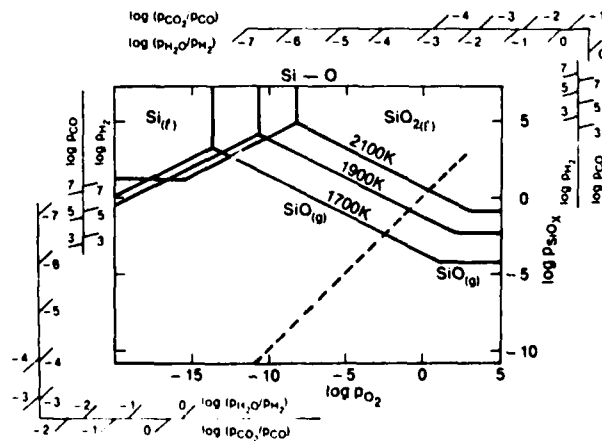


Fig. 14. Complete volatility diagram for the Si-O system.

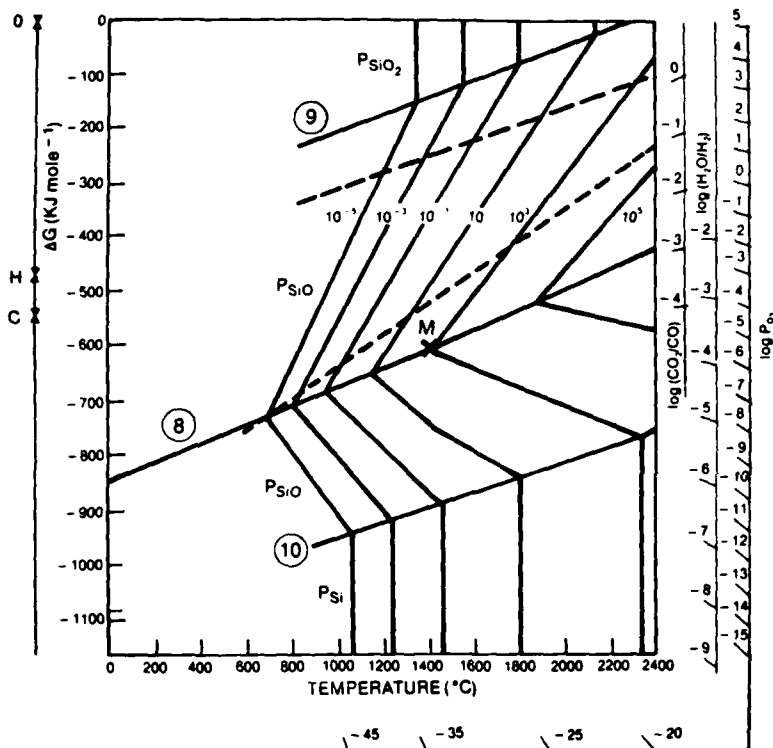


Fig. 15. Ellingham-type diagram for the Si-O system.

JANAF Tables, the equilibrium constant for Eq. (21a) at 1700 K is  $\approx 10^{16}$ . Thus, one can make the assumption that all the oxygen molecules arriving at this interface from the ambient are converted into  $\text{SiO}(g)$ . Based on this and the assumption that oxygen molecules arrive and  $\text{SiO}$  molecules depart at the same rate, active oxidation involves the generation of two  $\text{SiO}$  molecules for each oxygen molecule arriving at the Si surface. Therefore, at the interface  $p_{\text{SiO}} = 2p_{\text{O}_2}$  in the ambient. (This condition is in fact the same as for the isomolar line.) For example, at 1700 K, if the ambient  $p_{\text{O}_2}$  is  $10^{-15}$  Pa, then the  $p_{\text{SiO}}$  generated at the interface is  $2 \times 10^{-15}$  Pa. According to Fig. 17, this is many orders of magnitude lower than the equilibrium  $p_{\text{SiO}} \approx 10^3$  Pa (point a)—and hence  $\text{SiO}(g)$  should not condense. If the  $p_{\text{O}_2}$  is increased, the  $p_{\text{SiO}}$  will increase accordingly; at  $p_{\text{O}_2} = 10^{-12}$  Pa (point b) for example, the system should be in the  $\text{SiO}_2$  phase field; however, active oxidation will continue because the  $p_{\text{SiO}}$  is still far below the critical condensation value of  $\approx 10^3$  Pa at this point. As the  $p_{\text{O}_2}$  is further increased,  $p_{\text{SiO}}$  approaches the critical value and  $\text{SiO}_2$  smoke can form away from the interface (Fig. 16(B)). This active  $\rightarrow$  active + smoke transition in fact occurs at the isomolar point (c). If  $p_{\text{O}_2}$  is further increased to  $5 \times 10^2$  Pa,  $p_{\text{SiO}}$  is  $10^3$  Pa. This latter pressure will have exceeded the maximum equilibrium pressure defined by point T, and  $\text{SiO}_2$  will begin to condense on the silicon surface. Beyond this point, a passive  $\text{SiO}_2$  film will form,  $\log p_{\text{SiO}}$  will drop from  $10^3$  Pa at point T to  $10^{-4}$  Pa (point d), and weight loss will effectively cease. This is passive oxidation and is shown schematically in Fig. 16(C). The active-passive transition, although defined in terms of  $p_{\text{O}_2}$ , is determined by  $\text{SiO}$  vapor pressure:  $p_{\text{O}_2}$  at the active-passive transition  $= \frac{1}{2}p_{\text{SiO}}$  at point T.

One can put forward similar arguments for a hydrogen environment. Unlike the previous case, however, the oxygen carrier is  $\text{H}_2\text{O}$ . Two oxidation reactions are possible:

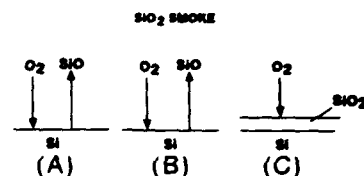
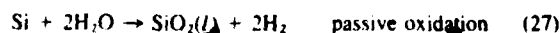


Fig. 16. Schematic view of active and passive oxidation of silicon; see text for discussion.

The method of construction of the  $\text{H}_2\text{O}/\text{H}_2$  nomograph enables the direct determination of the corresponding  $p_{\text{O}_2}$ . For example, a point b in Fig. 17,  $\log p_{\text{O}_2} = -12$  (Pa) and the corresponding  $\text{H}_2\text{O}/\text{H}_2$  ratio is  $10^{-4}$ , as is determined by noting the intersection of the  $\text{H}_2\text{O}/\text{H}_2$  scale of a line through point b. One can assume, as in the previous case, that all the  $\text{H}_2\text{O}$  molecules are consumed by reaction (26) to form  $\text{SiO}(g)$  and a simple relation— $p_{\text{SiO}}$  at the interface  $= p_{\text{H}_2\text{O}}$  in the ambient—is maintained. (This in fact is the condition for the isobaric lines.) Inserting a piece of Si into furnace containing  $\text{H}_2\text{O}/\text{H}_2$  at a ratio of  $10^{-4}$  at  $p_{\text{H}_2} = 10^5$  Pa will generate 10 Pa of  $\text{SiO}(g)$ , and as this is below the critical condensation value of  $p_{\text{SiO}} = 10^3$  Pa at point T, active oxidation will occur. With increasing  $\text{H}_2\text{O}$  to  $\text{H}_2$  ratios,  $\text{SiO}_2$  smoke will form when the ratio exceeds  $10^{-3}$  (the condition at the isobaric point e on Fig. 17 the active-passive transition occurs when the ratio is  $10^{-2}$ , as the  $\text{SiO}$  pressure at the triple point is then realized. At this condition  $p_{\text{SiO}}$  will drop from  $10^3$  Pa (point T) to 1 Pa; this pressure (point on Fig. 17) is determined by the intersection of the  $10^{-2}$  point on the  $\text{H}_2\text{O}/\text{H}_2$  scale with the maximum equilibrium pressure line. The difference between molecular  $\text{O}_2$  and  $\text{H}_2\text{O}/\text{H}_2$ ,  $T \rightarrow d$  and  $T \rightarrow f$ , respectively, is caused only by the thermodynamics of the  $\text{H}_2\text{O}/\text{H}_2$  equilibrium. In the latter case, the active-passive transition occurs when  $p_{\text{H}_2\text{O}}$  in the ambient  $= p_{\text{SiO}}$  at point T and the system must change to point f.

#### IV. Summary and Conclusions

Volatilization reactions in a metal-oxygen system in nonreacting or reducing environments can be fully understood using either volatility diagrams or Ellingham-type diagrams. Three pairs of such diagrams are shown in this paper, Figs. 6 and 7 for the  $\text{Mg}$  system, Figs. 10 and 11 for the  $\text{Al-O}$  system, and Figs. 14 and 15 for the  $\text{Si-O}$  system. The construction of these diagrams is somewhat more involved than the classical Ellingham diagram but is as simple from an application viewpoint. Use does, however, require some understanding of the significance of the isomolar line.

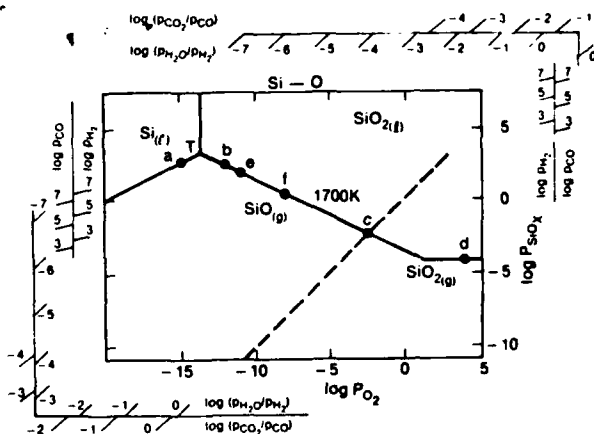


Fig. 17. Volatility diagram for the Si-O system at 1700 K. Points a-f refer to discussion in text on active and passive oxidation of Si.

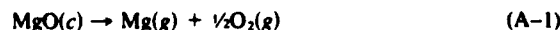
in neutral ambients and the isobaric lines in reducing ambients, in order to identify the valid portions of the diagrams—in fact, these *iso* lines are the principal original contributions of this paper.

The question of the relative merit of the volatility diagrams vs the Ellingham-type diagrams is interesting. On the one hand, the latter is more widely used in general, because of the convenient representation of the data, but volatility diagrams are popular with high-temperature scientists interested in gas-solid reactions because the species of interest,  $\text{MO}$ , gas, is plotted as one of the axes. Secondly, their use makes it easier to decide which vapor species in gas-solid reactions are important and to delineate valid regions of the  $p_{\text{O}_2}$ - $p_{\text{MO}}$  fields, and in this way are a useful intermediate step in constructing an Ellingham-type diagram. Thirdly, they are much more useful than Ellingham-type diagrams when dealing with solid solutions, oxycarbides, and oxynitrides, as will be discussed in future papers. Fourthly, it is a simple matter to compare the volatility of different oxides at a single temperature by noting the  $p_{\text{M}}$  or  $p_{\text{MO}}$  where the isomolar line intersects the maximum equilibrium pressure line (Fig. 18). Thus, it is easy to see that  $\text{Al}_2\text{O}_3$  is the least volatile and  $\text{MgO}$  the most volatile of the three oxides considered, in accord with common laboratory experience; furthermore, it is easy to see why all three of the oxides under consideration cannot easily be reduced to their elements—in all cases, access to the conditions where metal, solid or liquid oxide, and gaseous species can coexist requires very high pressures of reducing gases.

Finally, it is convenient to use volatility diagrams to determine the transition from active to passive oxidation, which occurs in those systems where a volatile  $\text{MO}$  species predominates, as in the Si-O system.

#### APPENDIX

The constant dew point lines can be shown to plot as straight lines in volatility diagrams using the following derivation. The important reactions here are



and



The equilibrium constants for these reactions can be expressed in terms of the partial pressures as well as the entropies and enthalpies of these reactions:

$$\log K_1 = \log \frac{p_{\text{Mg}} p_{\text{O}_2}^{1/2}}{a_{\text{MgO}}} = -\frac{\Delta H_1}{2.3RT} + \frac{\Delta S_1}{2.3R} \quad (\text{A-3})$$

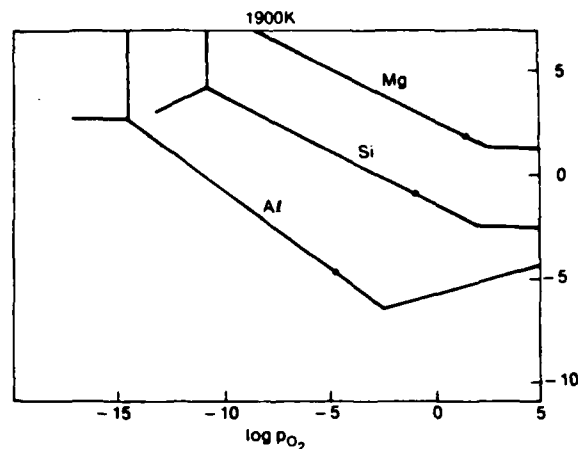


Fig. 18. Comparison of volatility diagrams for the Mg-O, Al-O, and Si systems at 1900 K.

$$\log K_2 = \frac{p_{\text{H}_2\text{O}}}{p_{\text{H}_2} p_{\text{O}_2}^{1/2}} = -\frac{\Delta H_2}{2.3RT} + \frac{\Delta S_2}{2.3R} \quad (\text{A-4})$$

By rearranging Eqs. (A-3) and (A-4) one can eliminate  $T$ , and assuming  $a_{\text{MgO}}$  to be unity, we find

$$\frac{1}{\Delta H_2} \left[ \frac{\Delta S_2}{2.3R} - \log \frac{p_{\text{H}_2\text{O}}}{p_{\text{H}_2} p_{\text{O}_2}^{1/2}} \right] = \frac{1}{\Delta H_1} \left[ \frac{\Delta S_1}{2.3R} - \log (p_{\text{O}_2}^{1/2} p_{\text{Mg}}) \right]$$

which can be simplified to the temperature-independent form

$$A \log p_{\text{Mg}} + B \log p_{\text{O}_2} + C \log \frac{p_{\text{H}_2\text{O}}}{p_{\text{H}_2}} + D = 0 \quad (\text{A-5})$$

where

$$A = 1/\Delta H_1$$

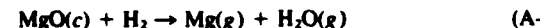
$$B = \frac{1}{2}[(1/\Delta H_1) + (1/\Delta H_2)]$$

$$C = -(1/\Delta H_2)$$

$$D = (1/2.3R)[(\Delta S_2/\Delta H_2) - (\Delta S_1/\Delta H_1)]$$

According to this equation, at constant  $\text{H}_2\text{O}/\text{H}_2$ ,  $\log p_{\text{Mg}}$  decreases linearly with  $\log p_{\text{O}_2}$ .

Similarly the relation between  $\log p_{\text{O}_2}$  and  $\log p_{\text{Mg}}$  (or  $\log p_{\text{H}_2}$ ) as depicted by the isobaric lines will be derived here. The two important reactions are water formation and magnesia reduction by hydrogen.



The equilibrium constants are

$$\log K_6 = \log \frac{p_{\text{H}_2\text{O}}}{p_{\text{H}_2} p_{\text{O}_2}^{1/2}} = -\frac{\Delta H_6}{2.3RT} + \frac{\Delta S_6}{2.3R} \quad (\text{A-8})$$

$$\log K_7 = \log \frac{p_{\text{Mg}} p_{\text{H}_2\text{O}}}{a_{\text{MgO}} p_{\text{H}_2}} = -\frac{\Delta H_7}{2.3RT} + \frac{\Delta S_7}{2.3R} \quad (\text{A-9})$$

But  $p_{\text{Mg}} = p_{\text{H}_2\text{O}}$  according to the mass balance criterion and assuming  $a_{\text{MgO}} = 1$ , Eq. (A-9) becomes

$$\log K_7 = \log \frac{p_{\text{H}_2\text{O}}^2}{p_{\text{H}_2}} = -\frac{\Delta H_7}{2.3RT} + \frac{\Delta S_7}{2.3R} \quad (\text{A-10})$$

By rearranging Eqs. (A-8) and (A-10) and eliminating  $T$ , one can again derive an expression which is independent of temperature:

$$A \log p_{\text{O}_2} + B \log p_{\text{Mg}} + C \log p_{\text{H}_2} + D = 0 \quad (\text{A-11})$$



where

$$A = 1/2\Delta H_0$$

$$B = (1/\Delta H_0) + (2/\Delta H_7)$$

$$C = -(1/\Delta H_7) + (1/\Delta H_0)$$

$$D = (1/2.3R)(S_0/\Delta H_0) - (S_7/\Delta H_7)$$

According to Eq. (A-10), at constant  $p_{H_2}$ ,  $\log p_{H_2}$  decreases linearly with  $\log p_{O_2}$ .

**Acknowledgments:** Victor L. K. Lou thanks several colleagues at CR&D, General Electric Company, for useful discussions. Professor John Halloran has provided many critical comments. A. H. Heuer acknowledges the Alexander Von Humboldt Foundation for a Senior Scientist Award, which made possible his sabbatical leave at the Max Planck Institut für Metallforschung, Stuttgart, FRG, where the first complete draft of this paper was prepared.

## References

- <sup>1</sup>O. Kubaschewski and C. B. Alcock, *Metallurgical Thermochemistry*, 5th ed., Pergamon Press, Oxford and New York, 1977.
- <sup>2</sup>Metals Handbook, American Society for Metals, 1948.
- <sup>3</sup>JANAF Thermochemical Tables, 2nd ed., National Bureau of Standards, 19 (Suppl. 1974 and 1975).
- <sup>4</sup>I. Barin, *Thermochemical Properties of Inorganic Substances*, Springer-Verlag, Berlin and New York, 1973.
- <sup>5</sup>C. Wagner, "Passivity During the Oxidation of Silicon at Elevated Temperatures," *J. Appl. Phys.*, 29, 1295 (1958).
- <sup>6</sup>K. Blegen, "Equilibria and Kinetics in the Systems Si-N and Si-N-O," *Spec. Ceram.*, 6, 223 (1974).
- <sup>7</sup>I. Colquhoun, S. Wild, P. Grieveson, and K. H. Jack, "Thermodynamics of the Silicon-Nitrogen-Oxygen System," *Spec. Ceram.*, 6, 207 (1974).
- <sup>8</sup>E. A. Gulbransen and S. A. Jansson, "The High-Temperature Oxidation, Reduction and Volatilization Reactions of Silicon and Silicon Carbide," *Oxid. Met.*, 4 (18) (1972).
- <sup>9</sup>S. A. Jansson and E. A. Gulbransen, "Thermochemical Considerations of High Temperature Gas-Solid Reactions," in *High Temperature Gas Metal Reactions Mixed Environments*, Edited by S. A. Jansson and Z. A. Foroulis, Metallurgical Society of AIME, New York, 1973.
- <sup>10</sup>S. C. Singhal, "Thermodynamics and Kinetics of Oxidation of Hot-Press Silicon Nitride," *J. Mater. Sci.*, 11, 500 (1976).
- <sup>11</sup>G. Ericksson, "Thermodynamic Studies of High Temperature Equilibria XII," *Chem. Scr.*, 8, 100-103 (1975).

AIR FORCE OFFICE OF SCIENTIFIC RESEARCH (AFSC)  
NOTICE OF TECHNICAL REVIEW  
This technical report has been reviewed and is  
approved for public release IAW AFR 190-12.  
Distribution is unlimited.  
PATRICK J. HANSEN  
Chief, Technical Information Division

Approved for public release:  
distribution unlimited.

